HAXPES on Transition Metal Oxides:

new insights into an effective use of the photoionization cross-sections

DISSERTATION

zur Erlangung des akademischen Grades

Doctor rerum naturalium
(Dr.Rer.Nat.)

vorgelegt dem Bereich Mathematik und Naturwissenschaften
der Technischen Universität Dresden

von
M.Sc. Daisuke Takegami
geboren am 15.05.1992 in Barcelona

Eingereicht am 30. September 2021
Tag der Verteidigung: 26. April 2022

Gutachter:

Prof. Dr. Liu Hao Tjeng

Prof. Dr. Jochen Geck

Prof. Dr. Ján Minár

Die Dissertation wurde in der Zeit von 11/2016 bis 09/2021
im Max Planck Institut für Chemische Physik fester Stoffe angefertigt.

Table of Contents

Abstract

Materials containing transition metals and rare earth elements have continued to attract attention due to many fascinating properties that emerge from the intricate interplay between the electron correlation effects, which arise from the strong Coulomb interactions often present in d and f orbitals, with the band formations in the periodic structure of the solids. The mathematical description of such systems, however, is highly complex and results in unsolvable sets of equations. Thus, an appropriate model must be chosen on each case and tested. Experimental input is thus needed as a verification, and also as guidance to make better models.

Amongst the wide range of experimental techniques available to determine the electronic structure, photoelectron spectroscopy is special due to the close relation between the spectra that is measured with these techniques and the one particle Green's functions, providing very direct information content. Photoelectron spectroscopy is a very well established experimental technique, but when used on bulk materials, it can have one major issue: the surface sensitivity. The electronic structure of the surface is not the same as in the bulk, and in correlated systems, these differences can lead into a major alteration of the electronic structure due to the delicate balance of different interaction strengths, and so it is crucial that spectra representative of the bulk can be obtained.

The most reliable way in which the surface contributions can be minimised for photoelectron spectroscopy is by using its high photon energy variant also known as Hard X-ray Photoelectron Spectroscopy (HAXPES). HAXPES is more bulk sensitive and also has several further advantages with respect to its lower energy counterparts such as the possibility to measure buried interfaces, reach deeper core levels, or greater polarisation dependence effects, to name a few examples. Despite all these advantages,

HAXPES is still not very widely used for the study of valence bands due to several challenges in the interpretation of the spectra.

In this thesis, we show that while often considered to be a minor detail or even neglected, understanding the photo-ionization cross-sections is crucial for the correct interpretation of its spectra. We study many of the different ways in which the cross-sections can affect the HAXPES experimental spectra, in order to learn how to make an effective use of them in our favour to get the information that is most relevant to us in each case. In order to achieve this, we study several carefully selected transition metal oxides with HAXPES as well as with other PES variants.

We start by solving an apparent contradiction which prevented a proper understanding of the HAXPES valence band spectra of compounds containing transition metals and rare earths, and could have been one of the reasons why there are not so many studies with HAXPES on the valence band in the literature. We will show that due to the cross-section relations, we cannot neglect contributions from e.g. the La $5p$, which are typically considered almost core-like and irrelevant for the physics studied in transition metal oxides. We will focus on $LaCoO_3$ as a representative example, but also provide a few more examples and provide a guide to see in which cases it may be necessary to make such considerations.

We make use of the very high cross-sections of $5d$ materials in HAXPES to study the class of double perovskite iridates, which have recently attracted interest as candidates for Kitaev physics. Due to the high Ir $5d$ cross-sections, the valence band spectra is completely dominated by the iridium spectral weight, making it possible to directly compare the spectra of many different iridates despite containing a wide range of ions in their composition. By fitting our calculations parameters to the experimental spectra, we conclude that the double perovskite iridates are highly covalent systems with essentially zero charge transfer, which would result in long-ranged interactions limiting the extent to which the Kitaev model can materialise.

Two different compounds are studied by complementing the information from the element-specific core level spectra and the valence band spectra, which has other contributions mixed but is more sensitive to parameters such

as the hybridization strength: First, we present a temperature dependence study of the $LaCoO_3$ HAXPES combined with O-K X-ray absorption spectroscopy to investigate the gradual low-to-high spin transition observed with increased temperature. Our results suggest a scenario in which paramagnetic $LaCoO_3$ should be considered as an inhomogeneous mixed spin-state system. Then, we present a comprehensive photoemission study of $CaCu_3Ru_4O_{12}$, a very rare system with 3d transition metal ions that according to some claims display Kondo behaviour. The HAXPES spectra is used to tune the parameters for LDA+DMFT calculations. Additional photoemission measurements are also performed with a wide range of energies to change the ratio of the multiple contributions, allowing us to find a small resonance peak in the Cu 3*d* as predicted by the calculations. From the calculations and their good agreement with the experimental studies, we conclude that $CaCu_3Ru_4O_{12}$ is a Kondo material, but with a very high Kondo temperature, finding a compromise between both sides of the literature and concluding a long standing debate.

Finally, we experimentally show that the initial state dependence, as predicted by Fadley et al. from the cross-section formulas, can be observed by measuring a single crystal sample with HAXPES on different orientations. We show, using the example of ReO_3, that a clear orientation dependence is present in many of the valence band feature. By applying the appropriate corrections, the shape of the atomic orbitals is recovered in the angular intensity plot. Other samples are also measured to prove that this technique can be used in a wide range of compounds.

Chapter 1

Introduction

1.1 The electronic structure of solids

Materials containing 3d, 4d, and 5d transition metals and 4f and 5f rare earth elements have continued to attract attention due to many fascinating properties that can be found in them. Such properties include high T_c superconductivity, colossal magneto-resistance, metal-insulator transitions, heavy-fermion behaviour, multiferroicity, and many other properties that challenge our understanding of solid state physics [1, 2]. The emergence of such complex effects is generally attributed to the intricate interplay between the electron correlation effects arising from the strong Coulomb interactions often present in d and f orbitals, with the band formations in the periodic structure of the solids. Such interplay is often very delicate, resulting in several nearly isoenergetic phases, making materials' properties highly susceptible to variations of the crystal structure, doping or other external factors such as temperature, pressure, or magnetic field. The understanding of the relationship between the physical properties, crystal structure and electronic structure is thus essential, not only from the theoretical point of view but also to design new materials.

Ab-initio approaches, which are based on mean-field descriptions of the periodic potential created by the electrons and nuclei, have been proven to be very successful in describing the electronic structure of a wide range of solid-state materials. However, mean-field approaches fail for many transition metal and rare-earth based compounds, due to the electronic correlations. The mathematical description of systems with correlations requires a many body approach, which result in unsolvable sets of equations. Approximations

need to be made in order to get solvable models. The validity of such approximations depends on the class or subclass of compounds, and such, an appropriate model must to be chosen on each case and tested. Experimental input is thus needed as a verification and also as guidance to make better models.

It is also important to note that calculating the ground state of the electronic structure can provide information about the total energy of the system and the charge density, like being done by density functional based band structure calculations, but most other physical properties depend actually on excited states of the system, which present further complications for mean field approaches.

One of the most direct approaches to get an insight on the electronic structure of the system is via the one particle Green's functions [3], which describe the systems with a single electron or hole removed. Amongst the wide range of experimental techniques available to determine the electronic structure, this makes photoelectron spectroscopy (PES) and inverse photoelectron spectroscopy (IPES) special due to the close relation between the spectra that is measured with these techniques and the one particle Green's functions. Techniques which involve addition or removal of multiple particles, such as Auger electron spectroscopy, or optical spectroscopies, in which electrons are excited without being emitted (and thus, both an electron and a hole are created) provide also valuable information. However, they involve the propagation of two or more particles, and its information content is less direct than the one particle Green's function. For example, for the case in which electron correlations are not important, the optical Green's function can be calculated from a convolution of the one electron Green's function and the one hole Green's function, meaning that knowing the optical electron-hole Green's function may not be enough to deconstruct it and get the single particle Green's functions, but knowing the one electron and one hole Green's function allows calculating the optical Green's function.

1.2 Photoelectron spectroscopy

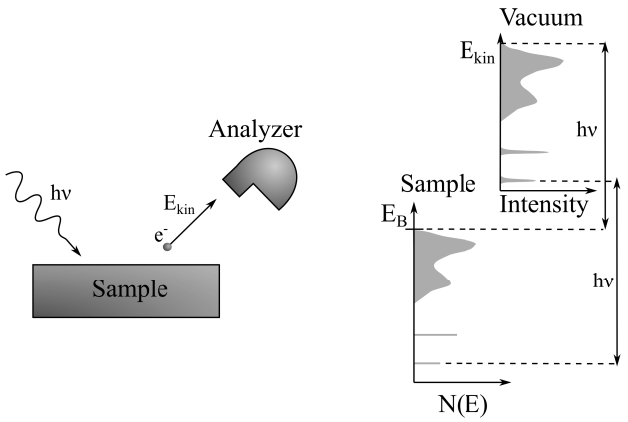

Figure 1.1: Schematic representation of the photoemission process. Left: A sketch of the experimental setting. Photons with energy $\hbar\nu$ interact with the sample, and photoelectrons with kinetic energy E_{kin} are emitted and picked up by the analyzer. Right: In the one electron theory, the photoemission spectra can be understood as a replica of the electronic density of states.

In PES, a monochromatic light with energy $\hbar\nu$ is focused to the sample, and due to the photoelectric effect, electrons are excited and ejected with a kinetic energy E_{kin} (Fig 1.1, left) [4]. The ejected electrons are then picked up by analyzers, obtaining a spectrum of the count-rate of the picked up photoelectrons as a function of their kinetic energy. From the conservation of energy, and under the one-electron approximation, we can get an idea of the energy that the photoemitted electrons had in the material before the interaction with the light, and thus, the spectra can be interpreted as a replica of the density of states (Fig 1.1, right).

To give a more rigorous description [5] , the observed intensity can be described by the Fermi's Golden Rule:

$$W_{IF} \propto |\langle I_N(0)|H^{int}|F_N\rangle|^2 \cdot \delta(E_N^F - E_N^I(0) - \hbar\nu), \tag{1.1}$$

where $|I_N(0)\rangle$ is the ground state with energy $E_N^I(0)$, $|F_N\rangle$ is the final state with energy E_N^F after the absorption of the photon, δ is the Dirac's

delta function and H^{int} is the Hamiltonian that describes the interaction of light with matter:

$$H^{int} = \sum_{n=1}^{N} \vec{A} \cdot \vec{p}_n, \tag{1.2}$$

where $\vec{A}$ is the photon vector field and $\vec{p}_n$ the momentum operator corresponding to the electron n. Then, under the sudden approximation, in which it is assumed that the photoemitted electron does not interact with the rest of the system once it is emitted, we can express the final state as

$$|F_N(k,j)\rangle = \boldsymbol{A}|k\rangle|F_{N-1}(j)\rangle \tag{1.3}$$

where $\boldsymbol{A}$ is the anti-symmetrizing operator, $|k\rangle$ the photoemitted electron with energy E_k, and $|F_{N-1}(j)\rangle$ corresponds to the final state with $N-1$ electrons, after the removal of its jth electron, with energy $E^F_{N-1}(j)$.

If we also approximate the initial state function as the product of the one-particle orbital $|i\rangle$ and the function with N-1 system with the ith electron removed $|I_{N-1}(0)\rangle$, then:

$$|I_N(0)\rangle = \boldsymbol{A}|i\rangle|I_{N-1}(0)\rangle. \tag{1.4}$$

We can also note that we can express $|i\rangle|I_{N-1}(0)\rangle$ using the annihilation operator ψ_i:

$$|I_{N-1}(0,i)\rangle = \psi_i|I_N(0)\rangle. \tag{1.5}$$

Using the following result of the Sokhotski-Plemelj theorem [6]

$$lim_{\varepsilon\to 0}\frac{1}{\omega + i\varepsilon} = P\left(\frac{1}{\omega}\right) - i\pi\delta(\omega), \tag{1.6}$$

where P denotes the Cauchy principal value [7], we can then develop equation 1.1 into the following expression:

$$W_I(E_k) \propto \lim_{\eta\to 0} \frac{1}{\pi} Im \sum_j \frac{\sum_i |\langle i|H^{int}|k\rangle \langle I_N(0)|\psi_i^\dagger|F_{N-1}(j)\rangle)|^2}{E_{N-1}^F(j)E_k - E_N^I(0) - \hbar\nu - i\eta}. \quad (1.7)$$

Finally, by changing the basis of the $|F_{N-1}(j)\rangle$ states we reach to

$$W_I(E_k) \propto \lim_{\eta\to 0} \frac{1}{\pi} Im \sum_{i,i'} M_{i'k} M_{ki} \langle I_N(0)|\psi_i'^\dagger \frac{1}{E_k - \hbar\nu + H - E_N^I(0) - i\eta} \psi_i |I_N(0)\rangle, \quad (1.8)$$

where $M_{ik} = \langle i|H^{int}|k\rangle$ is the optical matrix element. We can thus observe that the photoelectron spectrum corresponds to the one-hole Green's function multiplied with optical matrix elements. The matrix elements, also often referred to as the photo-ionization cross-sections, can highly alter the resulting spectra and depend on a wide variety of factors including the energies, momentum and polarization, and a proper understanding of these dependencies is crucial for the design of the experiments to be able to get the information that is most relevant to us, as we will observe in the following chapters of this thesis.

Using an analogous procedure as we have shown so far, it is possible to show that the IPES spectrum corresponds to the one-electron Green's function with its corresponding optical matrix elements. However, the focus of this thesis will be on PES, and thus, we will omit the details of the IPES technique.

PES (both its angular resolved (ARPES) version as well as the angular integrated version to which we will refer to by default) are by now well established techniques [4, 8, 9], with around half a century of history already. The core level spectra obtained from deep core electrons has been traditionally used to study the chemical compositions and environments, but it is also a valuable source of information about correlations. The valence band spectra, obtained from the shallow electrons from partially filled shells, provides highly detailed information about the electronic structure,

and in particular, about the bonds and covalency. With ARPES, one can also measure the dispersive electronic features, which can be compared to theoretically obtained band structures, or in case of strong correlations, give insight to the possible existence of quasi-particles and their behaviour.

1.3 Bulk sensitivity and HAXPES

Photoemission based techniques on bulk materials, however, can have one major issue: The surface sensitivity. Compared to photons or neutrons, electrons can scatter easily, and thus, the information of the photoemitted electrons from deep below the surface gets lost. This means that the surface contributions can have a relatively large effect on the obtained spectra. The electronic structure of the surface is not the same as in the bulk, as the translational symmetry is broken, the crystal structure can be different due to relaxation and the electronic coordination, and the ligand environment is different. In correlated systems, such differences can lead into a major alteration of the electronic structure due to the delicate balance of different interaction strengths, and so it is even more crucial that spectra representative of the bulk can be obtained. In Fig. 1.2, we show two different examples in which altering the bulk sensitivity (either via changing the emission angle, or the photon energy) can result in different spectra. In the example shown on the left panel, the intensity ratios of the peaks and features is altered, indicating that there is a change in the configuration of the Ce in $CeIr_2$ near the surface [10]. On the right panel, we can observe spectra from a series of compounds $Sr_{1-x}Ca_xVO_3$, which display a strong photon energy dependence, which turns out is due to the dependence of the probing depth [11]. By correcting for this and extracting the spectrum representative of the bulk, it is found that the bulk spectra does not depend on x, although the raw spectra suggest otherwise. This difference suggests strongly that the electronic structure on the surface does depend on x.

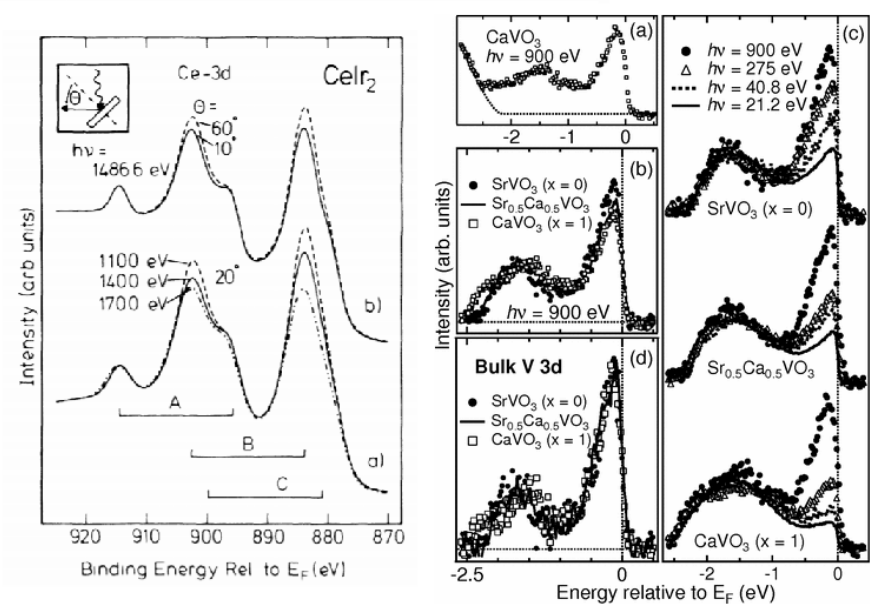

Figure 1.2: Left: Ce 3*d* core level spectra of $CeIr_2$ with varying degrees of surface sensitivity: (a) for different photon energies and constant electron-emission angle, $\theta = 20°$; (b) for different angles θ and constant $\hbar\nu = 1486.6$ eV. The change of the intensities in the regions A, B, and C indicate that surface sensitivity affects the measured ratio of the Ce configurations. Reprinted figure with permission from [10]. Copyright 2021 by the American Physical Society. Right: Valence band PES spectra of $Sr_{1-x}Ca_xVO_3$: (a) Raw spectrum near E_F of $CaVO_3$ (squares) and the fitted tails of O 2*p* contributions. (b) V 3*d* contributions obtained by subtracting the fitted tails of O 2*p* contributions from the raw spectra as in (a). (c) $\hbar\nu$ dependence of the V 3*d* contributions. (d) Bulk contributions of the V 3*d*. Reprinted figure with permission from [11]. Copyright 2021 by the American Physical Society.

The most widely used light sources in laboratories for PES provides photons between 10 eV for the UV gas discharge sources to around 1.5 keV of the Al x-ray sources. The kinetic energy of the emitted photoelectrons will be in the range between 0 - 10 eV (UV source) or 0 - 1.5 keV (Al source). In this energy range, the inelastic mean free path (IMFP) of the electrons, defined as "average distance that an electron with a given energy travels between successive inelastic collisions", is in most cases not larger than

5 - 15Å, which is a few unit cells at most, and in some cases, not enough to fully escape from the influence of the surface.

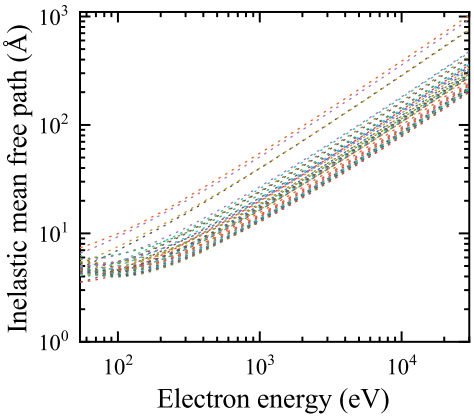

Figure 1.3: Inelastic mean free path of 41 elemental solids in function of energy calculated from optical data, from reference [12]

In general, the IMFP is known to have a strong energy dependence, and typically presents a minimum between $50 - 100$ eV kinetic energy, with a IMFP of around 5Å or smaller. Contrary to what the so-called "IMFP universal curve" often found in textbooks and literature may suggest [13], there is still a debate on what happens at the lower energy side. There are indeed experimental results backing a dramatic increase on the IMFP at very low energies as suggested by the so-called universal curve, attributing it to the lesser variety of excitation mechanisms that can scatter the electrons. However, not all experimental results consistently agree with such increase. Several other studies [14–16] show highly surface sensitive results, in which a layer of a few angstroms thick grown on top of the sample is enough to significantly suppress the signal coming from the material below, indicating much smaller values than expected. It is thus clear that the trend at lower energies has a strong material dependence. At high energies, however, there is a general agreement that the IMFP shows an increasing trend [12, 13, 17], reflecting the faster escape of electrons from the material. This makes PES with higher photon energies an attractive candidate to ensure data that is representative for the bulk regardless of the studied system.

Hard X-ray Photoelectron Spectroscopy (HAXPES) is defined as PES performed with hard x-rays, that is, photons with energies higher than around 2 keV. One of the main advantages of HAXPES with respect to soft x-ray photoelectron spectroscopy is, as discussed in the previous paragraph, the higher bulk sensitivity, with IMFP of 50Å or more. This can lead not only into the measurement of spectra which are more representative of the bulk properties, but also to allow measurements of buried interfaces or measurements in ambient pressure, to name some examples [17].

Higher photon energies also mean that deeper core levels can be reached. One example of interest is in the case of the Yb compounds, in which, on one side, the bulk sensitivity is important as the ratio of Yb^{2+} and Yb^{3+} can be different near the surface, but also because the core level Yb 3*d*, between 1.5 and 1.6 keV deep, allows an easier determination of the valence ratio compared to other core levels or valence band.

Other direct advantages of using high energies include the fact that the emitted photoelectrons will have less relative variation in their kinetic energies, and therefore the energy dependant IMFP, the effect of the inner potential barrier, or the instrument response functions will be closer to constant. Therefore, data measured from different core regions can be quantitatively compared.

In the valence band, higher energies allow a better decomposition of the spectrum into a sum of partial intensities based on orbital projected density of states and atomic differential cross-sections. This is due to what is known as the XPS limit [18], in which cross-sections become dominated by the core region of the atoms. Also, the elastic scattering is less pronounced, that is, there is a forward focusing effect, and thus directional effects such as the polarization dependence can be clearly observed. While such changes may result in increased difficulties to perform angular-resolved experiments, recent results also show that by performing the adequate corrections it is also possible to perform ARPES with hard x-rays [19].

Despite all these advantages, HAXPES is still not very widely used for the study of valence bands. One of its main complications, the overall smaller cross-sections, is no longer a critical problem with the much more

intense modern synchrotron photon sources. However, challenges in the interpretation have been reported, where the trends and features observed in the HAXPES spectra were not consistent with the theoretical models and techniques that had been so far used for interpreting the spectra obtained with photoemission in lower energies.

While often considered to be a minor detail or even neglected, understanding the photo-ionization cross-sections, and in particular, knowing up to which extent theories on the trends and behaviour of the cross-sections that were developed originally for lower energy PES are still valid for HAXPES is crucial for the correct interpretation of its spectra and also to make the most of this technique.

1.4 Scope

In this thesis, we study many of the different ways in which the matrix elements or cross-sections can affect the HAXPES experimental spectra, in order to learn how to make an effective use of them in our favour to get the information that is most relevant to us in each case. In order to achieve this, we will study several carefully selected transition metal oxides with HAXPES as well as with other PES variants. We will show that by changing the photon energy it is possible to enhance or suppress the contribution of certain orbitals, allowing a selective study of the desired contributions by selecting the appropriate energies. We will also show that the polarization of the light can be used for similar purposes as it has a major influence on the way photoelectrons are emitted. Finally, we will also explore the changes observed by changing the orientation of the measured crystals; something that for PES has been barely studied despite some highly promising early theoretical results which suggest that in specific measurement geometries, it could provide direct information on the symmetries of the active orbitals of the ground state.

We will first provide a more detailed overview of the matrix elements and the cross-sections in Chapter 2 and discuss about the different trends, approximations, as well as briefly describing the experimental geometry used in our HAXPES experiments in relation to the cross-sections.

In Chapter 3 we solve an apparent contradiction which prevented a proper understanding of the HAXPES valence band spectra, and could have been one of the reasons why there are not so many studies with HAXPES on the valence band in the literature. We will show that due to the cross-section relations, we cannot neglect contributions from e.g. the La 5*p*, which are typically considered almost core-like and irrelevant for the physics studied in TMOs. We will focus on $LaCoO_3$ as a representative example, but also provide a few more examples of compounds in which such often neglected contributions take a role and provide a guide to see in which cases it may be necessary to consider them.

In Chapter 4 we present a study of the class of double perovskite iridates. In double perovskite iridates, it was theorized that due to the combination of crystal field splitting and spin-orbit coupling a scenario in which spin-liquid states via the Kitaev mechanism may be possible to realize. Even though the double perovskites studied have a wide range of atoms in their chemical composition, the very high Ir 5*d* cross-sections in HAXPES allows the measurement of valence band spectra completely dominated by the iridium spectral weight, making it possible to directly compare the spectra of many different iridates. We study the experimental spectra with a combination of ab-initio and tight binding calculations. The ab-initio calculations provide an estimate of the parameters which is then optimized by down-folding or fitting the tight binding calculations to the experimental spectra. In this study, we observe that the double perovskite iridates are highly covalent systems with essentially zero charge transfer, which would result in long-ranged interactions preventing the materialization of the Kitaev model.

In Chapter 5 we present a temperature dependence study of the $LaCoO_3$ HAXPES and O-K X-ray absorption spectroscopy to investigate the gradual low-to-high spin transition observed with increased temperature. We will complement the analysis of the Co 2*p* core level spectra, which is completely element-specific, with the valence band spectra, which has other contributions mixed but is more sensitive to parameters such as the hybridization strength. By using cluster calculations, we show that the experimental data can reproduced by incoherently summing low spin and high spin spectra. Furthermore, the hybridization strength must be reduced in the high spin calculations, as to take into account the structural changes, in order to get an accurate reproduction. Our results suggest a scenario in which paramagnetic $LaCoO_3$ should be considered as an inhomogeneous mixed spin-state system.

In Chapter 6 we present a comprehensive photoemission study of $CaCu_3Ru_4O_{12}$, a very rare system with 3d transition metal ions that according to some claims display Kondo behaviour. The physics in $CaCu_3Ru_4O_{12}$ have been subjected to a long standing debate with several experimental and theoretical works arguing for and against the Kondo

scenario. In our study we observe that the magnetic susceptibility reported in the literature does not show a Cu 2+ signal, despite spectroscopic evidence of the 2+ magnetic character of the Cu ions. Thus, we find that there must be some form of screening mechanism. From the core-level bulk-sensitive HAXPES experiments, we observe satellite structures confirming the presence of an additional screening process. We show valence band measurements using a wide range of photon energies in order to disentangle the different contributions by altering the cross-section ratios of the different orbitals present in the valence band. LDA+DMFT calculations, performed by our collaborators, with parameters finely tuned to match the experimental spectra confirm the presence of a Kondo mechanism between the Cu 2+ ions and the Ru 4*d* bands. In the calculations, a small peak is predicted just above the Fermi energy, which we find by measuring PES using a photon energy corresponding to the Cooper minima of Ru 4*d*, where the Cu 3*d* - Ru 4*d* cross-section ratio is the highest. Performing multiple measurements in energies in-between ensures that the spectral features vary according only to the cross-section relations, and no changes appear due to potential surface-related contributions. From the calculations, and their good agreement with the experimental studies, we conclude that $CaCu_3Ru_4O_{12}$ is a Kondo material, but with a very high Kondo temperature, finding a compromise between both sides of the literature.

Finally, in Chapter 7 we experimentally show that the initial state dependence, as predicted by Fadley et al., can be observed by measuring a single crystal sample with HAXPES on different orientations. We show, using the example of ReO_3, that a clear orientation dependence is present in many of the valence band features. By applying the appropriate corrections, the shape of the atomic orbitals is recovered in the angular intensity plot. Other samples are also measured to prove that this technique can be used in a wide range of compounds.

Chapter 2

Matrix Elements and Cross-sections

In the introduction we have presented photoemission spectra in therms of the one-hole Green's function multiplied by matrix elements. The matrix elements account for many different effects that can influence the intensity captured in photoelectron spectroscopy. Amongst them, the most relevant to this work are the orbital, photon energy ($\hbar\nu$), and polarization dependent photo-ionization cross-sections.

The differential photo-ionization cross-section for linearly polarized light in a first order dipolar approximation is given by [20]:

$$\frac{d\sigma_i}{d\Omega} = \frac{\sigma_i}{4\pi}\left[1 + \beta_i P_2(\cos\theta)\right], \tag{2.1}$$

where σ_i and β_i are the photon energy and sub-shell dependent photo-ionization cross-section parameter and asymmetry parameter, P_2 is the second order Legendre polynomial, and θ is the angle between the photon polarization and the photoelectron propagation vector. Analogous formulas exist for the cases with non polarized or circularly polarized light. Here, however, we will focus on the case corresponding to linearly polarized light, most relevant for our measurements performed at synchrotron radiation facilities. As for the values of the parameters, there are several tables available in the literature with numerically calculated values [20–23] using different approaches and models as well as experimentally determined values. it is important to note that the calculated tabulated values rely typically on atomic values and using one-electron approximation, and thus they have to be used with some care for cases in which the conditions deviate much from said assumptions.

In this chapter, we will observe how photon energy and polarization dependence of the photo-ionization cross-section affect our measurements. As we will observe in this chapter, the photo-ionization cross-sections can greatly influence not only the overall intensity in the measurements but also the shape of the measured spectra. By choosing the right conditions, the photo-ionization cross-sections can allow the disentanglement of the contributions of different orbitals in the valence band or the enhancement of certain desired contributions allowing a more direct analysis and understanding of the data.

2.1 Energy dependence

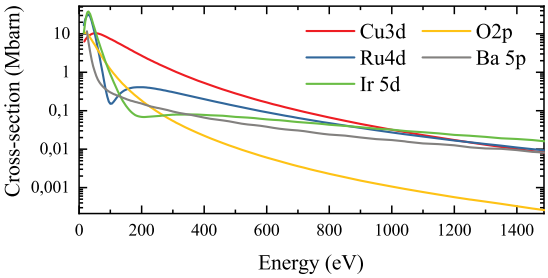

Figure 2.1: Values of σ for different atomic orbitals as tabulated in ref. [21].

In general, photo-ionization cross-sections have a decreasing trend with energy, which historically made the use of high energy (of several keV) photons for photoelectron spectroscopy very difficult due to the lack of photon flux. With modern synchrotron radiation sources, a much higher flux is available in a wide range of photon energies, allowing photoemission experiments with high photon energies feasible in a more practical timespan, although it is still one factor which needs to be considered when planning more delicate experiments. The specific energy dependence is different for each subshell as it can be observed in the examples displayed in Fig. 2.1, and thus, by changing energy the ratio of the spectral weights due to different orbitals will vary. Such variation in the ratios can be used to disentangle the different contributions in the valence band spectra, where typically there are

several different contributions overlapping, or to study the electronic states of one specific contribution that becomes dominant due to the effect of the cross-sections. Several practical examples are presented in the following chapters.

In Fig. 2.1 we can also observe that in some cases (such as Ru 4*d* and Ir 5*d*), the trend is not monotonous, but instead has a local minimum around $100 - 200$ eV. This is known as a Cooper minimum, and it can be found in orbitals with nodes in the radial part of the equation, such as the 4*d* or 5*d*, which can lead to a strong reduction of σ. The existence and the exact value of the Cooper minima have also been a subject of interest [21, 24], due to the additional possibilities it offers for the disentanglement or enhancement of selected orbital contributions. In chapter 5 we will present a study in which we have made use of the Cooper minima to isolate a specific contribution, in order to study it in detail.

2.2 Polarization dependence

Another cross-section effect that can significantly change the spectra is the polarization dependence, a consequence of the dipole selection rules that dictate which transitions are allowed depending on the symmetry of the electronic wave functions involved [25]. In the atomic picture, these rules are:

$$\Delta L = \pm 1 \text{ and } \Delta m_L = 0 \text{ for linear polarization,}$$
$$\Delta L = \pm 1 \text{ and } \Delta m_L = \pm 1 \text{ for circular polarization.}$$

One very illustrative example is the case of the *s* electrons photoexcited with a linearly polarized light, resulting in a final state of $p_{\pm\frac{1}{2}}$. This results into the photoelectrons being emitted in a highly anisotropic manner: In the direction of the light polarization, where the *p* orbital lobes of the final state are pointing, the amount of photoelectrons will be high, while in any direction perpendicular to it we will expect almost no photoelectrons.

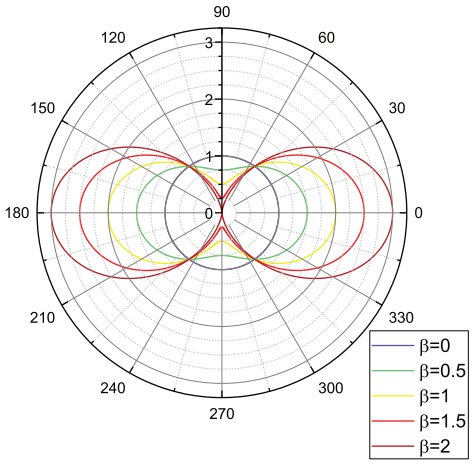

Figure 2.2: Polar plot of the cross section angular dependence on θ with different β_i values, calculated with the angle dependent part of equation 2.1.

In the cross-section formula presented in the equation 2.1 , this dependence is included in a first order approximation by the $\beta_i P_2(\cos\theta)$ term, where β_i is the energy dependent asymmetry parameter specific for each orbital, P_2 the second Legandre polynomial and θ the angle between the electrical field vector of the light and the momentum of the photoelectron. For values of β_i close to 2, which is the case for most s orbitals, the anisotropy is very pronounced, while for smaller β_i, closer to 0, such as for f orbitals, the intensity is almost isotropic, as illustrated in Fig. 2.2.

2.2.1 Experimental geometries in BL12XU

In order to change θ to perform polarization-dependent measurements, that is, to change the angle between the polarization of the light and the momentum of the measured outgoing electrons, one can choose to change either the light polarization or the electron collection position. In beamlines using synchrotron radiation sources, one typical approach is to use phase retarders to change the polarization of the incoming x-ray beam [26]. However, in such cases, undesired contributions could be present due to a non-ideal polarization factor. The approach taken in the BL12XU beamline in SPring-8, where our HAXPES experiments are performed, is

to keep the horizontal polarization that the incoming beam provides and change the electron collection position having two analyzers mounted in different positions [27, 28].

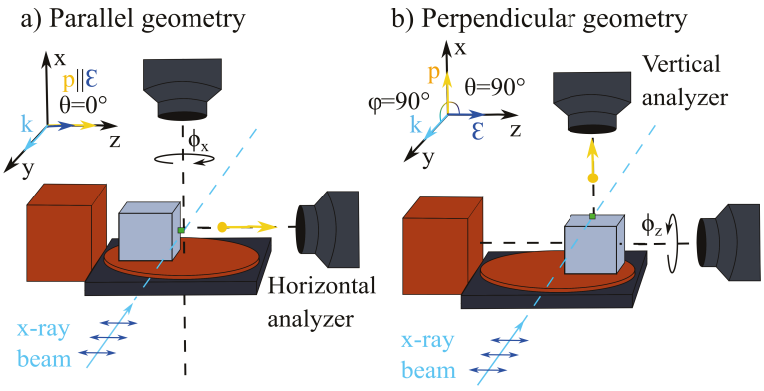

Figure 2.3: Schematic representation of the experimental setup in the two measurement geometries. The x-ray propagates in the **k** direction with linear polarization ε, which hits the sample represented with the green square. In the parallel geometry (a), the photoelectrons are captured by the analyzer mounted horizontally. The momentum of the measured electrons **p** and the polarization ε is parallel. In the perpendicular geometry (b), the photoelectrons are captured by the analyzer mounted vertically. The momentum of the measured electrons **p** and the polarization ε is perpendicular.

Fig. 2.3 a) schematically shows the parallel geometry, in which an analyzer is mounted horizontally in the same plane as the ring is used. In this geometry, the polarization (ε) and the momentum of the measured electrons (**p**) are parallel, and thus, $\theta = 0°$. The angle φ, which will later be used for the non-dipolar terms, is the angle between the direction of the incoming light (**k**) and the projection of **p** on the plane defined by ε, and in this geometry it is not well defined as $\mathbf{p}||\varepsilon$. In the perpendicular geometry, as shown in Fig. 2.3 b) an analyzer is mounted vertically, perpendicular to the plane of the ring. In this geometry, $\mathbf{p}\perp\ \varepsilon$ and thus, $\theta = 90°$. Also, $\varphi = 90°$, as it can be observed in the schematic representation.

According to Fig. 2.2, these two geometries should provide the maximum contrast obtainable. One example of the anisotropies that can be obtained is presented in Fig. 2.4. The region containing the Pt $4f$ and the Be $1s$

core levels (amongst others) is measured using the two different geometries, parallel and perpendicular. After normalizing the intensities to the Pt $4f$ peak, we can observe that in the perpendicular measurement the spectral weight of the features labeled as Be $1s$ are almost completely suppressed. This allows us to confirm that these peaks indeed have an s character [29].

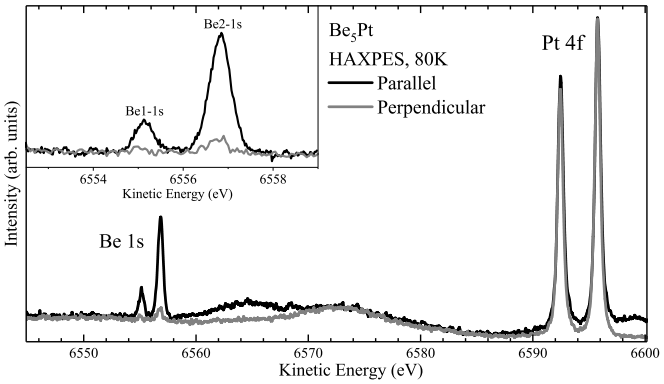

Figure 2.4: Pt $4f$ and Be $1s$ core level HAXPES spectra of Be_5Pt with $\theta = 0°$ (parallel) and $\theta = 90°$ (perpendicular). The spectra has been normalized to the Pt $4f$ core level peak intensities. The inset shows a close-up of the region with the two Be $1s$ peaks from the two different Be sites. The strong supression of both features in the perpendicular orientation confirms the s-character of both features [29].

In the valence band, where the contributions from different orbitals are usually highly mixed, the polarization dependence can also be used for discerning the different contributions. However, it is often a much more complicated job and requires a more careful analysis of the cross-sections as well as some calculations. One example is presented in Fig. 2.5, where it is possible to observe that the intensity ratios of the various spectral features can change considerably. However, due to the complexity of the line shape as well as the variety of orbitals involved, the interpretation of such changes may not be trivial [30].

Further examples can be found in the literature [27, 31–34] as well as in some of the results presented in the following chapters.

While for qualitative analysis and the comparison of general trends the equations and calculated parameters under the atomic, dipole-only and

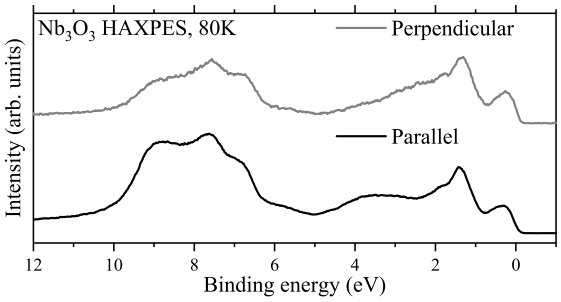

Figure 2.5: HAXPES valence band spectra of an Nb_3O_3 single crystal measured at 80K with $\theta = 0°$ (parallel) and $\theta = 90°$ (perpendicular).

first order approximation works generally fine, some discrepancies can be observed when trying to perform a more quantitative analysis [27]. In chapter 3 we will present such a quantitative analysis of experimental results, in which corrections are applied.

2.3 Beyond dipole and second order approximation

The cross-section equation (2.1) that was presented in the beginning of this chapter corresponds to a dipole-only first order approximation. According to recent theoretical results [23], however, non-dipole first order and second order terms may contribute appreciably to the angular distribution at high photon energies. In this section we will present the equations expanded up to the second term, and discuss how relevant the additional terms are in the two geometries used in our experiments.

The first-order equation with non-dipole matrix elements included is the following:

$$\frac{d\sigma_i}{d\Omega} = \frac{\sigma_i}{4\pi}\left[1 + \beta_i P_2(\cos\theta) + \overbrace{(\gamma\cos^2\theta + \delta)\sin\theta\cos\varphi}^{\text{Non-dipole terms}}\right] + O[(kr)^2], \quad (2.2)$$

with two additional first order non-dipolar parameters γ and δ. In the parallel geometry, we have that $\theta = 0$, and thus, $\sin\theta = 0$ and the non-dipolar term is cancelled. In the perpendicular geometry, $\theta = 90°$ and $\varphi = 90°$, and thus, $\cos\varphi = 0$, cancelling again the effect of γ and δ and resulting in the same equation as (2.1).

Next, if we expand the equation to include the second order terms, we obtain the following equation:

$$\frac{d\sigma_i}{d\Omega} = \frac{\sigma_i}{4\pi}\Big[1 + (\beta_i + \Delta\beta_{lp})P_2(\cos\theta) + (\gamma\cos^2\theta + \delta)\sin\theta\cos\varphi + \eta P_2(\cos\theta)\cos 2\varphi + \mu\cos 2\varphi + \xi(1+\cos 2\varphi)P_4(\cos\theta)\Big] \tag{2.3}$$

with the additional second order non-dipolar parameters $\Delta\beta_{lp}$, η, μ and ξ. Here we can observe that there is already a term directly added to β_i, resulting in a correction that cannot be cancelled out as it was the case for the first order non-dipolar terms. As for the contribution of the rest of the terms, in the parallel geometry we evaluate (2.3) with $\theta = 0$ and φ undefined:

$$\begin{aligned}\frac{d\sigma_i}{d\Omega} &= \frac{\sigma_i}{4\pi}\left[1 + (\beta + \Delta\beta_{lp}) + \xi + \overbrace{(\eta + \mu + \xi)}^{=0}\cos 2\varphi\right] \\ &= \frac{\sigma_i}{4\pi}\left[1 + \beta + \Delta\beta_{lp} + \xi\right].\end{aligned} \tag{2.4}$$

the term $(\eta + \mu + \xi) = 0$ is a result by the way the parameters are defined, but it can also be understood as the result of imposing continuity, as the directional limits $\lim_{\theta\to 0}\frac{d\sigma_i}{d\Omega}$ must converge from all directions i.e. $\forall\varphi$, a condition only met if $(\eta + \mu + \xi) = 0$.

As for the perpendicular geometry, we evaluate (2.3) with $\theta = 90°$ and $\varphi = 90°$ and obtain the following:

$$\frac{d\sigma_i}{d\Omega} = \frac{\sigma_i}{4\pi}\left[1 - \frac{1}{2}(\beta_i + \Delta\beta_{lp} - \eta) - \mu\right]. \tag{2.5}$$

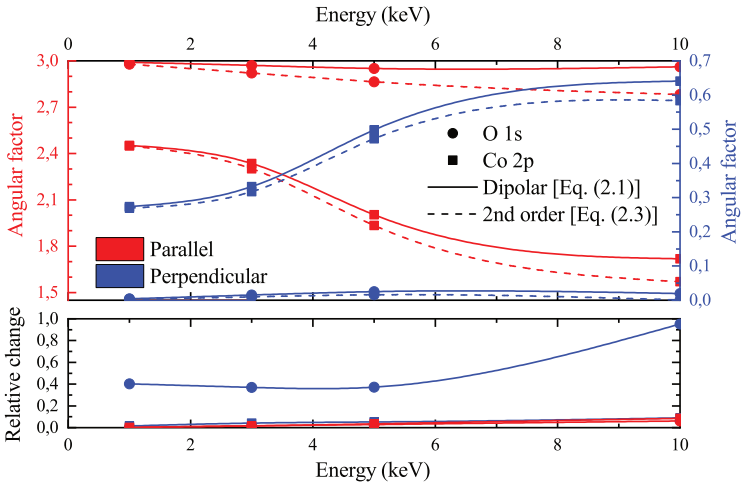

Figure 2.6: Top: Variation of the angular factor (i.e. the cross-section value without the $\frac{\sigma_i}{4\pi}$) in parallel (in red) and perpendicular (in blue) geometries for O 1s and Co 2p, using the first order dipolar approximation (continuous line) and the second order equation (dashed line). Bottom: Relative change from the dipolar approximation to the second order equation, obtained by dividing the difference between the two approaches by the angle factor of the dipolar approximation.

In order to examine the relevance of the 2nd order corrections, we compare in Fig. 2.6 the results of using equation (2.1) and equations (2.4) and (2.5) for O 1s and Co 2p. On the top panel we can observe that overall the differences become larger for higher energies. The relative change between using or not the higher order terms is shown in the bottom panel. There, we can observe that in Co 2p (as well as in most of our examples with β_i not close to 2) the relative decrease is no larger than around 10%, but for O 1s in perpendicular geometry, where the intensity is small, its relative change can reach 95% at 10 keV. While the magnitudes of the correction factors are not so different, for orbitals with values of β_i close to 2, where the suppression is largest, smaller corrections can play an appreciable role. While here we will not study in detail the trend for all orbitals, we can conclude that second order terms can indeed have a significant weight at higher energies and it could be necessary to take into account when trying to

perform quantitative analysis that goes beyond observing general trends. In chapter 3, we will further discuss the relevance or necessity of these higher order corrections, and how does this change when additional corrections related to the experiment, such as the effective angle correction, come into play.

Chapter 3

Towards a quantitative analysis of the valence band HAXPES:

Unexpected contributions and quasi-elastic scattering corrections.

As it has already been discussed in the introduction, in correlated compounds the electronic structure of the bulk and the surface can be significantly different due to changes in the local coordination and symmetries, and therefore, in order to study them, it is necessary make sure that the measured spectra is bulk-sensitive. In photoemission, such bulk-sensitivity can be achieved by using hard x-rays, that is, HAXPES. In the class of transition metal oxides, there are many HAXPES core-level studies making use of this additional bulk-sensitivity. However, the amount of valence band studies remains surprisingly low. In particular, in the case of rare earth containing $3d$ transition metal oxides, of considerable interest due to their tunability and rich phase diagrams, several problems about the interpretation of the valence band spectra have been reported. The ultra-violet or soft x-ray PES valence band spectra of such compounds are typically interpreted in terms of a weighted sum of the transition metal $3d$, oxygen $2p$, and/or rare-earth $4f$ spectral weights. However for the HAXPES version such an approach does not work even on the qualitative level.

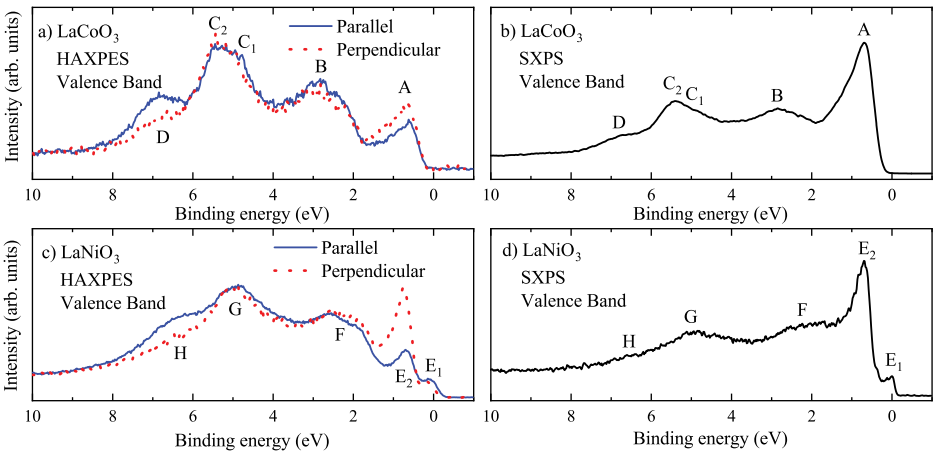

Figure 3.1: a) and c) Valence band HAXPES spectra ($h\nu = 6.5$ keV) of $LaCoO_3$ and $LaNiO_3$ respectively taken in the parallel ($\theta = 0°$) and vertical ($\theta = 90°$) geometries. b) and d) Valence band SXPS spectrum ($h\nu = 700$ eV) of $LaCoO_3$ and $LaNiO_3$ respectively. The data displayed in panel b) was measured by T. Koethe and is published in Takegami et. al. [28]

Figure 3.1 shows two of such examples: $LaCoO_3$ (a) and b)) and $LaNiO_3$ (c) and d)), where the valence band HAXPES spectra with $h\nu = 6.5$ keV and soft x-ray photoelectron spectroscopy (SXPS) with $h\nu = 700$ eV is compared. Of the features that can be observed in the SXPS spectra of $LaCoO_3$ ($LaNiO_3$), the feature near the Fermi energy A (E_1/E_2) is typically attributed to the Co (Ni) $3d$ contributions [35], and B-C (F-G) and the intensity in the 2-6 eV region, is considered to come from the O $2p$ bands.

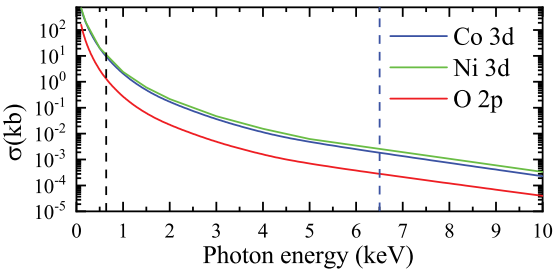

Figure 3.2: Subshell photo-ionization cross-section (σ) of Co $3d$ and O $2p$ deduced from [20, 22, 23].

Comparing the SXPS to the HAXPES spectra, we can observe that for higher energies, feature A (E) becomes smaller than B-C (F-G). The observed trend, however, is the opposite than what we would expect from the cross-sections values as shown in Figure 3.2, which predicts a larger suppression to the O $2p$ contributions than to the $3d$ from the transition metals. If we now compare the HAXPES spectra measured with different polarization, we observe that in both samples, A and E, is less suppressed than B-C/F-G features (i.e. A and E appear to be larger in the perpendicular orientation after normalizing both spectra). However, according to the same cross-section tables, at 6.5 keV the $3d$ orbitals from Co and Ni have a β asymmetry parameter of around $0.3 - 0.4$, larger than the 0.1 of O $2p$. This means, according to the cross-section, we should have expected a larger suppression for the $3d$ contributions, contrary to what we observe in the experiment.

The fact that such contradictions can be observed calls for a more careful look into the way on how HAXPES experimental valence band spectra is interpreted. From the analysis presented so far, one could prematurely get into the conclusion that the cross-section tables are not correct. However, we will demonstrate that this analysis using the most typically relevant orbital contributions was in fact incomplete.

In this chapter, we will show that this problem can be solved by including contributions from shallow core-levels which are often neglected due to their lesser relevance in the physical properties of such compounds, but gain relevance due to the huge cross-sections at the high photon energies used in HAXPES. We will observe that this is not only limited to the early rare earth elements, but applies in general to many elements in the first columns of the periodic table, where the binding energies of their p states are deep enough to be considered core levels ($15 - 20$ eV), but still shallow enough to get mixed with valence states. Furthermore, we will show that the use of cross-section tables can often provide a good quantitative match, but for specific geometries additional corrections must be included. We will discuss the corrections necessary to include the effect of quasi-elastic scattering processes and its behaviour with temperature and photon energy.

All HAXPES experiments presented in this chapter were performed at the BL12XU beamline, with the experimental geometries as described in Chapter 2. The *ab-initio* calculations were performed with FPLO unless specified otherwise. The one-step model calculations were provided by J. Minár and L.Nicolaï.

3.1 The $LaCoO_3$ spectra

The results presented in this section are published in:

Phys.Rev.B **99**, 165101 (2019).

$LaCoO_3$ is a non-magnetic insulator at low temperatures, with the Co^{3+} $3d^6$ ion in the octahedral oxygen coordination having the low spin t_{2g}^6 configuration [36–42]. Despite the presence of strong electronic correlations, non-magnetic $LaCoO_3$ with a completely filled t_{2g} and empty e_g can effectively be considered as a band insulator, for which *ab-initio* band structure calculations can be expected to provide a reasonable description of its electronic structure. This is important since we will make use of one-step photoemission calculations [17, 43–45] based on such band structure results to explain the valence band HAXPES spectrum and to study whether the sum of the partial density of states of the atomic constituents weighted by their tabulated photo-ionization cross-sections can reproduce the experiment.

In order to identify the origin of the valence band features observed in HAXPES, we carried out LDA calculations for $LaCoO_3$ in the non-magnetic phase. The total density of states (DOS) and the partial density of states (PDOS) are displayed in the left panel of Fig. 3.3. We can observe that peak A is mostly due to the Co d and that features B-C1-C2-D are originating primarily from the O p, consistent with earlier analyses in the literature [35]. For completeness, we also show the PDOS of the Co s, the La p and La d. They are tiny, but we will show below that they are important for the interpretation of the HAXPES signal. We have not shown the contribution of the La s PDOS since it is even much smaller than the Co s. In order to compare the LDA calculations with our HAXPES and SXPS spectra,

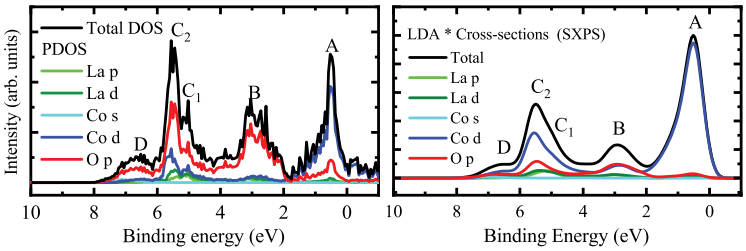

Figure 3.3: Left: Calculated density of states (DOS) of $LaCoO_3$ and partial density of states (PDOS) of the orbitals relevant to our study. The contribution of the La s PDOS is not plotted since it is even much smaller than the Co s. Right: Simulated valence band SXPS spectrum of $LaCoO_3$ obtained by multiplying the Co d, O p, Co s, La p, La s and La d PDOS by their respective photo-ionization cross-section at 700 eV photon energy, followed by their summation. The contribution of the La s PDOS is not shown since it is even much smaller than the Co s.

we scaled the PDOS by their respective photo-ionization cross-sections. Table 3.1 shows the exact values of the photo-ionization cross-sections for the energies used in the experiment, after including also the effect of the asymmetry parameter β.

We then multiplied them with the Fermi function, applied a broadening using a Gaussian of 0.25 eV (HAXPES) or 0.2 eV (SXPS) full width at half maximum (FWHM) and a Lorentzian of 0.1 eV FWHM, to account for experimental resolution and lifetime, respectively, and calculated their sum. We also have carried out calculations with the one-step method to directly simulate the HAXPES valence band spectra.

In the right panel of Fig. 3.3 we show the results for the SXPS spectrum. We can observe that the sum of the PDOS weighted by the respective photo-ionization cross-sections at 700 eV photon energy reproduce quite well the overall experimental spectrum displayed in Fig. 3.1 b), in particular that peak A is more intense than features B-C-D. We identify the Co $3d$ and the O $2p$ as the major contributors to the SXPS spectrum, thereby confirming the earlier assignment in the literature [35]. For SXPS, we can safely neglect the contribution of the Co $4s$, La $5p$, La $5d$ and La $6s$ PDOS.

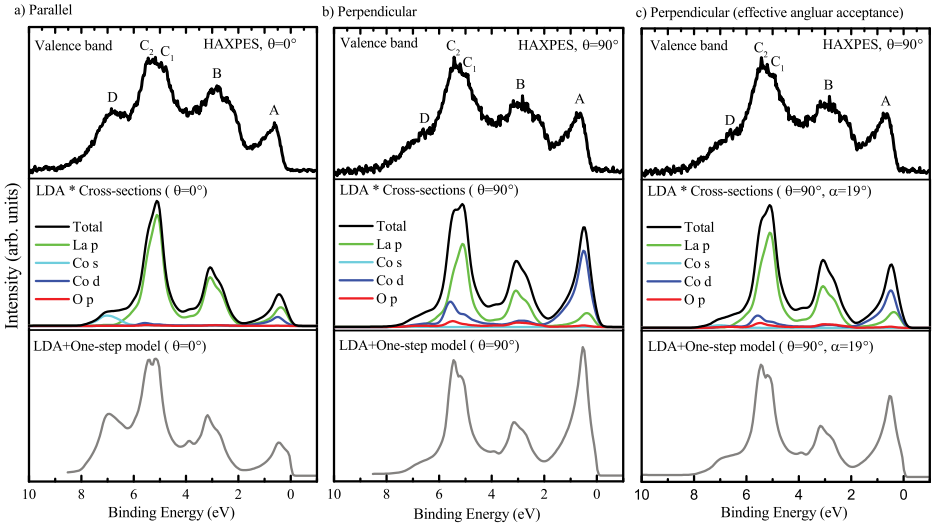

Figure 3.4: Experimental HAXPES valence band spectra (upper panels) compared with the simulated spectra obtained by multiplying the Co d, O p, Co s, La p, La s, and La d PDOS from the LDA calculations by their respective photo-ionization cross-section (middle panels) followed by their summation, and the results after using the one-step model on the LDA calculations (lower panels). Panels a) and b) show the results corresponding to the parallel ($\theta = 0°$) and perpendicular ($\theta = 90°$) geometry, respectively. Panel c) shows the results for the perpendicular geometry after including the effective angular acceptance as described in the text and in [27]. For the one-step model results, the correction was taken into account by numerically integrating spectra calculated at several angles.

	$h\nu$ = 6.5 keV				$h\nu$ = 700 eV
Atomic subshell	σ/e$^-$ (10^{-3} kb)	β	Parallel (10^{-3} kb)	Perp. (10^{-3} kb)	σ/e$^-$ (kb)
La $5p_{1/2}$	109	1.48	270	28.3	5.59
La $5p_{3/2}$	96	1.56	246	21.1	6.12
La $6s1/2$	9.75	1.99	29.1	0.06	0.74
La $5d_{3/2}$	8.33	0.95	16.3	4.36	4.01
Co $4s_{1/2}$	21.0	1.98	62.6	0.18	1.79
Co $3d_{3/2}$	1.53	0.34	2.06	1.27	10.5
Co $3d_{5/2}$	1.47	0.36	2.00	1.21	10.3
O $2p_{1/2}$	0.20	0.09	0.22	0.19	1.43
O $2p_{3/2}$	0.20	0.10	0.22	0.19	1.42

Table 3.1: Subshell photo-ionization cross-section (σ) at 6.5 keV and 700 eV deduced from [20, 22, 23]. σ is divided by the number of electrons in the subshell. β denotes the dipole parameter of the angular distribution. The cross-sections for parallel and perpendicular geometries are obtained by $\sigma[1 + \beta(1/4 + 3/4\cos(2\theta))]$, with $\theta = 0°$ and $\theta = 90°$ respectively.

Figure 3.4 displays the experimental HAXPES spectra together with the simulations for the HAXPES spectra using the cross-section analysis and the one-step calculations.

In the results for the parallel geometry, Fig. 3.4 a), we can observe a good agreement between the sum of the PDOS weighted by the respective photo-ionization cross-sections at 6.5 keV photon energy (middle panel) and the experimental spectrum (top panel). Unlike in SXPS, the simulations show that peak A is not the strongest feature in HAXPES spectrum, but rather features B-C1-C2. The reason for this is the very large relative contribution of the La 5*p*. This comes as a surprise since the weight of the La 5*p* PDOS is one order of magnitude smaller in comparison to that of the Co 3*d* or O 2*p* as shown in Fig 3.3 a). However, the photo-ionization cross-section of La 5*p* is about two orders larger than that of the Co 3*d* or O 2*p*, see Table 3.1. So in HAXPES we apparently are most sensitive to the tiny La 5*p* PDOS that are mixed into the valence band made of Co 3*d* and O 2*p* states. Finally, we can also observe that feature D is due to a Co 4*s* contribution, similar to

the appearance of the Ni 4*s* reported for HAXPES measurements on NiO [27], enhanced due to its larger cross-sections at higher photon energies (see Table 3.1).

Since the above mentioned analysis depends on small numbers (La 5*p* PDOS) multiplied by large numbers (La 5*p* cross-section), we need an independent verification for which the one-step method comes into play. The bottom panel of Fig. 3.4 a) shows the photoemission spectrum as calculated by this one-step method from the LDA results for $LaCoO_3$. We can clearly observe that the agreement with the experiment (top panel) is excellent. All spectral features are well reproduced in terms of energy positions and intensities. This supports the notion that indeed the La 5*p* PDOS is contributing strongly to the HAXPES signal despite its very small weight in the valence band. We would like to note that the one-step calculation reproduces the intensity of peak D much better than the cross-section analysis. At the moment we can only speculate that the inaccuracies in the cross-section analysis may originate from the fact that the assignments in terms of the various orbital PDOS may not be unique and rather depends on the wavefunctions basis set used in the band structure calculation, and that the orbitals are thus also different from the atomic ones used in the calculations for the photo-ionization cross-sections.

Next we will investigate the results for the perpendicular geometry. We can observe from Fig. 3.4 b) that also here there is a reasonable overall agreement between the sum of the PDOS weighted by the respective cross-sections (middle panel) and the experimental spectrum (top panel). The same observation can also be made for the spectrum calculated using the one-step model (bottom panel). In comparing the perpendicular geometry with the parallel geometry, the lower intensity of feature D in the experiment is reproduced by the simulations. This confirms that the Co 4*s* indeed contributes to the intensity of feature D in the parallel geometry, but is practically forbidden in the perpendicular geometry, see Table 3.1. The other important change, namely the increase of the intensity of peak A relative to that of features B-C1-C2 in going from parallel to perpendicular geometry is also reproduced in the simulations. Table 3.1 shows the reason why: the

La 5p has a considerably higher β-asymmetry parameter value than the Co 3d, meaning that the suppression of the signal in going from parallel to perpendicular geometry is stronger for the La 5p (factor 10 reduction) than for the Co 3d (factor two reduction). The fact that this lineshape change is highly visible in HAXPES supports again the notion that the La 5p is indeed important for the HAXPES signal.

3.1.1 Effective acceptance angle

A closer look at the simulations for the perpendicular geometry reveals, however, that the calculated intensity ratio of peak A vs features B-C-D is too large in comparison to the experimental one. This is the case for both the cross-section analysis and the one-step method calculations. The experiment does not show the expected factor of 10 reduction for the La 5p. A similar phenomenon has been previously reported [27]: in studying NiO, it was noted that the suppression of the O 1s core level and Ni 4s valence band intensity in going from the parallel to perpendicular geometry was very strong but not as complete as expected on the basis of the β parameter being very close to 2. This incomplete suppression was attributed to O 1s and valence band photoelectrons quasi-elastically scattered while traveling in the solid and yet arriving at the analyzer although they had a different direction when they were created by the photoelectric effect. That is, that a certain wider effective acceptance angle has to be considered.

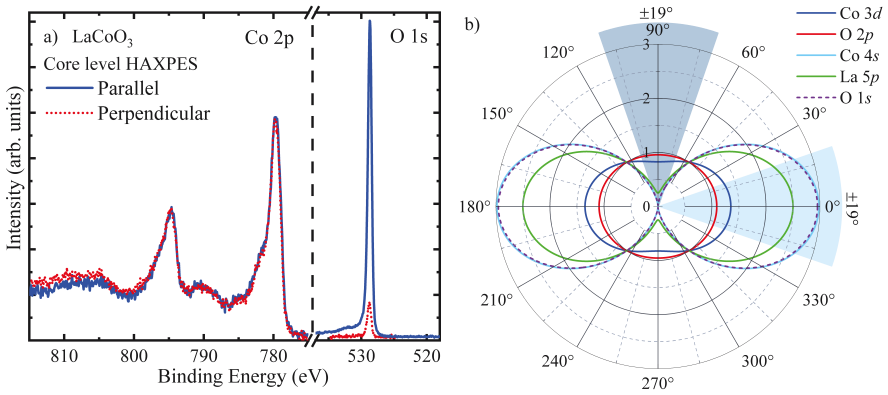

Figure 3.5: a) Co 2p and O 1s core level HAXPES spectra of $LaCoO_3$ with $\theta = 0°$ (parallel) and $\theta = 90°$ (perpendicular). The spectra has been normalized to the Co 2p core level peak intensities. b) Polar plot of the cross section angular dependence of the Co 3d, O 2p, Co 4s, La 5p, and O 1s orbitals at $h\nu = 6.5keV$ interpolated from refs. [20, 22, 23]. The shaded angular fans indicate the effective angular acceptance as a result of quasi-elastic scattering processes.

Fig. 3.5 a) displays the HAXPES Co 2p and O 1s core level spectra. The parallel vs. perpendicular spectra are normalized with respect to the Co 2p main peak intensity. Also here it is clear that the suppression of the O 1s in the perpendicular geometry is not complete. The tabulated angular dependence of the O 1s at $h\nu = 6.5$ keV [20, 22, 23] is plotted in Fig. 3.5 b) and gives clearly zero intensity for the perpendicular geometry.

To reproduce the experimentally observed finite intensity, we have to assign an effective angular acceptance $\pm\alpha$ to account for the presence of quasi-elastic scattering processes, i.e. we have to integrate the signal from θ=(90-α)° to θ=(90+α)° (followed by a normalization of 2·α° with α in rad) as illustrated by the grey shaded angular fan in Fig. 3.5 b). Analytically, we can determine this number by using the photo-ionization cross-section equation as described in chapter 2, but integrated in a $\pm\alpha$ range. The following expression is obtained [27]:

$$\frac{d\sigma}{d\Omega} = \frac{\sigma}{4\pi}\left[1 + \beta\left(\frac{1}{4} + \frac{3}{4}\cos(2\theta)\frac{\sin(2\alpha)}{2\alpha}\right)\right] \tag{3.1}$$

From the experimental core level spectra in Fig. 3.5 a), we obtain an α of about $\pm 19°$. We note that this $\pm 19°$ number is very similar as in the NiO case [27]. We also would like to point out that the consideration for quasi-elastic scattering effects is important for the perpendicular geometry but much less so for the parallel geometry since the *relative* variation of the intensity with angle is much larger in the perpendicular than in the horizontal geometry, i.e. compare the intensity variation in the grey shaded with that in the blue shaded angular fans in Fig. 3.5 b).

We now apply this $\pm 19°$ number also for the valence band simulation. The results are shown in the middle panel of Fig. 3.4 c). For the one-step calculation, the correction was achieved by calculating the spectra at $\theta \in \{90°, (90 \pm 9.5)°, (90 \pm 19)°\}$ followed by an interpolative numerical integration. The results are shown in the bottom panel of Fig. 3.4 c). We observe that we are now able to achieve a very good quantitative agreement to the experimental data, which proves that our approach is physically justified and thus verifies our conclusions.

3.2 Temperature and photon energy effects on the quasi-elastic scattering

This effective angle correction and in particular, the choice of the $\pm 19°$ angle is phenomenological, and in order to verify the consistence of the quasi-elastic scattering explanation we performed further experiments using different temperatures and photon energies. The results, after performing a common normalization to the Co $2p$ are shown in Fig. 3.6.

Here we can clearly observe that by increasing the temperature the perpendicular to parallel intensity ratio increases largely, as it would be expected from the scattering explanation. As for the comparison between photon energies, at 10 keV according to the cross-sections tables we would expect the ratio to decrease by around 1/3. In the experimental spectra, we can observe that the decrease is larger, being consistent with the increased forward focusing at higher energies. In order to better understand these

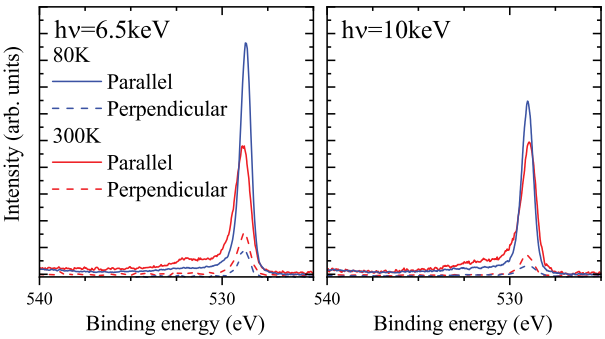

Figure 3.6: O 1s core level HAXPES spectra measured at 80K and 300K for both orientations using photon energies of $h\nu = 6.5$ keV and 10 keV. All spectra has been normalized to the Co 2p, as it was shown in fig 3.5

changes, we can calculate for each case the required value of α to get the experimental ratio to match with the theoretical cross-section formula. In figure 3.7, we show the the expected ratio in function of the energy for different α values. We can observe that for 80 K, the effective acceptance angle decreases from $\pm 19°$ at 6.5 keV to around $\pm 11°$ at 10 keV, meaning a significant decrease in quasi-elastic scattering processes. The 300 K data, however, shows a large increase of such scattering processes, as much larger α values of around $\pm 30°$ for 6.5 keV and $\pm 21°$ for 10 keV are required.

Finally, we will also include the second order non-dipolar terms that in the previous chapter were mentioned to be potentially relevant for HAXPES. We presented in our previous discussion that for the perpendicular geometry, in cases with β close to 2 (as it is the case of O 1s), the inclusion of these terms could lead into a significant lowering of the theoretical cross-section values. The dashed lines in Fig. 3.7 show the theoretical predictions once the second order non-dipolar terms are included in the equation. We can observe for α values larger than 11°, where all our experimental points lie, the inclusion of these higher order terms lead into a change of the effective acceptance angle of no more than 1° or 2°. In other words, second-order terms are less relevant when the quasi-elastic scattering processes take place and its consideration only result in a minor change in the choice of the effective acceptance angle.

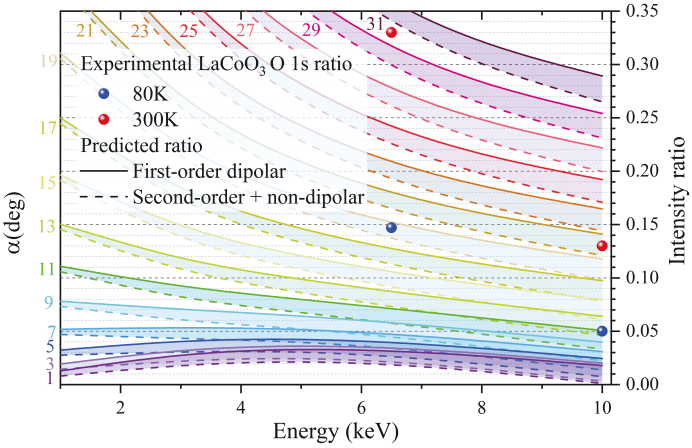

Figure 3.7: Expected intensity ratios of the O 1*s* core level spectra for different values for the effective acceptance angle α using the first-order cross-section equation and the second-order equation. The spheres show the experimentally observed ratios for the cases shown in fig 3.6.

3.3 Further examples and generalization

From the analysis performed in the previous section, we can reasonably assume that for $LaNiO_3$, which displayed the same trend as $LaCoO_3$, the same conclusion of having a dominant La 5*p* contribution can be drawn. We will now show some more examples to see to which extent the results can be generalized, or that is, for which type of compounds we could expect similar unexpected or undesired contributions.

In Fig. 3.8 (a) we show the HAXPES experimental valence band spectra of Ba_2CoO_4, together with a simulation based on the PDOS obtained from LDA calculations. The simulation does not intend to provide an accurate description of the electronic structure Ba_2CoO_4, but gives us an idea of the weight that the Ba orbital contributions may have in the valence band. Here we can observe that the Ba 5*p* appears to be clearly dominating and the Co 3*d* or O 2*p* are again negligible. In Fig. 3.8 (b) we observe the case of $YTiO_3$. Here, we can observe that while Ti 3*d* and O 2*p* constitute most of the spectral weight, the Y 4*p* is relevant enough to be required in any attempt of quantitative analysis.

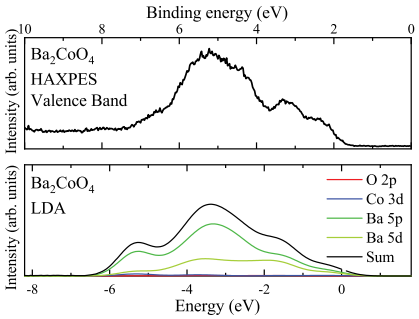

(a) (top) Experimental HAXPES valence band of Ba_2CoO_4, measured using the parallel geometry. (bottom) Simulation spectra by using broadened PDOS multiplied by their respective photo-ionization cross-sections at 6.5keV.

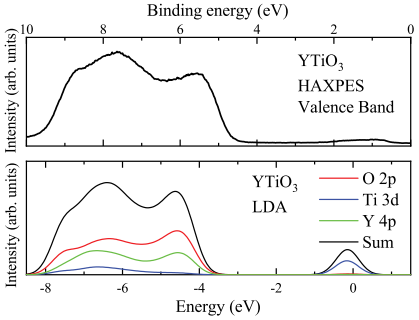

(b) (top) Experimental HAXPES valence band of $YTiO_3$, measured using the parallel geometry. (bottom) Simulation spectra by using broadened PDOS multiplied by their respective photo-ionization cross-sections at 6.5keV.

Figure 3.8: Examples of compounds with deep p states influencing the valence band spectra. The displayed simulation does not intend to provide an accurate description of the electronic structure of the compounds, but gives us an idea of the weight different orbitals have in the valence band spectra.

With these examples we conclude that such additional contributions are not restricted to the La $5p$ as observed in the $LaCoO_3$ or $LaNiO_3$ cases presented in the beginning of the chapter, but can be present in a wider range of types of compounds. In the three cases presented as examples, that is, La $5p$, Ba $5p$, and Y $4p$, the tabulated binding energies for the elemental case are all around the 25 eV-15 eV range [46]. Similar cases such as the $4p$ of Sr or Rb, or $5p$ of Ce or other rare earth elements may be expected to have a similar influence. It is important to note that the influence of these p orbitals with higher cross-sections in HAXPES can become a serious issue only when our interest lies in orbitals with very small cross-sections (such as the $3d$ in the $3d$ transition metals).

3.4 Conclusions

We have carried out a detailed HAXPES valence band study on $LaCoO_3$. We were able to disentangle the various orbital contributions to the spectra

using a combination of band structure calculations, photo-ionization cross-section analysis, and the one-step photoemission method. We discovered that the semi-core La 5*p* contributes significantly to the HAXPES valence band spectra. This is to be contrasted with valence band spectra taken with soft x-rays, where the Co 3*d* and O 2*p* spectral weights dominate. We also have shown how to reduce the La 5*p* signal in HAXPES as to enhance relatively the Co 3*d* by choosing the so-called perpendicular geometry. We have further shown that the one-step photoemission method provides an excellent description of the HAXPES valence band spectra and their polarization dependence. Analysis on the basis of photo-ionization cross-sections yields also highly satisfactory results, which is important since this requires less computing efforts than the one step calculations and is also applicable to evaluate strongly correlated systems for which band structure calculations are generally not adequate. We also show that an accurate quantitative description of the polarization dependence in the HAXPES spectra can be achieved if quasi-elastic scattering effects are taken into consideration. Measuring at higher temperatures result in an significant increase on the amount of scattering effects, while using higher photon energies decreases them. At 10 keV and 80 K, the scattering effects are still significant enough to require an effective angle corrections. Finally, we have shown that these results for $LaCoO_3$ provide a more general conclusion, that is, the importance of taking into account the semi-core 4*p* or 5*p* of some elements such as Y, Sr, Ba or rare earths due to their large photo-ionization cross-sections that can overcompensate the tiny contributions, turning them into relevant, or even dominating contributions.

Chapter 4

Charge transfer energy in iridates

The results presented in this chapter are published in:

Phys. Rev. B 102, 045119 (2020).

In the previous chapter we have demonstrated the vital importance of the photoionization cross-sections for the valence band spectra, and that in some cases, undesired contributions can overwhelm the spectra, hampering the analysis of the electronic states of interest. In this chapter, we will present results of an opposite case, in which the large cross-sections of the iridium 5*d* states dominate all other contributions, facilitating the study of its electronic structure in a large series of iridates with many different ions involved.

4.1 Iridates: an introduction

Iridium oxides, or iridates, have attracted a lot of attention due to the expectation for exotic magnetic states arising from the interplay between strong spin-orbit coupling, crystal field, and Coulomb interactions. Spin-orbit coupling is the relativistic interaction between the spin of an electron and its orbital, and is important for its role in entangling the spin and orbital degrees of freedom. The strength of the spin-orbit coupling may be small enough to be ignored in lighter elements, but it becomes larger for heavier atoms, and in the case of 5*d* transition metals such as iridium, the energy scale becomes comparable to the strength of the crystal field, and Coulomb interactions. When these interactions compete, small changes in

the balance of the strength in the different interactions can lead to a very rich family of behaviours.

In the case of the iridium oxide compounds with octahedral symmetry, in an ionic scenario, the crystal field splits the $5d$ states in a t_{2g} triplet and a e_g doublet, ignoring the spin degrees of freedom. Then, the spin-orbit coupling splits the t_{2g} triplet into a doublet with $j_{eff} = 1/2$ and a quadruplet with $j_{eff} = 3/2$ (see Fig. 4.1). For compounds with the formal Ir^{5+} valency ($5d^4$), this picture leaves the $j_{eff} = 3/2$ bands fully filled while the $j_{eff} = 1/2$ doublet remains empty. We then obtain a non-magnetic Van Vleck singlet ground state with $J_{eff} = 0$ [47–49], in which the spin-orbit coupling creates a gap and the magnetic properties are determined by the virtual transitions to higher levels. This would allow the possibility of the presence of excitonic magnetism in such systems [50]. Experimental studies reported indeed unusual magnetic behavior in Ir^{5+} compounds such as Sr_2YIrO_6 and Ba_2YIrO_6 [51, 52]. However, the origin of such behaviour and the possibility for the materialization of such excitonic magnetism are still subject to debate [53–57].

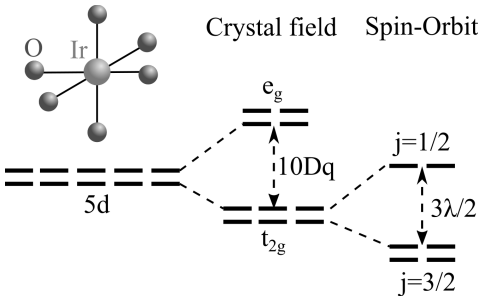

Figure 4.1: An illustration of the splitting of the $5d$ levels of iridium in an octahedral coordination by the crystal field and the spin-orbit coupling. Under an ionic t_{2g}-only assumption, iridates with formal Ir^{5+} valency, the $j = 3/2$ band is fully filled while $j = 1/2$ remains empty, producing a Van Vleck ground state with $J_{eff} = 0$. Under the same assumptions, iridates with formal Ir^{4+} valency will have a half-filled $j = 1/2$ producing a pseudospin $J_{eff} = 1/2$ Mott insulating state.

For iridates with the formal Ir^{4+} valency ($5d^5$), and still assuming that the conditions to obtain the scenario described in Fig. 4.1 are met, the t_{2g} states split into a fully filled $j_{eff} = 3/2$ band and a half filled $j_{eff} = 1/2$ band, leading to a pseudospin $J_{eff} = 1/2$ Mott insulating state as a ground state in the Ir^{4+} ions [58]. Here it is also assumed that the small Hubbard U

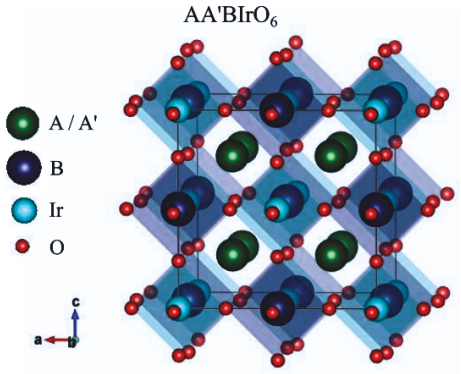

Figure 4.2: Crystal structure of the double perovskite AA'$BIrO_6$. Red spheres correspond to the position of oxygen atoms, the dark green spheres to the A and A' sites. Cyan and dark blue octahedra correspond to the IrO_6 and BO_6 octahedra, respectively.

value for the Ir 5*d* is still larger than the effective one-electron bandwidth for the Ir 5*d* t_{2g}. In certain lattices such as the honeycomb lattice, the nearest-neighbor $J_{eff} = 1/2$ states can interact via a strongly anisotropic Ising exchange. In such lattices, these exchange interactions strongly compete, leading the system into a quantum spin-liquid phase. Such systems are described by the Kitaev model [59–61], and an extensive work has been performed on various candidate materials [62, 63]. However, it turned out that perturbations from the ideal cubic coordination or longer range hopping can introduce other types of intersite exchange interactions masking the long-sought pure Kitaev phenomenon [64].

In this context, double perovskite iridates of AA'$BIrO_6$ form, the crystal structure of which is displayed in Fig. 4.2, provide a very interesting playground for the search and development of materials with novel magnetic and electric properties [65]. This structure is closely related to the ABO_3 perovskite structure, but with a 50% substitution of the ion on site B (and in some cases, also site A). This provides alternated octahedras of IrO_6 and BO_6, and therefore, it results in large Ir-Ir interatomic distances. The Ir-Ir distances are then much larger compared to the honeycomb systems, which reduces delocalization (i.e. band formation) and leads to better defined

local $J_{eff} = 1/2$ entities. Furthermore, the substitution of the A, A' and B sites allows for a tuning of the different competing interactions, local symmetries, and ligand environment as well as the oxidation state of the iridium. A significant amount of research has been reported during the last years [47–49, 51–57, 66–73]. A new class of face-centered-cubic materials for Kitaev physics has been suggested based on the double perovskite iridates [67, 69, 70, 72].

While the larger Ir-Ir distances and the chemical and concomitant structural tunability offered by the double perovskite structure are indeed a step forward towards the necessary conditions for the realization of the Kitaev model, another issue remains to be addressed. As it has been argued in the case of Sr_2IrO_4 [74], covalency may be expected to be large in iridates generally. The assumption of an ionic t_{2g}^5 $J_{eff} = 1/2$ state, therefore, may become increasingly questionable for larger hybridization strengths.

4.2 Methods

In this study, our main focus is on the issue of covalency and less on the aspects that are the result of the small structural variations or the magnetic properties of the B site cations. Therefore, a wide range of double perovskite iridates is studied in order to be able to find out the general features or characteristics of this class of materials as a whole. With the formal Ir^{4+} valency, we will show the results of La_2BIrO_6, with B = Mg, Co, Ni and Zi, and with the formal Ir^{5+} valency, Ba_2YIrO_6, Sr_2YIrO_6, Sr_2FeIrO_6, Bi_2NaIrO_6 and $SrLaBIrO_6$, with B= Ni, Zn.

The experimental technique for the study is HAXPES. As discussed in the previous chapters, the large probing depth characteristic of HAXPES allows us to obtain spectra that are representative of the bulk material. In addition, at high photon energies the photoionization cross-sections of the Ir 5*d* are much larger than those of the other orbitals from lighter elements contributing to the valence band [20, 22, 23]. We thus can expect that our spectra directly unveil the Ir 5*d* contributions [75, 76].

Furthermore, another relevant advantage of using photoelectron spectroscopy in comparison to absorption based spectroscopies is that photoemission has a much higher sensitivity to covalency [77], which is the main focus of this study.

All HAXPES experiments presented in this chapter were performed at the BL12XU beamline, already described earlier in chapter 2. The overall energy resolution was set at around 0.3 eV. All measurements were performed in the horizontal geometry at 80 K except for the $SrLaNiIrO_6$ and Sr_2YIrO_6, which were performed at 300 K.

The experimental data are complemented with *ab-initio* density functional calculations and subsequent downfolding to effective localized Wannier bases, in order to get a quantitative understanding of the local electronic structure of the iridium in the double perovskite iridates. The ab-initio calculations were perfomed with FPLO [78]. For the derivation of the effective hopping integrals we downfolded to a lattice basis of Wannier functions including O $2p$, $2s$ and Ir $5d$ orbitals. In order to translate the numerical downfolding results into analytical hopping terms, we mapped the model to a Slater-Koster tight-binding model on a linear combination of atomic orbitals (LCAO) basis [79] which consists of O $2p$, $2s$, and Ir $5d$ orbitals and optimized to match the experimental spectra.

4.3 HAXPES spectra and ab-initio calculations

Figure 4.3 shows the HAXPES valence band spectra of the selected double perovskite iridates. We can observe that all measured samples have no or negligible spectral weight at the Fermi level (zero binding energy), consistent with their insulating behaviour. Remarkably, all spectra look rather similar: there are two main features, namely a rather narrow peak at around 1 eV binding energy (labelled α), and a broader structure between 6 and 8 eV (labelled β_1/β_2), with some low intensity in between. The main difference observed between the Ir^{4+} (left panel) and Ir^{5+} (right panel) compounds is the intensity ratio between these two features. For the Ir^{4+} samples both

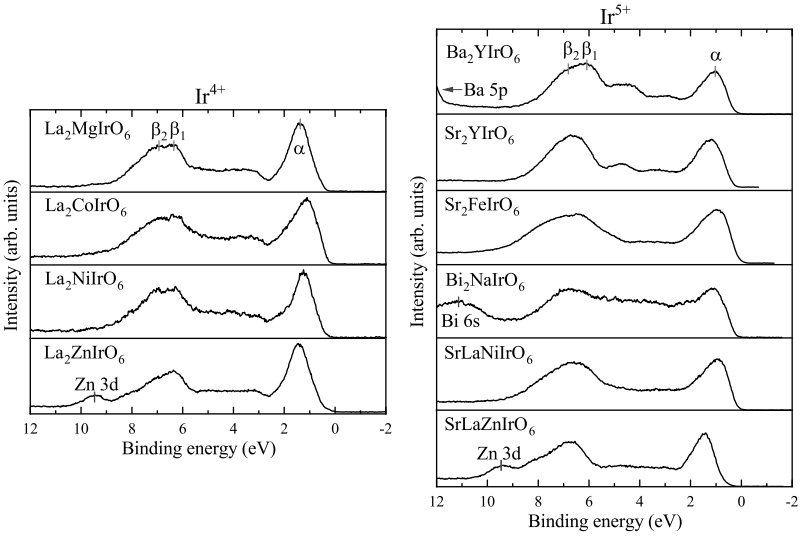

Figure 4.3: Valence band HAXPES spectra ($h\nu = 6.5$ keV) of the double perovskite compounds containing formally Ir^{4+} (left panel) and Ir^{5+} (right panel) ions.

features have a similar integrated intensity, while for the Ir^{5+} samples the β_1/β_2 features are more intense.

The fact that the presence of the different B cations (e.g. Mg, Y, Fe, Co, Ni) has little effect on the overall line shape of the spectra, suggests that the spectra are dominated by the contribution from the iridium orbitals. Indeed, the tabulated photo-ionization cross-section values for the Ir 5*d* orbitals are by far the largest in comparison to those of the transition metal 3*d* and the O 2*p* for x-rays with 6.5 keV energy as we have used in our HAXPES experiment [20, 22, 23]. We can in fact deduce now already that the features α and β_1/β_2 are displaying the Ir 5*d* PDOS and that this Ir 5*d* PDOS is rather similar across the set of compounds independent of the nature of the B cation, which by itself is quite remarkable.

In order to better understand the electronic structure of these iridates, we performed DFT calculations and projected out the different orbital contributions to the valence band. Figure 4.4 shows the density of states (DOS) and the partial density of states (PDOS) of the Ir 5*d* e_g and t_{2g}, O

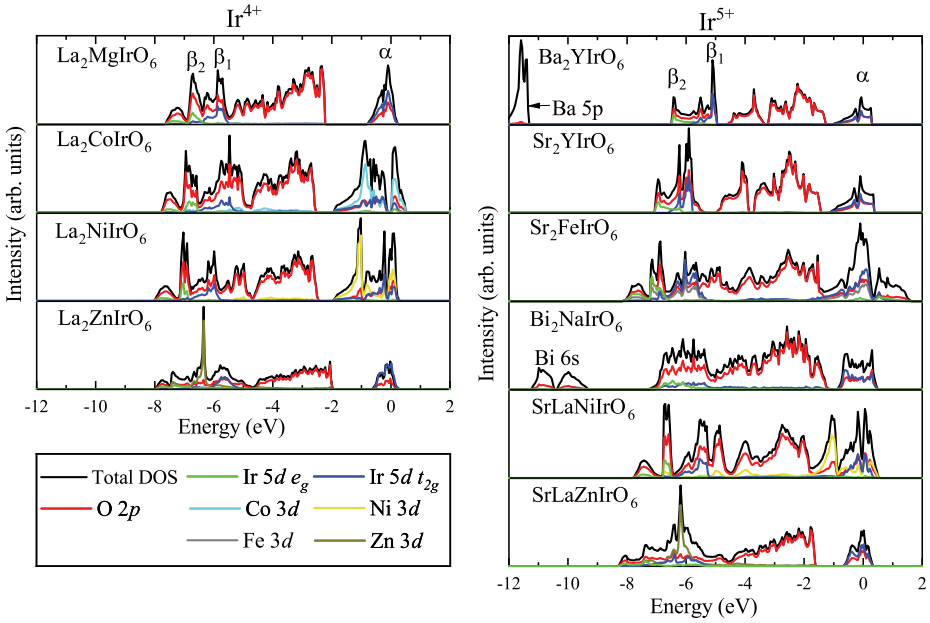

Figure 4.4: Calculated density of states (DOS) and the Ir 5*d* , O 2*p*, and transition metal 3*d* partial density of states (PDOS) of the double perovskite compounds with Ir^{4+} (left panel) and Ir^{5+} (right panel).

$2p$, as well as the $3d$ from the other transition metals on the B site. We observe that the Ir $5d$ density is mostly located in the same regions as the main two features α and β_1/β_2 observed in the experimental spectra. The O $2p$ is present throughout the entire valence band, not only where the Ir $5d$ is present but also in the region between the two iridium features.

As for the contribution from the $3d$ orbitals, the intensity for the Co and Ni compounds is mostly slightly below the iridium states close to the Fermi energy, for the Fe compound it is more evenly distributed, while the Zn compound it is close to the deeper iridium states. Here we note that the calculated energy position of the Zn $3d$ states deviates from the experiment. This is a short-coming of standard DFT calculations, and the inclusion of self-interaction effects is required to reproduce properly the spectra of ZnO and related materials [80]. We also note that all DFT results produce a metallic state and that therefore electron correlations effects need to be included [54] in order to reproduce a gap associated with the experimentally observed insulating behaviour of the compounds. Yet, the DOS and PDOS results are useful for our study since the purpose of our DFT calculations is to gain insight into single-particle processes like hybridization and crystal field splittings rather than reproducing the small bandgaps.

In order to compare the DFT results to the experiment, we calculate the valence band spectra by multiplying each of the PDOS by their respective photoionization cross section at 6.5 keV photon energy as derived from Refs. [20, 22, 23] and by the Fermi function to include only the contributions from the occupied states, followed by a broadening to account for the experimental resolution and their summation. This was done for all the PDOS included in the calculation (not only the ones shown in the figures). Finally, the obtained spectra have been shifted rigidly to match the position of the experimental α feature and to simulate the experimentally observed gap. The results are shown in Figure 4.5.

We can notice first of all, that in all cases most of the intensity originates indeed from Ir 5d states. The contributions of O $2p$ and also of transition metal $3d$ orbitals are negligible in all cases. The remaining weight can be attributed to states not explicitly represented in this plot, which are mostly

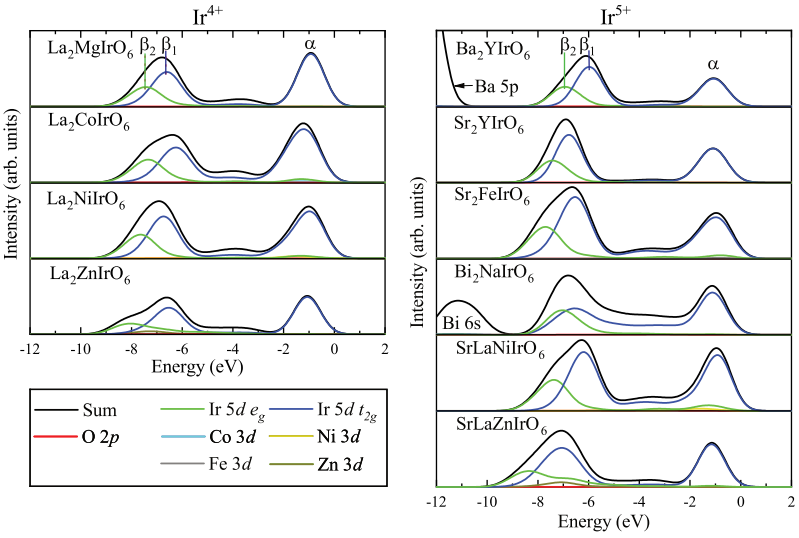

Figure 4.5: Calculated valence band spectra of the double perovskite compounds with Ir^{4+} (left panel) and Ir^{5+} (right panel). The spectra were obtained by multiplying the calculated PDOS of the occupied states by their respective photoionization cross sections at 6.5 keV photon energy, followed by a broadening to account for experimental conditions, and then their summation. Finally, a rigid shift is applied to simulate the gap.

p states from Ba, La, Y, or Sr, which become much more relevant when measuring using hard x-rays [28].

Comparing the calculated with the experimental spectra we find good overall agreement. There are some deviations when looking in more detail, for example, the shapes and positions of the features are not completely reproduced. Also, in some cases, the intensity in the region between the two main features is somewhat underestimated, which could be due to an underestimation of some of the cross-sections. Nevertheless, it is safe to state that the overall experimental spectral features are well explained by the calculations. In particular, we observe that the materials trend for the intensity ratios of the two features α vs. β_1/β_2 when comparing the Ir^{4+} and Ir^{5+} set of compounds is well captured by the calculations.

4.4 Tight-binding parametrization

In order to extract the dominant hopping parameters on a minimal basis, we perform Slater-Koster LCAO tight-binding modelling on the experimental spectra. As representative compounds for this more detailed study we take La_2MgIrO_6 for Ir^{4+} and Ba_2YIrO_6 for Ir^{5+}, i.e., systems which do not contain $3d$ transition metal ions which otherwise could complicate the analysis due to typically very strong correlation effects within the $3d$ shell.

To this end we start by numerical downfolding of the converged DFT Kohn-Sham bands to a Wannier orbital basis. Besides Ir $5d$ and O $2p$ states we included also O $2s$ states. The reason for this inclusion is a non-negligible hybridization between O $2s$ and the $5d$ e_g states of iridium. If such hybridization effects were included only implicitly, it would lead to a renormalized (enlarged) effective crystal field splitting by shifting the Ir $5d$ e_g states to higher energies (even before considering any hybridization effects with O $2p$ states). Our choice for the explicit inclusion of O $2s$ states can be, hence, understood as the intention to stay as close as possible to an atomic basis for our tight-binding analysis.

In our model, we distinguish two different types of O $2p$ orbitals, as hopping integrals vary depending on the symmetry of the corresponding

On-site energies (eV)

	$p_{\sigma 0}$	$p_{\pi 0}$	s_0	d_{eg0}	d_{t2g0}
La_2MgIrO_6 (LDA fit)	-3.950	-2.370	-17.370	-2.120	-2.480
La_2MgIrO_6 (exp. fit)	-3.210	-1.630	-16.630	-1.380	-1.740
Ba_2YIrO_6 (LDA fit)	-3.767	-2.437	-16.600	-2.310	-2.590
Ba_2YIrO_6 (exp. fit)	-3.602	-2.272	-16.435	-2.145	-2.425

Hopping integrals (eV)

	$sp\sigma$	$sd\sigma$	$ss\sigma$	$pp\sigma$	$pp\pi$	$pp\pi_1$	$pd\sigma$	$pd\pi$
La_2MgIrO_6 (LDA fit)	0.4	-2.4	-0.16	0.48	-0.22	-0.10	-2.90	1.45
La_2MgIrO_6 (exp. fit)	0.4	-2.4	-0.16	0.48	-0.22	-0.10	-2.90	1.15
Ba_2YIrO_6 (LDA fit)	0.4	-2.9	-0.16	0.42	-0.12	-0.01	-2.66	1.33
Ba_2YIrO_6 (exp. fit)	0.4	-2.9	-0.16	0.42	-0.12	-0.01	-2.71	1.23

Table 4.1: Tight-binding parameters for La_2MgIrO_6 and Ba_2YIrO_6, as obtained from the downfolding (LDA fit) and after fine tuning to match the experimental features (exp. fit).

bond. O $2p$ σ orbitals, which are aligned along the Ir-O direction and hybridize mostly with the Ir $5d$ e_g, and O $2p$ π orbitals, which are aligned perpendicularly and hybridize mainly with the Ir $5d$ t_{2g} states.

The DFT calculations with the projected Ir $5d$ e_g/t_{2g} and O $2s$, $2p$ σ/π PDOS are shown in Figs. 4.6 (a) and (b) for La_2MgIrO_6 and Ba_2YIrO_6 respectively. For feature α at 1eV binding energy from the experiment (see Fig. 4.3) we observe a clear Ir $5d$ t_{2g} character. This is also true for feature β_1 at 6.2 eV. Feature β_2 at 7 eV, on the other hand, originates entirely from Ir $5d$ e_g states. All features have appreciable O $2p$ π and σ character, respectively.

The results of the tight-binding calculations using the parameters as obtained from the downfolding (Table 4.1) are displayed in panels (c) and (d). We observe that the tight-binding results reproduce the PDOS of Ir $5d$ found in DFT well. This implies that the most relevant hopping processes for the Ir $5d$ states are captured by our minimal tight-binding model. This also means the cations of the A and B sites do not play a significant direct role on the Ir $5d$ states. Starting from this set of parameters, we can adjust

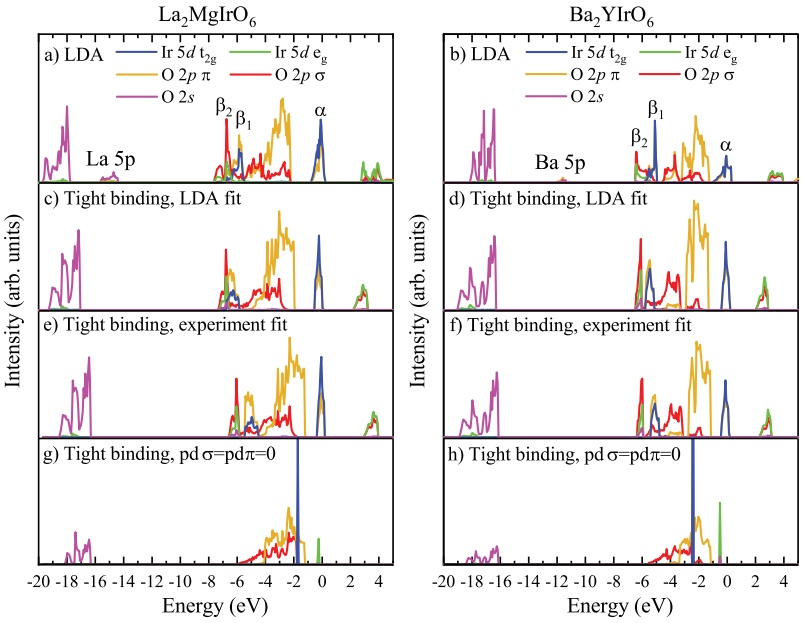

Figure 4.6: (a) and (b): Comparison of the DOS and PDOS obtained from the *ab initio* calculations and the tight binding calculations for La_2MgIrO_6 (left panel), chosen as a representative compound for the double perovskites with Ir^{4+}, and Ba_2YIrO_6 (right panel), as representant for the double perovskites with Ir^{5+}. O $2p$ π (σ) corresponds to the contribution of the O $2p$ orbitals perpendicular (parallel) to the Ir-O direction. (c) and (d): Results of the tight binding calculations using the parameters obtained from the downfolding of the *ab initio* calculations. (e) and (f): Results after fine tuning of the parameters to match the experimental spectra (Table 4.1). (g) and (h): Results of the tight binding calculations performed with the fine tuned parameters but with $pd\pi = pd\sigma = 0$, i.e., with the hybridization between Ir $5d$ and O $2p$ switched off.

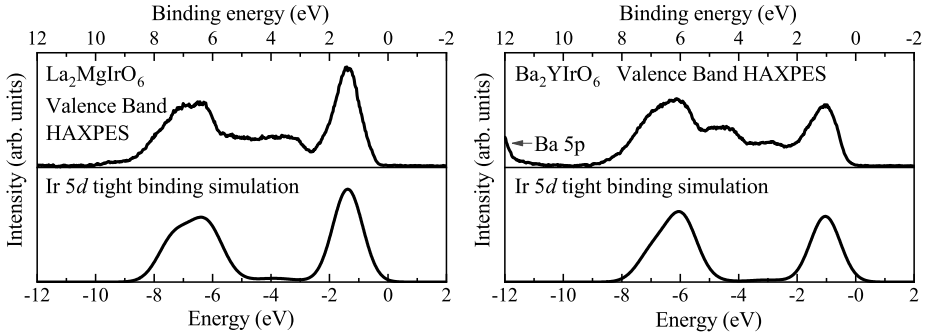

Figure 4.7: Comparison of the experimental HAXPES spectra (top) with the simulated Ir 5*d* valence band spectrum based on the optimized tight binding calculations (bottom) for La_2MgIrO_6 (left panel) and Ba_2YIrO_6 (right panel).

them in order to get a better match to the experimental spectra and thus obtain the parameters that describe best what we have observed in our measurements.

Figs. 4.6 (e) and (f) are the results after fine tuning the parameters in order to get the separation between features α and β_1/β_2 to match the experiment. Fig. 4.7 shows the comparison of the experimental spectra with the Ir 5*d* contribution obtained with this optimized set of tight-binding parameters. The same procedure as described for the data in Fig. 4.5 is used to simulate the experimental conditions. The effect of the photoionization cross-sections is effectively already taken into account since we are looking into the Ir 5*d* only, and its contribution is by far the dominant one for the HAXPES spectra. We can observe that the Ir 5*d* PDOS replicates very well the features from the experiment.

Finally, Figs. 4.6 (g) and (h) are the results of the calculations using the set of parameters for the experimental fitting but with $pd\pi = pd\sigma = 0$, i.e., with the hybridization between the Ir 5*d* and O 2*p* switched off. These plots reveal most clearly the effect of hybridization process between the Ir 5*d* and the O 2*p*. We can see that the Ir 5*d* t_{2g} and e_g states in (g) and (h) become delta-function like which implies that inter-site iridium hopping is small and that most of the Ir 5*d* band formation is due to the hopping via the O 2*p* orbitals. Most interesting is the energy position of the Ir 5*d* states

when the hopping is set to zero: the Ir 5d t_{2g} fall inside the O 2p π band. For the Ir^{4+} case (g), t_{2g} is at the upper half of this oxygen band, and for the Ir^{5+} (h), it is even in the middle. In other words, the O 2p π and the Ir 5d t_{2g} states are nearly degenerate in the Ir^{4+} system and fully degenerate in the Ir^{5+} material.

With these findings we get a clearer picture of the hybridization process between the O 2p and the Ir 5d t_{2g}. As it can be seen from Figs. 4.6 (e) and (f), bonding (feature β_1) - antibonding (feature α) bands are formed with about 5 eV energy separation. This separation is much larger than the separation between the O 2p π band and the Ir 5d t_{2g} states before the hybridization, which is about 2 eV for the Ir^{4+} systems and 0 eV for the Ir^{5+}, as shown in Figs. 4.6 (g) and (h), respectively. The hopping integral is thus much larger than the difference in the O 2p π and Ir 5d t_{2g} on-site energies. Consequently, the bonding and antibonding states have highly mixed O 2p π and Ir t_{2g} characters. The simulations in Figs. 4.6 (e) and (f) show that the antibonding peak at 1 eV binding energy has a 60% Ir 5d t_{2g} character in the Ir^{4+} systems and 50% in the Ir^{5+}.

In the case of the e_g states, they are positioned at higher energies (closer to the Fermi level) than the t_{2g}, and thus more separated from the O 2p σ bands before hybridization, see Figs. 4.6 (g) and (h). Yet, even on the scale of this Ir 5d e_g O 2p splitting, their σ hopping integrals are so large, that the energy separation between the resulting bonding (feature β_2) and anti-bonding (above the Fermi level) states reaches values of about 10 eV, see Figs. 4.6 (e) and (f). The hybridized states have a 50-50 mixed character. In other words, also the Ir 5d e_g and the O 2p σ bands are effectively degenerate.

In developing models which include electron correlation effects and the spin-orbit entanglement explicitly in order to describe the (potentially) exotic magnetic properties, the degeneracy of the O 2p and Ir 5d states translates into a value for the O 2p to Ir 5d charge transfer energy which is essentially zero. As a result, the assumption of an ionic t_{2g}^5 configuration in order to stabilize the pure $J_{eff} = 1/2$ state for Kitaev physics can no longer be justified. There will be a substantial oxygen ligand hole character in

the Ir 5d t_{2g} Wannier orbitals and this extremely strong covalency must be taken into account in the quantitative evaluation of the models. This has far reaching consequences. Additional inter-site magnetic exchange interactions will be present, i.e. not only of the Kitaev type. Moreover, the exchange interactions will become very long-ranged [74, 81], leading also easily to anisotropies not foreseen in the Kitaev model. Nevertheless, it is still quite feasible to design materials that show a spin-liquid behavior, provided that the exchange interactions present can be tuned such that they compete and sufficiently cancel each other [62, 64, 82].

4.5 Conclusion

We have measured the valence band of several A_2BIrO_6 and AA'$BIrO_6$ double perovskites containing either Ir^{4+} or Ir^{5+}. The spectra display very strong similarities as far as the Ir 5d contribution is concerned, pointing out common aspects in the O 2p and Ir 5d hybridization process. Density functional theory calculations and Slater-Koster LCAO tight-binding calculations provide a detailed explanation of the spectra and demonstrate that the iridates are highly covalent systems with essentially zero O 2p to Ir 5d charge transfer energy. The consequence is that the exchange interactions become very long-ranged, thereby inhibiting the materialization of the pure Kitaev model. Nevertheless, it still would be possible to realize a spin-liquid system using the iridates with a proper tuning of the various competing exchange interactions.

Chapter 5

Paramagnetic LaCoO3: An inhomogeneous mixed spin-state system

$LaCoO_3$ is a non-magnetic insulator at low temperatures, and it shows a gradual transition to a paramagnetic state upon increasing the temperature [83]. While the non-magnetic state can be assigned to the low-spin (LS) t_{2g}^6 configuration, there is a considerable debate about the nature of the excited states. Originally, a gradual occupation of a high-spin (HS) $t_{2g}^4 e_g^2$ state was proposed but an alternative intermediate-spin $t_{2g}^5 e_g^1$ scenario that was suggested in 1996 by Korotin et al. based on a theoretical study with LDA+U calculations [84] gained also significant attention. A more recent study in 2006 by Haverkort et al.[42] established using X-ray absorption spectroscopy (XAS) and X-ray magnetic circular dichroism (XMCD) that the paramagnetic state is formed from a mixture of LS and HS. In order to understand better the behaviour of the electric and magnetic properties of $LaCoO_3$ with temperature, it is important to understand how does this LS/HS mixture is coupled to the lattice. This may be of importance for the search for any sort of ordering between the LS and HS sites, as originally proposed by Goodenough et al. [39, 40].

In this chapter we will present temperature dependent valence band and core level HAXPES, and O-K X-ray absorption spectra and analyze the data using detailed cluster model calculations. We will show that it is necessary to use a different set of parameters for the LS and HS sites, accounting for the structural expansion of the HS sites at higher temperatures.

The HAXPES spectra were measured at the BL12XU beamline in the vertical geometry as already discussed in previous chapters. The photon

energy was $\hbar\nu = 6.5$ keV and the overall energy resolution was 0.35 eV. The spectra were normalized to the total integrated intensity after the background due to secondary electrons has been subtracted. The O-K XAS measurements were performed at the Dragon beamline of the NSRRC in Taiwan. The bulk-sensitive fluorescence-yield mode was used at a photon-energy resolution of 0.25 eV. XAS spectra of NiO were also measured for energy calibration. The XAS spectra were normalized to the average spectral intensity in the energy range 556-570 eV, after the subtraction of the pre-edge background.

5.1 Cluster calculations

Full multiplet configuration-interaction cluster calculations of the cluster model CoO_6 were performed with the software xtls 9.25 [85]. The parameters for the calculations are, in units of eV, $\Delta = 2.0$, $U_{dd} = 5.5$, $U_{dp} = 7.0$, $pd\sigma = -1.67$, and $pd\pi = 0.78$. A combination of Gaussian and Lorentzian broadening has been applied to compare the calculations with the experimental spectra.

The spin state of the ground state is determined by the choice of the value of the ionic crystal field $10Dq$, and in our case we chose $10Dq = 0.75$ to obtain a low spin (LS) ground state and $10Dq = 0.40$ to obtain a high spin (HS) ground state. It is, however, also possible to calculate the HS spectra by using the LS set of parameters by calculating its excited states, and similarly, the LS spectra can be obtained as an excited state [42]. In order to verify if any differences are present depending on the chosen method to simulate the LS / HS spectra, the results that are achieved for the PES / IPES spectra using both are compared in Fig. 5.1. We observe that for all spectra both approaches give essentially the same results with only very minor differences. In the following sections, the LS spectra that are presented have been calculated from the LS ground state and the HS spectra from the HS ground state.

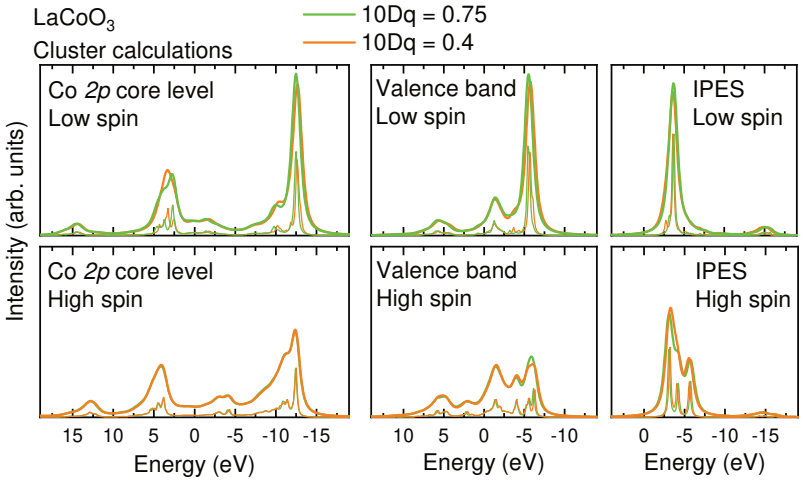

Figure 5.1: Cluster calculation results for the $LaCoO_3$ Co $2p$ photoemission core level, valence band and the inverse photoemission spectra, corresponding to the low spin (top) and high spin states (bottom). For $10Dq = 0.75$ (in green), the ground state results provide the low spin spectra while the high spin spectra was obtained from the excited states. For $10Dq = 0.40$ (in orange), the high spin spectra corresponds to the ground state results while the low spin results are from an excited state.

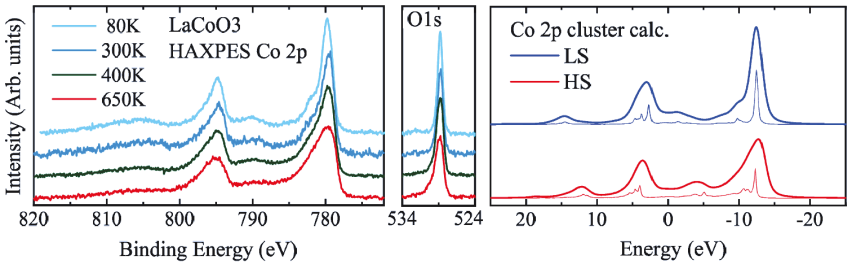

Figure 5.2: Co $2p$ (left) and O $1s$ (middle) HAXPES spectra measured on $LaCoO_3$ at different temperatures. (right) Cluster calculations of the Co $2p$ photoemission spectra of $LaCoO_3$ assuming the LS and HS initial states.

5.2 Core level spectra

In Fig. 5.2 we report the HAXPES spectra of Co $2p$ and O $1s$ core levels measured on $LaCoO_3$ at different temperatures, together with the calculated $LaCoO_3$ Co $2p$ core level spectra.

The Co $2p$ core-hole spin-orbit coupling splits the spectrum roughly in two parts, namely the Co $2p_{3/2}$ (main line at 779.7 eV and charge transfer satellite at 790 eV) and Co $2p_{1/2}$ (main line at 794.8 eV and charge transfer satellite at 805.5 eV) regions. At 80 K the Co $2p_{3/2}$ main line is quite narrow, with a shoulder at about 1.9 eV higher binding energy with respect to the main line, and a charge-transfer satellite at about 11 eV higher binding energy with respect to the main line. Such features are well captured in the calculated spectra with LS initial state, as shown on the right panel of Fig. 5.2, confirming the mainly LS state at 80 K.

As the temperature is increased, the main lines become very broad and very asymmetric. One could argue that this strong change in shape of the Co $2p$ spectrum is simply a temperature broadening effect due to phonons. However, if one looks to the temperature evolution of the O $1s$ spectrum reported in Fig. 5.2, then one can see that the broadening produced here by warming up the sample is much smaller than that observed in the Co $2p$ spectrum. At high temperature the O $1s$ line also exhibits an increasing asymmetry, but this is nothing in comparison with the much stronger line asymmetry of the Co $2p$ spectrum. The asymmetry of the O $1s$ is probably

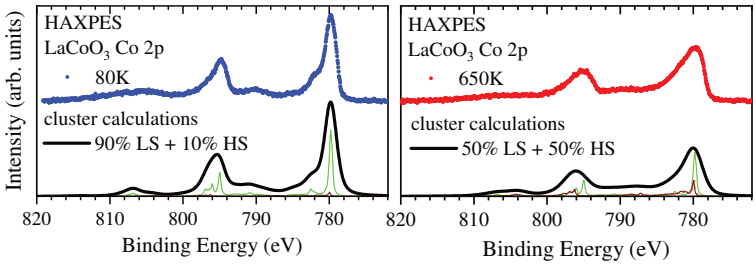

Figure 5.3: Cu 2*p* HAXPES experimental spectra at 80K (left) and 650K (right) together with a theoretical fit. The fit is done by incoherently summing the results obtained with a full-multiplet configuration-interaction cluster calculations of the Co 2*p* photoemission spectra of $LaCoO_3$ assuming the LS and HS initial states. The ratio of the mixing was chosen according to the LS-HS ratios as found in [42].

simply caused by the presence of electron-hole pair excitations upon the creation of the core hole, i.e., screening of the core hole by conduction-band electrons. This phenomenon is known as Doniach-Sunjic asymmetry and is present in metals [86]. Therefore the high-temperature asymmetry of the O 1s spectrum reflects the fact that the system is increasingly less insulating and finally under goes the MIT at around 500 K.

In the Co 2p spectrum, instead, the strong enhancement of both the line width and the asymmetry can be well explained with the increase of the amount of HS states. With increasing temperature, the experimental spectra gains resemblance to the calculated HS spectra, as shown in Fig. 5.2. Such trend can be observed not only in the main peaks but also in the gradual loss of intensity in the charge-transfer satellite at 790 eV, and the increase in intensity at around 788 eV, where the satellite is located in the HS state.

In order to quantitatively analyze the experimental spectra, we perform an incoherent sum of the LS and HS spectra. We show that with such incoherent sum method we can achieve a quite accurate fit, shown in Fig. 5.3. The LS-HS ratios used are for the 80 K spectrum 90% LS and 10% HS, and for the 650 K spectrum 50% LS and 50% HS. The LS-HS ratios obtained here are the ones found previously by Haverkort et al. [42]. Here we note that the HS spectrum has been calculated including a 15%

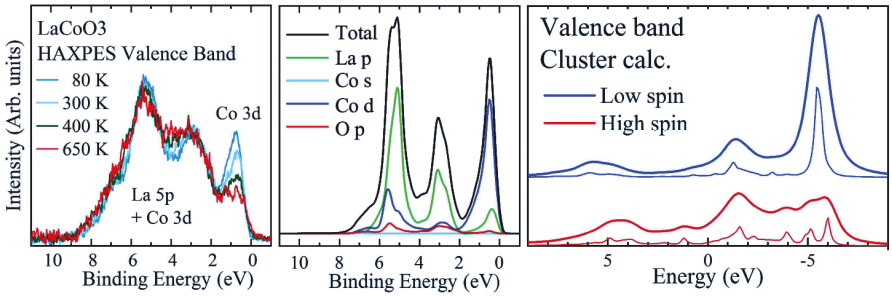

Figure 5.4: (Left) Temperature dependence of the bulk- sensitive HAXPES spectra of the valence band of $LaCoO_3$. The strong variations of the spectral feature near the Fermi energy is the sign of the LS-to-HS transition. (Middle) Simulated spectra by multiplying the PDOS calculated with LDA with their respective calculations. Reproduced from the middle panel of Fig. 3.4 b) from chapter 3. (Right) Full-multiplet configuration-interaction cluster calculations of the Co 3d photoemission spectra of LaCoO3 assuming the LS and HS initial states.

hybridization reduction will be mentioned and explained below, but it does not have a relevant effect on the shape of the core-level spectrum because of its relatively large lifetime broadening.

5.3 Valence band spectra

The left panel of Fig. 5.4 shows the evolution of the experimental valence band HAXPES spectrum of $LaCoO_3$ as a function of temperature. At 80 K our experimental valence band spectrum presents a sharp peak close to the Fermi energy at 0.75 eV. This peak mainly has Co t_{2g} character and is usually used in literature as fingerprint for the determination of the spin state of the cobalt ions. In fact, the LS state of a $3d^6$ configuration is a pseudo-closed t_{2g} sub-shell system and, as shown by the calculated spectra for a CoO_6 cluster in the right panel of Fig. 5.4, the spectral weight is concentrated in a single prominent peak, while for Co^{3+} ions in the HS state the spectral weight is distributed in a widely spread multiplet structure.

The presence of the sharp and intense peak close to the Fermi level not only at 80 K but also at 300 K is a clear indication that the Co^{3+} ions in

$LaCoO_3$ are still mainly in a LS state even well above the non-magnetic-to-paramagnetic phase transition shown by magnetic susceptibility at T 50 K. As the sample is warmed up the sharp peak exhibits a continuous reduction in spectral weight until becoming a little more than a shoulder at 650 K. The lost spectral weight is transferred to higher binding energies, suggesting the presence of a significant and growing number of Co^{3+} ions in the HS state as the temperature is increased above 300 K.

The valence band spectra between 2 and 10 eV is dominated by the contribution of the La 5*p* bands [28], as it was described in chapter 3, and can also be observed in the middle panel of 5.4, which explains the inability of the cluster calculations to reproduce the experimental spectrum in this energy region.

Our HAXPES results are very different from what was observed in previous UPS and XPS studies, where only small variations were noticed [87–90] as a function of temperature. It is likely that the previous photoemission studies were too much surface sensitive and the spin state of the cobalt ions on the surface is different from the bulk one, as also previously suggested [88]. The strong variations we observed in our spectral data is consistent with the previous XAS/XMCD study by Haverkort et al. and the Co 2*p* core level data as shown in Fig. 5.2 and Fig. 5.3.

5.4 Reproducing the gap

To get more insight on the evolution of the electronic properties of the present compound across the MIT we have displayed in Fig. 5.5 a close-up of the Fermi region of the valence band HAXPES spectrum (top left) and of the pre-edge region of the O-K edge XAS spectrum (top right). On the bottom panels, the corresponding photoemission and inverse photoemission spectra from the cluster calculations are included for comparison.

The HAXPES data show that at T = 80 K the energy distance between the valence band and E_F is very small, however a direct estimation of it from only the 80 K data is difficult because of the resolution broadening. As the temperature is increased, the appearance of a tail is observed on

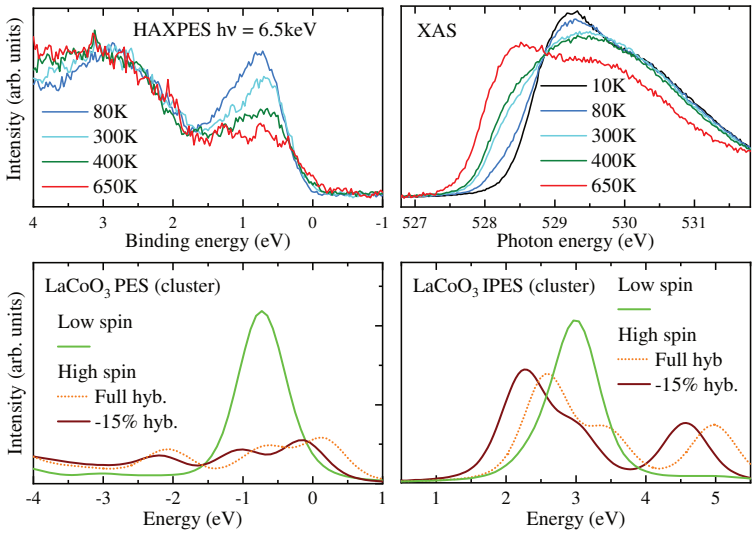

Figure 5.5: Top: Close-up of the valence band HAXPES (top left) and pre-edge region of O-K XAS (top right) spectra of $LaCoO_3$ measured at different temperatures. Bottom: Full-multiplet configuration-interaction cluster calculations of the Co 3*d* photoemission spectra (bottom left) and inverse photoemission spectra (bottom right) of $LaCoO_3$ using the values of $10Dq = 0.75$ (0.4) for the low (high) spin state. The high spin calculations were also performed including a reduced hybridization to account for the structural changes. We can observe that the energy position of the high spin features with respect to the low spin features observed in the experimental spectra can be much better reproduced when the reduction of the hybridization is included.

the low binding-energy side of the valence band already at 300 K. However the spectral intensity at the Fermi level remains very small even at high temperatures and without the onset of a clear Fermi edge, which indicates that at 650 K $LaCoO_3$ is still a bad metal.

Considering the shift in binding energy of the valence band close to E_F occurring between 80 K and 650 K we could estimate indirectly the energy distance between the Fermi level and the valence band at T = 80 K as 0.15 eV. Such a value is in a good agreement with the one (0.1-0.2 eV) measured in a previous high-resolution soft X-ray photoemission study of $LaCoO_3$ [91].

The O K-edge XAS spectrum displays strong shift towards lower values of photon energy as the temperature is increased from 80 K to 650 K (see right upper panel of Fig. 5.5). The pre-edge region of the XAS spectrum is related to transitions from the O 1s core level into O 2p states mixed with unoccupied Co 3d bands. At 80 K the pre-edge region is characterized by a main peak at 529.25 eV, related to transitions into unoccupied Co 3d e_g states, while at higher temperatures a second feature appears at 528.5 eV, that is associated to transitions into unoccupied Co 3d t_{2g} states [87]. Thus, the strong changes in the XAS spectrum occurring as a function of temperature reflect the spin-state transition: in fact at 80 K, the Co^{3+} ions are mainly in the LS state, where the t_{2g} levels are practically fully occupied and transitions mainly into the e_g levels are possible; on the contrary, at higher temperatures, the HS state predominates and unoccupied t_{2g} states are now available.

In our calculations, in the bottom panels of Fig. 5.5, we can observe that the shifts are not well reproduced when using the same hybridization values for LS and HS calculations, shown in the orange dotted curves. In the valence band calculations, there is a too large shift between the LS and HS spectra, and on the IPES, the shift is roughly half of the experimentally observed shift.

In order to get the energy position of the HS spectra right, we must use a different set of parameters for the HS calculations. In particular, we note that structural changes are reported at higher temperatures [92].

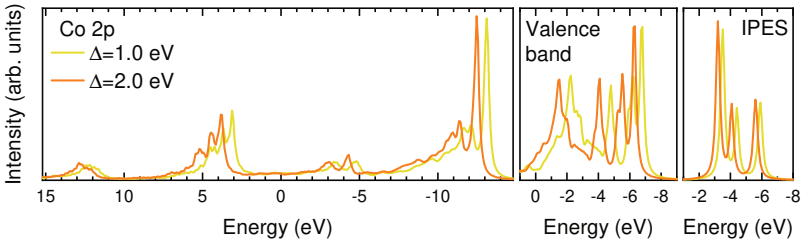

Figure 5.6: Cluster calculations of the HS Co 2*p* and valence band PES, and IPES spectra, without the hybridization reduction, for $\Delta = 2$ (in orange) and $\Delta = 1$ (in yellow).

At the high temperature phase, the interatomic Co-O distances increases from 1.943 Å to 1.978 Å. In terms of parameters, this increased distance could result into a reduced interaction or hybridization between the O and Co. The results we obtain when a 15% reduction is included in the HS calculations achieve a much better agreement of the energy position with the experiments, as seen in the brown curve in the bottom panels of Fig. 5.5. With these results, a bandgap of 3.5 eV is estimated for the LS state, and of 2.3 eV for the HS state, resulting in a gap reduction of around 1.2 eV from HS to LS, consistent with the experimentally reported results. Finally, here we point out that a quantitative comparison to determine the LS-HS ratios is not possible: In the valence band spectra, the fact that there is still La 5*p* contributions present in the 0 - 2 eV range does not allow make a direct sum of only the Co contributions that are calculated in the cluster model to reproduce the experimental data. As for the IPES spectra, while the positions of the features match with the XAS spectra, the intensities are different, due to the fact that in the O-K XAS, the intensities are also determined by the hybridization strength of the O 2*p* and Co 3*d*, which is orbital dependent.

One possible alternative approach for taking into account the structural changes is by changing the charge-transfer energy. LDA+U performed by Wu H. with a structure mixing LS and HS sites with their respective Co-O distances found that the calculations simulating this higher temperature LS-HS mixed scenario results in a relative change of energy of the Co orbitals,

which in our case could be translated into reducing Δ by 1 eV. In our cluster calculations, however, this parameter change yields results which are the in the opposite direction, as it can be seen in Fig. 5.6, indicating that this approach does not accurately reflect the system at its HS state.

5.5 Conclusions

Temperature dependent HAXPES and XAS spectra of $LaCoO_3$ were measured in the range of 80 K to 650 K. We have shown that the bulk sensitivity of HAXPES allows the observation of many significant changes on the Co 3*d* features due to the increased bulk sensitivity. We have performed cluster calculations and shown that the experimental data can reproduced by incoherently summing LS-HS spectra, with ratios agreeing with the values reported by Haverkort et al. [42]. Furthermore, we have found that in order to properly reproduce the HS spectra we need a different set of parameters, namely by reducing the hybridization strength as to take into account the structural changes. Our results suggest a scenario in which paramagnetic $LaCoO_3$ should be considered as an inhomogeneous mixed spin-state system.

Chapter 6

Kondoesque behaviour in CaCu3Ru4O12

The results presented in this chapter are published in:

Phys. Rev. X 12, 011017 (2022).

6.1 Introduction

In some strongly correlated systems, complex coherent quantum states cause a strong increase of the effective mass of the electrons, leading into what is known as heavy fermion behaviour. These coherent states can arise from the Kondo effect, where magnetic impurities couple with the spin of the conduction electrons. At temperatures lower than the Kondo temperature T_K, this coupling results into an entangled Kondo singlet state, manifested as a sharp resonance peak in the density of states. Heavy fermion materials can, in addition, show several unexpected phenomena such as unconventional superconductivity or quantum criticality [93–96]. While quite common in the rare-earth and actinide intermetallics, heavy fermion or Kondo behaviour is hardly encountered in transition metal oxides. One may find perhaps only in the oxide LiV_2O_4 [97–99] indications for heavy fermions physics.

The discovery of the transition metal oxide $CaCu_3Ru_4O_{12}$ (CCRO) showing properties of Kondo physics therefore created quite an excitement [101–103]. The crystal structure of this so-called A-site ordered perovskite is shown in Fig. 6.1. The magnetic susceptibility has a weak temperature dependence with a broad maximum at around 200 K, which resembles that of the heavy fermion system $CeSn_3$. The electronic contribution to the specific heat exhibits a relatively large Sommerfeld coefficient $\gamma = 70{-}140$ mJ/(f.u.mol K^2). The low-temperature resistivity

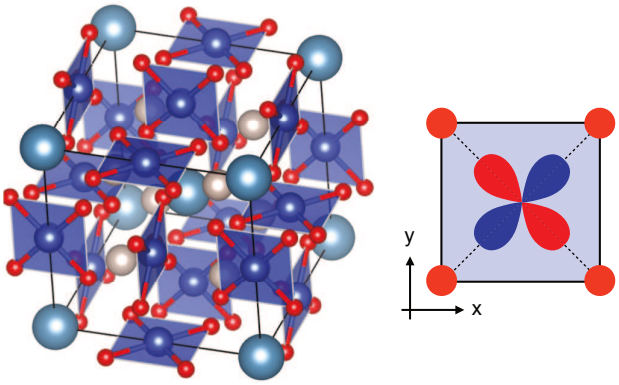

Figure 6.1: The crystal structure of $CaCu_3Ru_4O_{12}$ visualized by VESTA [100]. The blue, red, gray and indigo blue spheres represent Cu, O, Ru and Ca atoms, respectively. The sketch of the CuO_4 plane in the local axis system is also displayed.

is proportional to T^2 satisfying the Kadowaki-Woods relation with a value typical for $4f$ heavy-fermion materials. However, the Kondo interpretation of the CCRO properties has met reservations. It has been argued that the specific heat coefficient γ does not deviate much from the band structure value, suggesting a minor role of the electronic correlations [104]. Other interpretations of the mass enhancement have been put forward [105, 106].

Electron spectroscopy studies have not converged on the position or even the presence of the putative Kondo peak [110–112], but nonetheless confirmed the 2 + valence of the Cu ions [111]. The magnetic susceptibility of CCRO reported in the literature [102, 107, 108] as displayed in Fig. 6.2 is, however, clearly much smaller than the theoretical Curie-Weiss behaviour that would be expected from the presence of Cu^{2+} ions, unlike other compounds of the same family with Cu^{2+} such as $CaCu_3Ti_4O_{12}$ [109]. So far no magnetic ordering has been reported for $CaCu_3Ru_4O_{12}$, and thus, it is clear that there must be some mechanism that screens the magnetic moment of the Cu^{2+} ions.

In order to reconcile the existing controversies, we have carried out a detailed photoelectron spectroscopy study combined with local-density approximation (LDA) + dynamical mean-field theory (DMFT) calculations.

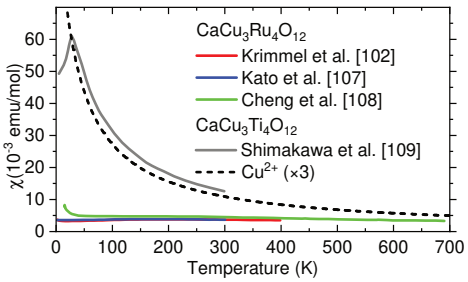

Figure 6.2: Magnetic susceptibility of $CaCu_3Ru_4O_{12}$ as reported in references [102, 107, 108] compared to the susceptibility of $CaCu_3Ti_4O_{12}$ from reference [109]. The black dashed line shows the theoretical Curie-Weiss paramagnetic behaviour from three Cu^{2+} S= 1/2 sites.

We have made use of a wide range of photon energies in order to disentangle the Ru, Cu, and O contributions to the valence band, starting from the hard x-ray range to ensure bulk sensitivity and using gradually lower photon energies to enhance the Cu 3*d* contributions. This gradual process allows us to observe a smooth change in the features consistent with the change in the cross-section ratios so that we can verify that no additional features of non-bulk nature appear in the spectra taken at the lower photon energies. Photon energies down to the Cooper minimum of the Ru 4*d* photo-ionization cross section are also used, where the Ru 4*d* signal is maximally suppressed. The LDA+DMFT calculations, performed by A. Hariki and J. Kuneš, were tuned to the experimental core level and valence band spectra and predict a Kondoesque scenario with a very high Kondo temperature of around $T_K \approx 500 - 1000K$.

The HAXPES measurements were carried out at the BL12XU beamline, as already described in chapter 2, with the photon energy of $h\nu = 6.5$ keV and the overall energy resolution of $\approx$ 270 meV. The soft x-ray (resonant) photoelectron (PES) and absorption (XAS) spectroscopy experiments were performed at the NSRRC-MPI TPS 45A Submicron Soft x-ray Spectroscopy beamline at the Taiwan Photon Source in Taiwan. The overall energy resolution when using 1.2 keV, 931 eV, and 440 eV photons was $\approx$ 150 meV, 125 meV, and 60 meV, respectively. Photoemission measurements in the

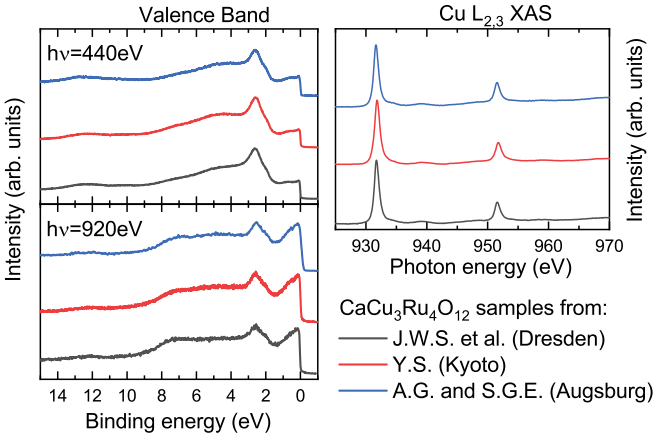

Figure 6.3: Valence band PES (left) and Cu-$L_{2,3}$ XAS (right) of $CaCu_3Ru_4O_{12}$ samples synthesized by the different groups used in this work.

vicinity of the Ru 4*d* Cooper minimum, i.e. at photon energies of 200 eV, 150 eV, and 100 eV, were performed at the PLS-II 4A1 micro-ARPES beamline of the Pohang Light Source in Korea. The overall energy resolution was ≈ 55 meV. Clean sample surfaces were obtained by cleaving sintered samples *in situ* in an ultra-high vacuum preparation chamber with a pressure in the low 10^{-10} mbar range. The measurements at SPring-8 and TPS were carried out at 80 K, and the measurements at PLS at 100K.

6.2 Consistency and valence

In systems such as CCRO where many controversies are present, it is very important to make sure that the results obtained are intrinsic to the material. Furthermore, as we will also later observe, some of our important claims are based on rather small spectral features.

In order to ensure the consistency and the sample quality, we have utilized three different batches of samples synthesized by three different groups: A.C. Komarek's group from Max Planck Institute for Chemical Physics of Solids, Dresden, A. Günther from the University of Augsburg, and Y. Shimakawa's group from the Kyoto University. Beyond the usual

characterization methods performed by the sample growers such as X-ray diffraction, we also performed PES and XAS measurements using the same conditions. Figure 6.3 shows the comparison of the valence band PES and XAS spectra taken from these three batches of samples. The results match perfectly, and thus confirm that the results presented here are not sample specific or due to extrinsic contributions.

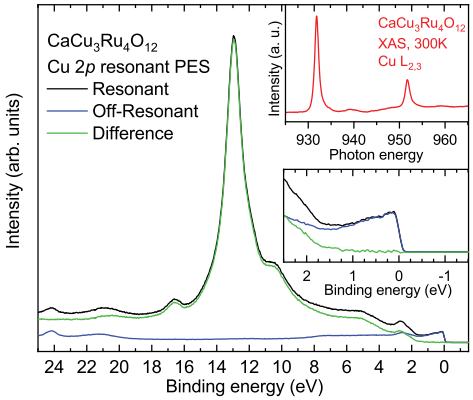

Figure 6.4: Valence band resonant photoemission of $CaCu_3Ru_4O_{12}$, with the experimental spectra taken at the Cu $2p$ (L_3) resonance ($h\nu = 931.2$ eV), at 10 eV below the resonance ($h\nu = 921.2$ eV), and their difference. The lower inset shows a close-up of the spectra in the vicinity of the Fermi level. The upper inset displays the experimental Cu-$L_{2,3}$ x-ray absorption spectrum.

Furthermore, XAS and resonant PES measurements can also be compared to previous results to verify the consistency with the literature. The XAS spectrum, shown in the left panel of Fig. 6.3 as well as in the top inset in Fig. 6.4 matches with the results reported in the literature, and confirms the 2+ valence of the copper in $CaCu_3Ru_4O_{12}$ [111]. The resonant PES results (Fig. 6.4) also agree with the literature [111]. Furthermore, the higher resolution of the present data (approx. 130 meV), allows to firmly conclude that there are no detectable Cu $3d^8$ states near E_F.

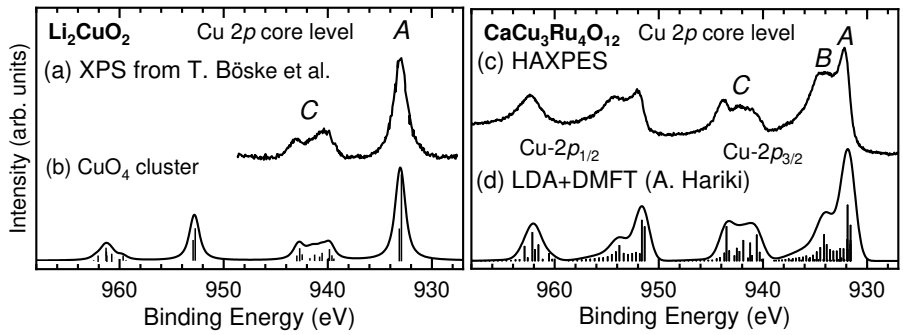

Figure 6.5: (a) Cu $2p$ core-level spectrum of Li_2CuO_2 reproduced from Ref. [113]. (b) CuO_4 cluster model results. (c) Experimental Cu $2p$ core-level spectrum of $CaCu_3Ru_4O_{12}$. (d) LDA+DMFT calculation provided by A. Hariki and J. Kuneš.

6.3 Core level spectra

Fig. 6.5 shows the Cu $2p$ core level HAXPES spectrum of CCRO together with that of Li_2CuO_2 reproduced from Ref. [113]. Here we took Li_2CuO_2 as a system which contains CuO_4 plaquettes that are weakly coupled electronically [113] and thus can serve for a comparison with CCRO that also contain rather isolated CuO_4 plaquettes. The two curves share the following gross features: the main peak (A) at around 932-933 eV binding energy and the satellite (C) at 942 eV for the Cu $2p_{3/2}$ component.

However, the fine structure differs: the main peak of CCRO consists of two peaks (A and B) [110, 114] unlike the single peak (A) of Li_2CuO_2.

The Li_2CuO_2 spectrum is typical for a Cu^{2+} oxide [115] and thanks to the weak coupling between the CuO_4 plaquettes it can be explained quite accurately with a single CuO_4-cluster calculation [85, 116], as shown in Figure 6.5 b). In contrast, the two-peak structure (A and B) of the CCRO main peak, cannot be captured by the CuO_4 cluster model. This is indicative of the presence of a screening process [110, 114, 117, 118] absent in Li_2CuO_2. The LDA+DMFT calculations, Fig. 6.5 d), reproduce the fine structure of the main peak well. We infer that CCRO contains magnetic Cu^{2+} ions, which experience screening by conduction electrons. How strong or complete the screening is, will be discussed later.

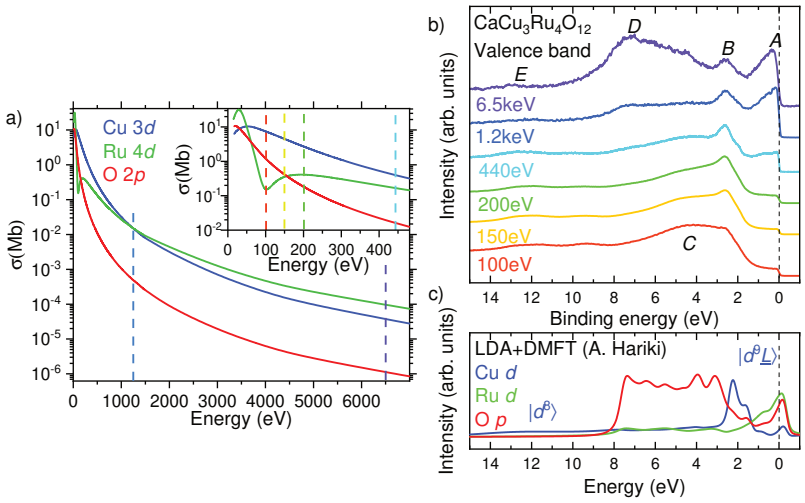

Figure 6.6: a) Photo-ionization cross section values of Cu 3*d*, Ru 4*d*, and O 2*p* interpolated from the data tabulated in Refs. [20, 21, 23]. The vertical lines indicate the photon energies used for the photoemission data. b) Experimental valence band spectra of $CaCu_3Ru_4O_{12}$ as measured using different the photon energies. c) LDA+DMFT results for the Cu 3*d*, Ru 4*d*, and O 2*p* spectral weight, calculated by A. Hariki and J. Kuneš.

6.4 Valence band and energy dependence

Fig. 6.6 b) shows the experimental valence band spectra of CCRO measured at various photon energies. Fig. 6.6 a) shows the photo-ionization cross section values for the Ru 4*d*, Cu 3*d*, and O 2*p* shells [20, 23], with the vertical lines specifying the photon energies used in the measurements.

The photon energy of 6.5 keV in HAXPES is much higher than the previously used photon energies of 1486.6 eV and 920 eV [110, 111, 114] and makes Ru 4*d* to have the highest cross section compared to Cu 3*d* and O 2*p*. The low photon energies of 200, 150 and 100 eV are close to the Cooper minimum of the Ru 4*d* cross section [20], so that with these photon energies the Ru 4*d* signal gets maximally suppressed, enabling us to observe better the Cu 3*d* contribution. The ratio between the O 2*p* and Cu 3*d* cross sections also becomes continuously larger with lowering the photon energy [20].

In the set of valence band spectra, Fig. 6.6 b), we can identify features which we label as A, B, C, D, and E. Features A and D are very strong at 6.5 keV and diminish practically completely at 200-150-100 eV photon energies. This strongly suggests that features A and D are derived from the Ru 4*d*. Features B and E are visible throughout the set, while feature C enhances its intensity for 100 eV, the lowest photon energy of the set. This observation indicates that features B and E are related to the Cu 3*d* while feature C is likely to be of O 2*p* origin. We point out that the positions of these five features do not change with the photon energy, and coincide with the previously reported soft x-ray studies [110, 111, 114].

The results of the LDA+DMFT calculations by A. Hariki and J. Kuneš are presented in Figure 6.6 c), and confirm that the assignments based on the photon energy dependence of the experimental spectra are well reproduced. The calculated Ru 4*d* spectrum matches the experimental features A and D, while the theoretical Cu 3*d* spectrum explains well the features B and E, the former being the Cu $|d^9\underline{L}\rangle$ and the latter the Cu $|d^8\rangle$ final state [111, 119, 120]. $\underline{L}$ denotes here a hole in the oxygen ligand. The feature C is captured by the theoretical O 2*p* spectra. The calculations reveal that the spectrum around the Fermi level consists of hybridized Ru 4*d* and O 2*p* bands. In performing the LDA+DMFT calculations, A. Hariki and J. Kuneš tuned the double-counting corrections such that the experimentally observed energy position of peaks A, B, C, and D of the valence band (Fig. 6.6 b) are best reproduced, as well as the position of the peaks A, B, and C in the Cu 2*p* core level (Fig. 6.5 d)

These observations lead to the picture of CCRO as a system consisting of Cu^{2+} ions immersed in a hybridized Ru-O band. The calculations also reveal a peak just above the Fermi level, associated with a small but discernible Cu 3*d* character. Is this the sought-after Kondo resonance, similar to the case of intermetallic Ce and Yb 4*f* systems?

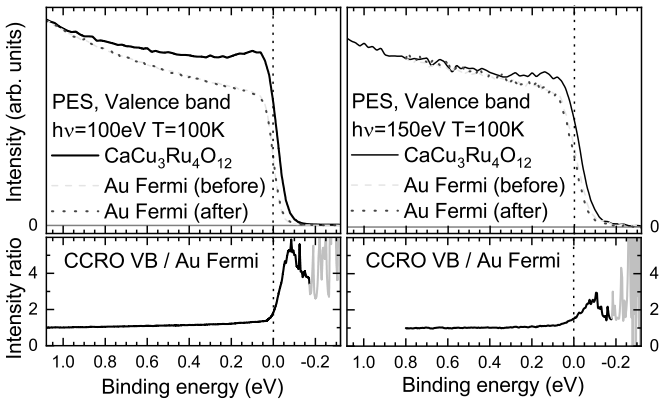

Figure 6.7: (top panels) Close-up of the Fermi level region of the $CaCu_3Ru_4O_{12}$ spectrum together with the gold spectrum measured before and after. (bottom panels) Division of the $CaCu_3Ru_4O_{12}$ spectra by the gold spectra. Left panels show the results taken using 100 eV photons and right panels using 150 eV.

6.5 The resonance peak

To answer this question experimentally, we focus on the spectra taken at the photon energies which minimize the Ru 4*d* signal, i.e. with 100 and 150 eV. The top panels of Fig. 6.7 display a close-up of the spectra along with the corresponding gold reference spectra taken under the same conditions. In order to look for the possible presence of states above the Fermi level, we divide the CCRO spectrum by the corresponding gold spectrum. The results are shown in the bottom panels of Fig. 6.7. For both the 100 eV and 150 eV spectra, we can identify clearly the presence of a sharp peak at about 0.07-0.08 eV above the Fermi level, very consistent with the results of the LDA+DMFT calculations.

In order to ensure that this experimental finding is not an artifact caused by an energy shift, we have taken the gold spectra shown in Figure 6.7 just before and just after each CCRO measurement. It can be seen that the 'before' and 'after' gold spectra overlap perfectly, demonstrating that there is no energy shift in the experiment and that the observation of the peak at 0.07-0.08 eV above the Fermi level is reliable. We remark that Sudayama *et*

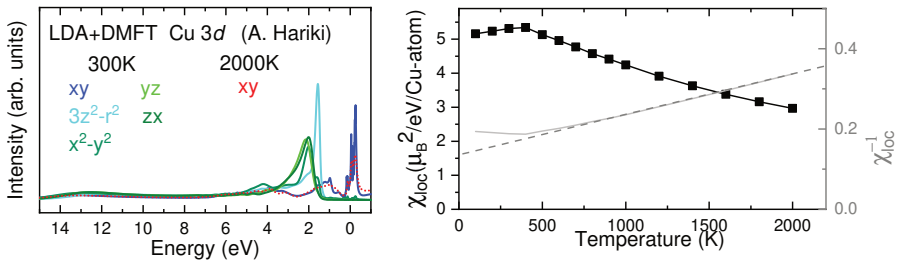

Figure 6.8: Left: The LDA+DMFT spectral weights of the Cu 3*d* in $CaCu_3Ru_4O_{12}$. The Cu orbitals are defined in the local axis of CuO_4 plane, see Fig. 6.1. Right: Local susceptibility $\chi_{\rm loc}$ and its inverse as calculated by LDA+DMFT. Both results were provided by A. Hariki and J. Kuneš.

al. [110] have observed a feature at about 5 meV above the Fermi level in their ultra-low-photon energy photoemission experiments. We notice that the sensitivity for the Cu 3*d* with respect to the O 2*p* and Ru 4*d* is one to two orders of magnitude larger when using 100-150 eV photons as is done in here in comparison with the ultra-low-energy photons utilized in their study. Indeed, their spectral feature is close to the Ru 4*d* component calculated by LDA+DMFT (Fig. 3) rather than the Cu 3d one.

6.6 Discussions

Having established experimentally the theoretically predicted existence of a sharp Cu-derived peak just above the Fermi level, A. Hariki and J. Kuneš now investigate theoretically its orbital character and behavior with temperature. The left panel of Fig. 6.8 shows the orbitally resolved Cu 3*d* spectral weights. The calculations reveal that the peak just above the Fermi level stems overwhelmingly from the xy orbital, i.e. the Cu 3*d* orbital which is σ-bonded with the oxygens, see Fig. 6.1. This is consistent with the notion that the hole in a square-planar coordinated Cu^{2+} ion resides in the σ-bonded orbital [121, 122]. Also similar to the 4*f* Kondo and heavy fermion systems, the peak intensity decreases with increasing temperature. However, we can also observe that the Kondo-like peak as calculated by the DMFT calculations displays a set of complex features, instead of being a simple

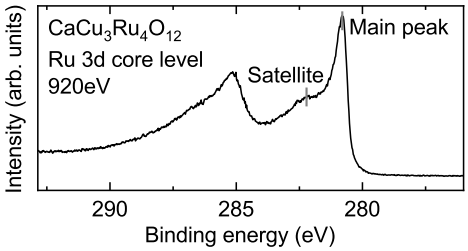

Figure 6.9: Experimental Ru $3d$ core-level spectrum of $CaCu_3Ru_4O_{12}$. The presence of the satellite feature indicates that correlations are present on the Ru site.

single sharp peak. This complex behaviour result from the asymmetry of the conductive bands due to the correlations on the Ruthenium site. The presence of such correlation effects can be experimentally confirmed by the presence of satellite features in the Ru $3d$ core level, as shown in Fig. 6.9, and is in fact one of the main differences that distinguish the DMFT results presented here and the ones by Liu et al. [112]. The exact way in which such changes affect the Kondo behaviour and its resonance peak, however, remain to be studied.

The above results can be now related to the behaviour of the local spin susceptibility χ_{loc} at the Cu site. The right panel in Fig. 6.8 displays the χ_{loc} as calculated using the LDA+DMFT approach. χ_{loc} exhibits the Curie behavior at high temperatures, and turns into a broad maximum at lower temperatures which is characteristic for Kondo screening. The deviation from the Curie behaviour starts around 700 K, as can be seen also from the χ_{loc}^{-1} curve in the right panel of Fig. 6.8, suggesting a relatively high Kondo scale T_K. The calculated χ_{loc} reproduces quite well the characteristics of the experimental susceptibility [101] although an exact matching can't in general be expected between the local and the uniform spin susceptibility [123], and in this particular case also not due to the contribution from the itinerant Ru $4d$ - O $2p$ states.

The presence of magnetic Cu ions immersed in an itinerant band leads indeed to the emergence of Kondo physics, as demonstrated by our

spectroscopy and corresponding LDA+DMFT results from A. Hariki and J. Kuneš. An important aspect for the longstanding discussions about CCRO is also the finding that the Kondo temperature is quite high, i.e. around 700 K (between 500 and 1000 K). This implies that the contribution of the Kondo screening process to the low temperature specific heat is modest, thus explaining why band structure calculations can seemingly reproduce the experimentally observed γ value of the specific heat rather well since the main contribution comes from the Ru-O derived bands. The high Kondo temperature also implies that upon going from high to low temperatures the Kondo screening process is practically completed already at 300 K, and that lowering the temperature further would not produce significant changes in the electronic and magnetic properties. So it is understandable now that there is a controversy about the existence of Kondo physics in $CaCu_3Ru_4O_{12}$ since the signatures for its presence are small and residing on a high background when performing low temperature measurements.

6.7 Conclusions

We presented hard X-ray Valance and Cu $2p$ photoemission spectra in $CaCu_3Ru_4O_{12}$. The experimental spectra are analyzed using the local-density approximation (LDA) + dynamical mean-field theory (DMFT). The double peak main line in Cu $2p_{3/2}$ core level spectra is identified as a fingerprint of the strong coupling of localized Cu $3d$ moment and Ru $4d$ bands, being the source of the charge-transfer-Kondo behaviour in $CaCu_3Ru_4O_{12}$. The valence spectra at different photon energies allow a detailed disentanglement of spectral features, and show the charge-transfer-type Cu $3d$-O $2p$ bands, embedded in metallic Ru $4d$ bands. The experimental findings are supported by the LDA+DMFT calculations and the analysis of the spin and charge susceptibility confirms the Kondo behaviour of Cu $3d$ states with a high temperature scale in $CaCu_3Ru_4O_{12}$. The Kondo resonance peak predicted in the LDA+DMFT calculations was experimentally found by measuring the photoemission spectra using the photon energy corresponding to the Cooper minima of Ru $4d$. According to LDA+DMFT calculations the presence of a

U on the ruthenium site, justified by the satellites in the Ru $3d$ core level spectrum, is relevant for setting the Kondo temperature in the 500 - 1000 K range in the calculations in $CaCu_3Ru_4O_{12}$.

Chapter 7

Orbital Imaging with HAXPES

Part of the results presented in this chapter are published in:

Phys. Rev. Research 4, 033108 (2022).

7.1 Introduction

In unravelling the electronic structure of strongly correlated systems based on transition metal (TM) d or rare-earth (RE) / actinide f elements, there is a strong need to identify the active d or f orbitals in the system. Very recently, a new experimental method has been developed with which one can obtain a direct image of the orbital hole density. This method is based on non-resonant inelastic scattering with high momentum transfer involving an s-orbital [124–126], and is called s-NIXS. Since with this method holes are probed, it is most suitable for late TM or RE systems where a large contrast in the image can be obtained since the number of holes is small in the d or f shell. In order to cover early TM or RE or uranium compounds, where the number of holes is large but the number of electrons is small, it would be highly desirable to have an analogous imaging method which would then be based on photoemission processes to achieve a high contrast image.

According to an atomic theoretical result derived by Goldberg, Fadley and Kono in 1978 [127, 128] for a free standing single ion, in the specific experimental geometry where the polarization of the light and the momentum of the measured electrons is parallel, the matrix elements cause the photoemission intensity to be directly proportional to the electron density of initial state parallel to the polarization. Then, by rotating the

single atom in such geometry, it should be possible to reproduce or image the orbital shape from the intensity of its spectral features. Until now, however, there are only reports experimentally using such initial-state dependence in studies of molecular orbitals of adsorbates [129]. To our knowledge, such experiments have not been performed or reported on solid state bulk materials. Compared to the NIXS technique in which photons are measured, the electron based photoemission experiments present additional complications for performing such experiments in bulk samples due to the interactions the electrons can have with the material before reaching the analyzer. The momentum of the outgoing electrons can be affected by inelastic as well as elastic scattering effects. Incoherent scattering effects will cause a loss of the information about the momentum, leading into a homogeneous spread of the electrons, while coherent processes can lead into the formation of complex patterns from the diffraction of the outgoing electrons with the upper layers of the material in a process also known as (X-ray) photoelectron diffraction (XPD)[130, 131]. Furthermore, we must also consider the dispersions of valence electrons which can also determine the moment of the outgoing electrons.

In this context it is understandable that the actual observation of such theoretically predicted initial state dependence has still not been reported for bulk samples, with all these additional phenomena affecting also the momentum of the photoelectrons. However, in this chapter, we will show that by using HAXPES many of such effects can be normalized by using a shallow core level and it becomes in fact possible to perform orbital imaging measurements analogous to the NIXS technique but with electrons.

7.2 Experimental geometry

Experiments have been carried out at the Max-Planck-NSRRC end station at the Taiwan undulator beamline BL12XU at SPring-8, Japan. The photon beam was linearly polarized with the electrical field vector in the plane of the storage ring (i.e., horizontal) and the photon energy was set at about 6.7 keV. The overall energy resolution was set at 0.27 eV. The measurements

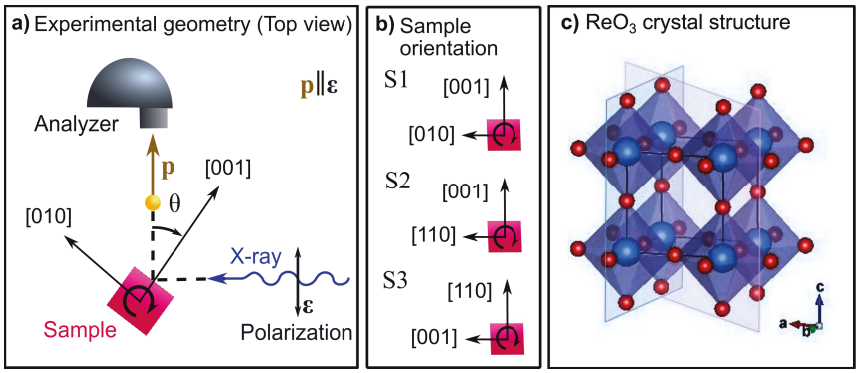

Figure 7.1: a) Top view of the experimental geometry of the HAXPES experiment. The photoelectrons detected by the analyzer have their momentum **p** parallel to the electrical field ε of the photon beam. θ is the polar angle. Experiments are performed from values of $\theta \approx 0$ to $\theta = 45°$. b) The orientation of the three measured samples, as defined by the orientation of the crystal at $\theta = 0$ and the orientation perpendicular to it in the plane of rotation. c) Crystal structure of ReO_3. The blue spheres represent the rhenium atoms and the red spheres represent the oxygen atoms. The blue (pink) plane corresponds to the rotation plane of the S1 sample (S2 and S3 samples).

were performed at 80 K. The analyzer is mounted parallel to the photon beam's electrical field ε as shown in Fig. 7.1 a). The momentum of the measured photoelectrons **p** is therefore also parallel to ε.

The rotation of the sample on the plane formed by **p** and the direction of the incoming photons is defined by the polar angle θ. The origin $\theta = 0°$ is set at the grazing incidence geometry, and the rotation direction is such that $\theta = 90°$ at the normal incidence geometry. In our experiments, measurements are performed on a freshly cleaved sample surface and for values of θ between $0°$ and $45°$, as for higher angles the intensity of the photoelectrons becomes lower, leading into data with lower quality.

In this experiment, ReO_3 is used as a model compound to show the capabilities of the technique. ReO_3 has a cubic structure, with the rhenium atoms surrounded by an oxygen octahedra (Fig. 7.1 c)) leading the Re $5d$ to split into e_g and t_{2g} levels. The electronic structure of ReO_3 can be accurately described by band structure calculations [132], and furthermore, the cross-sections of Re $5d$ at 6.7 keV are much higher than the other valence

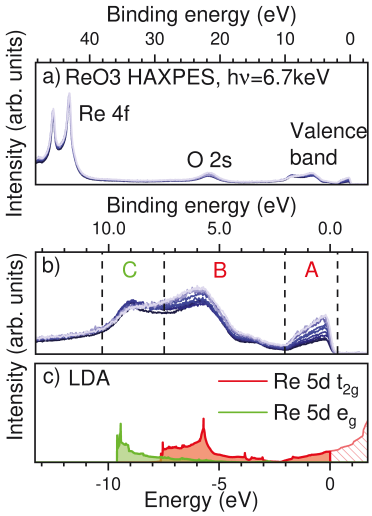

Figure 7.2: a) Experimental HAXPES spectra in its full measured range. The spectra measured on different orientations and samples are all normalized to the same Re $4f$ core level integrated intensity. The spectra displayed in this figure correspond to the measurements performed for sample S1. b) Close-up of the valence band region. The valence band is divided into three regions dominated by the features A, B and C respectively. c) Partial density of states of the Re $5d$ t_{2g} and e_g. The A and B features can be attributed to t_{2g} contributions, and C mostly to e_g contributions.

orbitals [23], making ReO_3 an optimal candidate for studying its d orbitals without other undesired contributions affecting the results.

ReO_3 single crystal samples with three different orientations are used (Fig. 7.1 b)). For the sample S1, the crystal orientation at $\theta = 0°$ is [001], and at $\theta = 90°$ it is [010], defining the rotation plane corresponding to the blue cut in Fig. 7.1 c). In sample S2 (S3) the crystal orientation at $\theta = 0°$ is [001] ([110]) and at $\theta = 90°$ it is [110] ([001]), so that by using both samples the full 90 degree range between [001] and [110] can be measured. The rotation plane of these two samples corresponds to the pink cut in Fig. 7.1 c).

7.3 Results

In this experiment, it is of high importance to have a common reference in all measurements that can be used for normalizing the data. As discussed in the introduction, XPD effects are known to affect the angular distribution of the photoemitted electrons, and other extrinsic details such as the incidence angle or variations due to irregularities in the specific measured spot can lead to changes in the intensity but are difficult to quantify.

In this context, the Re $4f$ core-level, at around 45 eV binding energy, is an ideal candidate for the normalization. On one side, the photoelectrons from the shallow Re $4f$ core-level have almost the same kinetic energy as the valence electrons, and thus, the observed XPD effects are expected to be almost the same as those of the valence band [19, 133, 134]. Furthermore, fully filled cores are expected to have a spherical symmetry and thus, it should not display any initial-state orientation dependence. Therefore, by normalizing the spectra to the integrated Re $4f$ core-level intensity we can expect to normalize all effects except for those that depend on the initial-state orientation dependence of the partially filled valence band orbitals. The sharp shape of the $4f$ peaks allows an accurate normalization, as well as serving as an indication of the good quality and cleanliness of the measured spot.

Fig. 7.2 a) shows the measured spectra in its full range. The Re $4f$ core level is included in all valence band measurements to ensure that the normalization of the valence band spectra is reliable and accurate. Figure 7.2 b) shows a close-up of the valence region, which displays three main features A, B and C. The spectra is divided into three regions around each of the features. This division will later be used as integration ranges. In order to determine the character of each feature, ab-initio calculations were performed with the code FPLO [78]. The calculated partial density of states, as shown in Fig. 7.2 c), indicate that features A and B can be attributed mainly to t_{2g} orbitals, while feature C originates from the e_g orbitals.

Fig. 7.3 shows the valence band spectra of all three samples measured at different values of θ, after a standard integral type ("Shirley") background

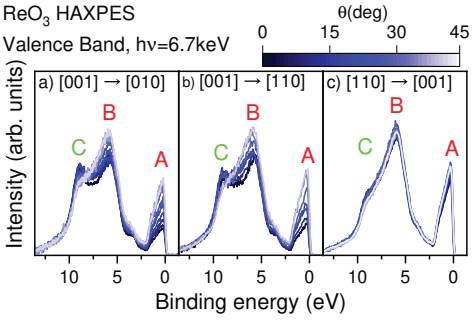

Figure 7.3: Valence band spectra of the three samples measured at different values of θ, after a Shirley background subtraction and a common normalization to the Re $4f$ core level intensity. Significant orientation dependence can be observed in all three main features or regions for S1 and S2.

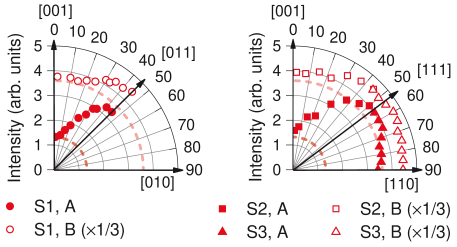

Figure 7.4: Polar plot of the intensity of the t_{2g}-dominating regions of the valence band spectrum measured for the different orientations. The integrated regions A and B are as shown in Fig. 7.2, with Region A (Region B) ranging from -0.7 eV to 2.05 eV (2.05 eV to 7.05 eV) in binding energy. The dashed lines show the amount of isotropic background present.

[4] subtraction and a normalization to the Re $4f$ integrated intensity. We can observe that very clear variations on the intensity of the features can be observed, especially for the orientations corresponding to the samples S1 and S2. In particular, the intensity of feature A changes up to a factor 3 depending on the orientation, while features B and C display more modest but still significant changes. In order to quantitatively compare the intensities first of the t_{2g}-like features A and B, we integrate the intensities in the ranges as shown in 7.2 b), that is, from -0.7 eV to 2.05 eV (2.05 eV to 7.05 eV) in binding energy for A (B).

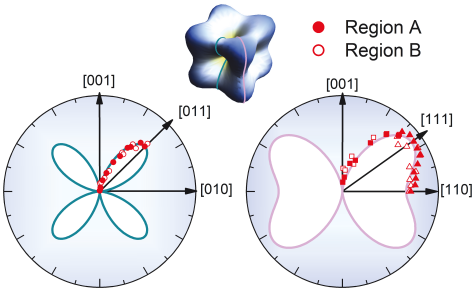

Figure 7.5: Integrated intensities of regions A and B after subtracting a constant background as shown in the dashed lines in Fig. 7.4, overlapped to the projection of the t_{2g} theoretical orbital function as calculated from the corresponding spherical harmonics.

The results of the integration are represented in polar plots in Fig. 7.4. As we observed in Fig. 7.3, the intensity variations in region A are significantly larger than in region B, but in both cases, it is possible to clearly appreciate the change. It is important to note that the intensity values obtained from different samples at common orientations ([001] for S1 and S2, [110] for S1 and S3, and the 45° in the S2-S3 cut) are consistent with each other. Furthermore, we can observe the minimum at [001], a maximum in [110] on the cut defined by the geometry in S1, and the global maximum in the [111] direction. The positions of said maximums and minimums correspond to those of the theoretical t_{2g} orbitals, demonstrating that the dominating t_{2g} character in the integrated regions can be directly deduced. However, we can also observe that the shape does not fully correspond to the theoretical orbital shape, and in particular, we have a non-zero intensity in the minimums.

If we then assume that some isotropic contributions or background is present in our data, we can subtract such a constant background as shown in the dashed lines in Fig. 7.4. The choice of the intensity of such isotropic background corresponds to the intensity we observe at the minimum [001], where theoretically we would expect zero intensity. The result, as shown in Fig. 7.5 perfectly match with the corresponding projections of the theoretical

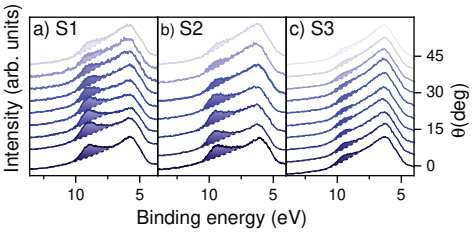

Figure 7.6: Close-up of the e_g-like feature C. In order to calculate the area corresponding to C, as coloured in the figure, a baseline (dashed line) was interpolated from the surrounding data for each case.

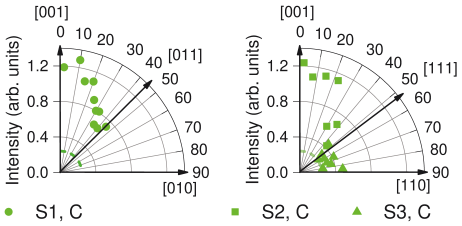

Figure 7.7: Polar plot of the intensity of the e_g-like feature C of the valence band spectrum measured for the different orientations. The integral has been performed in the area between 7.05 eV to 11.05 eV in binding energy after subtracting a baseline as depicted in 7.6. The dashed lines show the amount of isotropic background present.

t_{2g} orbital function as calculated from the spherical orbitals. We will discuss later about the nature of such isotropic background contribution.

7.4 Non-isolated contributions

In contrast to the t_{2g}-like features, the e_g-like feature C, is not completely isolated nor has a very clear dominance. In Fig. 7.3 we can observe that in the experimental spectra, the peak C is sitting on top of a baseline dominated by the t_{2g} influence. To be more precise, at around 7.05 eV binding energy, where the e_g-like feature C starts, the starting intensity follows exactly the same t_{2g}-like trend that can be observed in regions A and B. Therefore, the direct integration would provide mixed information from the overlapping contributions.

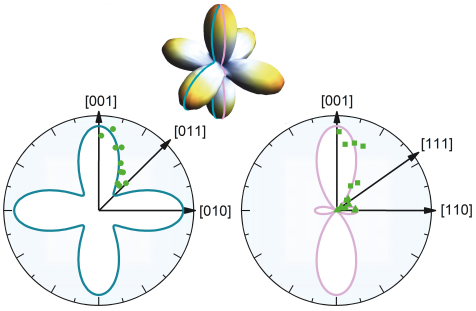

Figure 7.8: Integrated intensities of feature C after subtracting a constant background as shown in the dashed lines in Fig. 7.7, overlapped to the projection of the e_g theoretical orbital function as calculated from the corresponding spherical harmonics.

In order to isolate the contribution of the e_g-like feature C, a baseline subtraction is performed, as shown in Fig. 7.6. The baseline is defined by an interpolation using the data points close to peak B, at around 6 eV, where the t_{2g} character is clearly dominant, and points after feature C, at around 10 eV, where there is no orientation dependence appreciated anymore. A cubic spline interpolation was performed to ensure a smooth curve, and the results can be seen in the dashed lines in Fig. 7.6. The integrated area then corresponds to the coloured regions in Fig. 7.6, and its polar representation are displayed in Fig. 7.7. Here also a significant variation can be observed, and also the overall e_g-like trend is appreciated. By performing a constant background subtraction with a background intensity corresponding to the intensity observed at the [111] direction where a theoretical zero intensity is expected, we obtain the results shown in Fig. 7.8. Here we again observe a very good agreement of the experimental data with the corresponding projections of the theoretical e_g orbital function, showing thus that this technique can also provide the orbital character information from spectral features that are not fully isolated or dominant.

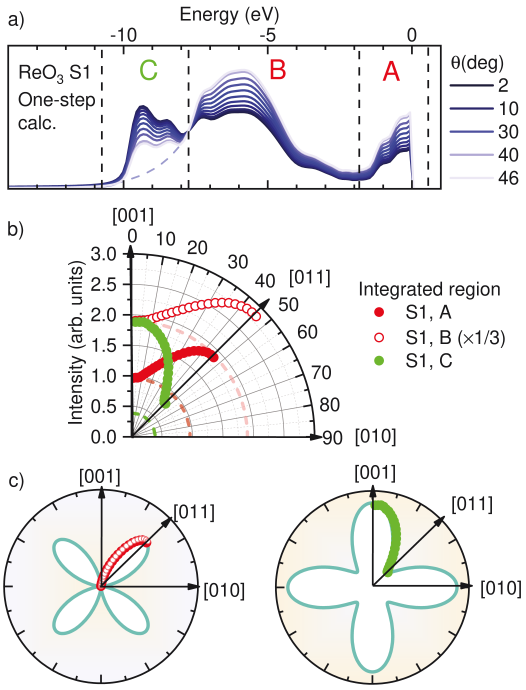

Figure 7.9: a) Calculated valence band spectra by using the one-step model in the experimental geometries corresponding to S1, after normalization to the total integrated intensity. b) Integrated intensity values of the regions A and B and of the feature C, defined in the same ranges and using the same procedures as with the experimental spectra. c) Integrated intensities after the background subtraction, overlapped to the projection of the corresponding theoretical orbital functions as calculated from the spherical harmonics.

7.5 One-step model calculations

In order to better understand the nature of the experimentally observed isotropic contributions, one-step model calculations were performed by L. Nicolaï and J. Minár using the same geometries as the experiments.

Fig. 7.9 a) shows the calculated valence band spectra in the same geometry as the experiments performed in sample S1. We observe that the orientation-dependence trends match very well those observed in the experiment, as displayed in Fig. 7.3. By performing the same integration procedure as in the experiment Fig. 7.9 b), we obtain an angular profile very

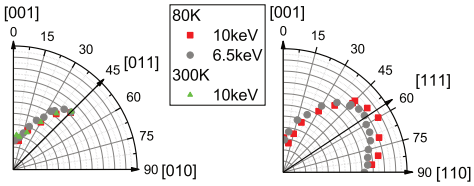

Figure 7.10: Polar plot of the integrated intensity region A by using hν = 10 keV and temperatures of 80 K and 300 K, together with the 6.5 keV previously displayed in fig. 7.4

similar to the experimental ones as shown in figures 7.4 and 7.7. We can observe that in the calculations, a similar amount of isotropic background is obtained, indicating that the effects causing such contributions is already included within the one-step model calculations. After the subtraction of a constant background in the calculations, we can very well reproduce the projections of the e_g and t_{2g} orbital functions (Fig. 7.9 c)). Here we have to note that so far only the calculations for the cut corresponding to S1 are available, and thus, the background intensity selection procedure for the e_g data was not, as in the experiment, of choosing the intensity at the [111] direction. Instead, the background was chosen so that the ratio of the intensity at [011] to the intensity at [001] after subtraction is 0.25, as expected from the theoretical curve. Further calculations are being performed by L. Nicolaï and J. Minár to obtain the remaining geometries and to verify that the same criteria as in the experiment can be followed.

7.6 Photon energy and temperature dependence

We have performed additional measurements using a different photon energy of hν = 10 keV, with temperatures of 80 K and 300 K. The results are shown in Fig. 7.10. We observe that by using the same temperature of 80 K but higher photon energy, the orientation dependence becomes sharper, that is, the amount of isotropic contribution decreases in proportion to the anisotripic signal. This is consistent with the idea of the increased forward focusing and less side-scattering effects at higher energies.

As for the temperature dependence, the data shown in the left plot of Fig. 7.10 indicates that the differences are rather small between 80 K and 300 K, with only a slight increase in the isotropic contribution.

7.7 Discussions

In the HAXPES experiments performed with ReO_3, we have been able to observe the t_{2g} and e_g like trends by integrating the different regions/features, and that the angular profiles that we obtain with such integration, very well correspond to the shapes obtained from the spherical harmonics with an added constant background. The one-step model calculation results match very well to the experimental results, indicating that all effects observed in the experimental spectra and trends are already included within the theoretical model. The fact that we did not observe any additional coherent trends such as the ones that would be expected from XPD effects [19, 133, 134] means that the shallow Re $4f$ core level can indeed be used for the normalization. In particular, a normalization procedure using the O $2s$ was attempted, leading to a very different angular profile. This is most likely due to the different XPD profile that comes from the electrons diffracted in the oxygen sites, as the different sites can lead into different diffraction conditions. From this, we can conclude that the normalization must be performed using a core level from the same site as the orbitals that are studied. The changes observed by increasing the photon energy were not very large, but still significant enough to support the idea that the isotropic background comes from incoherent scattering effects that are reduced by using higher energies, where the forward focusing is more pronounced. The fact that from 80K to 300K the trends do not change, tells us that in both cases we are well into the XPS limit, and thus, ARPES effects are no longer relevant. However, with increased temperature, an increase of incoherent scattering effects may have been expected, but it is possible that the change in temperature was not significant enough for the Debye scale. Our explanation of the incoherent scattering is also consistent with the

results explained in chapter 3, where we showed that side scattering (i.e. incoherent elastic scattering) is still quite relevant in HAXPES.

7.8 Further examples

In this section we will show further examples of orientation dependence measurements, to illustrate that even in cases with conditions which are not so ideal as in ReO_3, this technique can provide relevant information.

7.8.1 Sr_2IrO_4

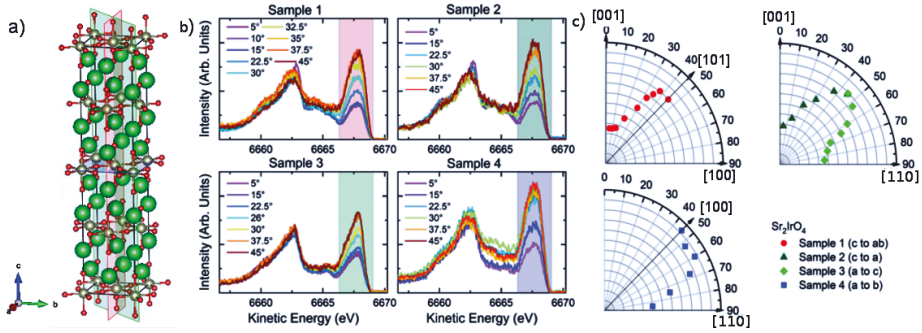

Figure 7.11: a) Crystal structure of Sr_2IrO_4. The green spheres represent the strontium atoms, the grey spheres the iridium atoms and the red spheres the oxygen atoms. The three planes corresponds to the cuts studied with the orientation dependant technique. b) Experimental valence band spectra after normalization. The highlighted area with coloured boxes is the integration region. c) Polar plot showing the orientation dependence of the integrated regions.

In Sr_2IrO_4, with the crystal structure shown in Fig. 7.11 a), the iridium atoms in distorted oxygen octahedra. The IrO_6 octahedra are distributed in planes, and so a certain anisotropy in the shape of the Ir $5d$ orbitals can be expected. Furthermore, in Sr_2IrO_4, we expect a more covalent scenario similar to the double pervoskite iridates presented in chapter 4.

Fig. 7.11 b) shows the experimental valence band spectra after normalizing to the Ir $4f$ core level. Similar to the case with the double perovskites,

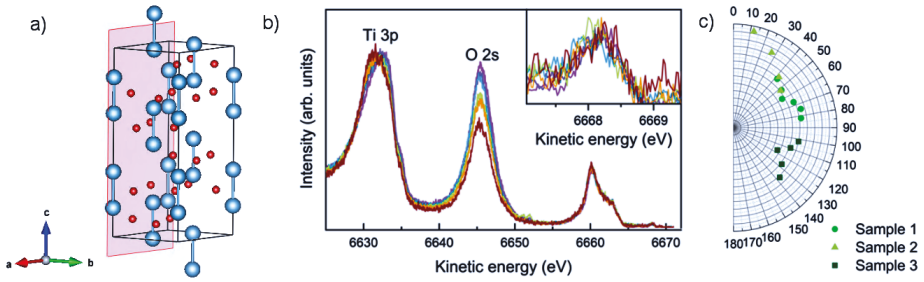

Figure 7.12: a) Crystal structure of Ti_2O_3. The blue spheres represent the titanium atoms and the red spheres represent the oxygen atoms. The pink plane corresponds to the rotation plane studied. b) Experimental valence band spectra of sample 1 after normalization to the Ti 3*p* core level integrated intensity. The inset shows a close-up of the integrated region. c) Polar plot showing the orientation dependence of the integrated regions.

here we can expect the Ir 5*d* contributions to be dominant in the valence band spectra.

Several samples with different orientations were used to cover the three planes drawn in Fig. 7.11 a). In the spectra, we can observe that a clear orientation dependence is observed for the first peak near the Fermi energy. By integrating the highlighted region, we obtain the results shown in Fig. 7.11 c). We can observe a clear t_{2g}-like trend, with the intensity being minimum at the directions corresponding to Ir-O. Note that in the a-b plane, the Ir-O bonds are not on the directions of the axis but rather at $45 \pm 12°$, resulting into a minimum in the [110]. In particular, we can observe the additional local maximum at 57°, which matches with this 12 degree buckling.

While further analysis and interpretation could provide interesting information about the sample, we have shown that the orientation dependence measurements can also be performed in other materials with more complicated electronic and crystal structures.

7.8.2 Ti_2O_3

The next example is Ti_2O_3, with a structure shown in Fig. 7.12 a), and it is a compound in which Ti-Ti dimers with the configuration $a_{1g}a_{1g}$ are formed

along the *c*-axis[135]. In this case, with a 3*d* transition metal, the conditions are not so favourable as the cross-section of the Ti 3*d* orbital of our interest is very small and comparable to other valence band contributions such as O 2*p*. Fig. 7.12 b) displays the experimental spectra corresponding to one of the measured samples. The normalization has been done using the Ti 3*p* core level. Here, we observe that the O 2*s* semi-core intensity is not normalized in the same manner as the Ti 3*p*, which as we have previously discussed for ReO_3, can be attributed to the differences in the XPD patterns generated for the oxygen sites and are thus not normalized,

Now, if we focus on the tiny Ti 3*d* feature near the Fermi energy [135], shown also in the inset of Fig. 7.12 b), we observe that it is very difficult to discern any trend. Each one of the displayed spectra is the result of in average 8 hours of measurements, but because of the small cross-sections and the already small feature to begin with, obtaining a good intensity to noise ratio within a reasonable time would be very hard to accomplish. By integrating, however, some trend can still be observed, as seen in Fig. 7.12 c). Here we observe a highly anisotropic shape with larger intensity in the direction of the c axis, and local minimum at around 55° as expected from the a_{1g} orbitals. Nonetheless, its significant noise makes the correct background subtraction difficult and would actually lead to very large error bars.

7.9 Conclusions

In this chapter we have shown evidence that by measuring single crystal samples with HAXPES in the specific geometry where the photoelectrons are measured in the same direction as the polarization of the light, the intensity of the spectral features in the valence band present a clear orientation dependence. By normalizing the spectra taken in different orientations to a core level from the same element and integrating then the spectral features of the valence band, it is possible to directly observe the trends corresponding to the shapes of the expected initial state orbitals, even from features that are not completely isolated in the valence band. The observed orientation

dependence displays a certain isotropic background which appears to be caused by scattering processes, and thus, influenced by the photon energy and the temperature at which measurements are performed. By subtracting a constant background, it is possible to recover no only the trend but also the exact theoretical shape of the orbital. Finally, we have shown other examples beyond the ReO_3 which was chosen as a model compound, and we have seen than the orientation dependence can be observed in more complicated structures, or even from orbitals with small cross-sections, as the integration process reduces the influence of the noise present in the spectra.

From the presented experiments and the one-step model calculations backing the interpretation of the results we can see that this new technique could provide relevant and more direct information of compounds in which the theoretical modelling of its electronic structure is challenging or unclear. It can also be used in a complementary manner together with the conventional methods for analyzing spectra, as it can provide further ways to disentangle and identify spectral contributions.

Chapter 8

Epilogue: concluding remarks and outlook

It this thesis, we have studied several carefully selected transition metal oxides with hard x-ray photoemission spectroscopy (HAXPES). The studies showed many ways in which HAXPES can be used to learn about the electronic structure of a variety of materials. Furthermore, we have obtained results concerning different material systems with a range of physical properties. In this section, we will present our concluding remarks and outlook, starting from the general remarks about the use of HAXPES that can be drawn from all the studies performed and then individually discussing about the different material systems or studies.

Our first study on $LaCoO_3$ and other materials allowed clearing many of the doubts regarding the interpretation of HAXPES spectra. Solving what seemed to be an inconsistency and reassuring that we can explain the spectra using the same well-proven methods as the lower energy photoemission spectroscopy is a necessary first step to be able to trust in the results obtained with HAXPES and to make sure that no new or additional mechanisms are being neglected. We confirmed that the values provided by the cross-section tables together with the partial density of states are a good starting point to understand the spectra. This also allows us to determine beforehand if the conditions (i.e. the cross-section ratio's dependence of polarization, energy, etc.) are favourable or not for the experiments to be performed, and in particular, to the partial density of states of our interest. We have shown that we have to take into account, not only the contributions typically considered in the valence band but also from the semi-core $4p$ or $5p$ of some

elements such as Y, Sr, Ba or rare earths due to their large cross-sections. Moreover, one of the lessons that can be learned from the conclusions of this work is that HAXPES may be more suited to the study of the valence band of compounds containing 5*d* elements.

This is clearly seen in the study with the double perovskite iridates, where the very large Ir 5*d* cross-sections makes its contribution dominant. This allowed the direct comparison of the experimental spectra of iridates containing a wide range of other metal elements. Such direct comparison does not only make the analysis much easier, but also makes the generalization of the results in such systematic studies more convincing. Analogously in our ReO_3 study, this cross-section dominance greatly facilitated the analysis of the spectra and allowed us to concentrate on the other novel aspects that our orientation-dependent measurements provided. This clearly confirms that HAXPES is a very powerful technique to study compounds with 5*d* transition metals.

We have also showed that it is still possible to study 3*d* compounds using HAXPES: Both in the $LaCoO_3$ study and in the $CaCu_3Ru_4O_{12}$ study, where our focus was on a 3*d* transition metal, we showed that the element-specific core level spectra is still very useful and can provide a solid base for calculations. While a quantitative analysis and the observation of small details in the valence band were hampered by the small cross-sections of the 3*d* orbital of our interest, we have shown that the spectra can still provide very useful information. In the $CaCu_3Ru_4O_{12}$, measuring the valence band spectra with many different photon energies starting from hard x-rays down to VUV allowed us to so ensure that the changes were smooth and according to the change in cross-section ratios, and that no new surface-related features were appearing.

As an outlook for future projects, the study of compounds where the interest lies in elements with large cross-sections should be prioritized, including 5d transition metals compounds such as the iridates, and perhaps also rare earth or uranium compounds. The high cross-sections do not only mean an easier analysis as we have discussed about several times in this thesis, but also means a much faster measuring time, with experiments in

5*d* compounds taking even 5 to 10 times less the time than in 3*d* compounds to obtain similar signature-to-noise ratios. While in this thesis not much emphasis has been put to measuring times, it can be a very important practical aspect in synchrotron-based techniques where the availability of beamtime is limited. Longer measurements can add further experimental complications such as sample degradation (and thus, the need of new measuring spots or cleaves), stability of the beam and other experimental conditions, etc.. 4*d* compounds such as ruthenates, which also present very interesting magnetic properties, can still be measured reasonably fast, and depending on their exact composition the 4*d* may still be the largest contribution in the valence band. In the case of 3*d* compounds, experiments have to be more carefully designed to be able to extract useful information from the valence band. The different methods that we have discussed such as changing photon energy or polarization still leave room for analytical procedures to remove these large undesired contributions by using multiple experimental spectra, although the feasibility of such method may be limited to cases in which there are only a few significant contributions in the valence band.

Our understanding of these unexpected contributions in the $LaCoO_3$ spectra allows us to revisit other HAXPES spectra of compounds in which similar effects are present. This is the case in, for instance, $LaNiO_3$ or Ba_2CoO_4 which were also measured but the analysis had not been complete due to the same difficulties in interpreting the valence band spectra we had encountered in $LaCoO_3$. While the valence band may still be dominated by these undesired La or Ba *p* contributions, other measurements from the core levels or from techniques such as XAS could be used to complement the valence band study in order to be able to learn about the electronic structure of these systems.

There is also one corollary remark from the orbital imaging study that can be applied to HAXPES (or even photoemission spectroscopy in general), and that is the high importance of taking into the account the orientation of single crystal samples when measuring. As we have observed in the orbital imaging study, the specific orientation does matter on the intensity of features from

partially filled shells. However, in angle integrated photoemission studies on single crystals, very often little attention is placed on the specific orientation of the measured crystal. This could result into studies reporting different spectral shapes obtained from the same compounds, and could wrongly lead into misinterpretations and apparent inconsistencies. In particular, studies which rely on changing the incidence angle (i.e. in order to vary the surface sensitivity), may be especially affected by such orientation dependence phenomena if performed on single crystals. Therefore, it is of vital importance to explicitly report the poly- or single- crystalline nature of the sample as well as the orientation and geometry of the measurements in the case of the latter even in angle-integrated photoemission studies.

As for the experimental setup in the BL12XU HAXPES end-station, one desirable improvement would be the ability to reach lower temperatures, with a finer control to adjust the temperature, as that could allow exploring regions of interest in the phase diagrams of transition metal and rare-earth compounds. The current experimental setup makes use of a horizontally mounted open-cycle cryostat. This limits the cooling to LN2 (thus, down to 80K at most) due to the recent lack of availability of liquid helium. Moreover, its horizontal mounting (a necessary configuration to leave room to the vertical analyzer on the top of the chamber), severely limits the ability to fine-tune the flow and thus, properly control the temperature. The upgrade of the cryostat to a close-cycle system would enable the possibility of reaching to much lower temperatures while using the liquid helium in a responsible manner, although the specific details on the minimum temperature and how finely can the temperature be adjusted would highly depend on the technical specifications of the systems provided by the manufacturers.

The spectroscopy studies provided results for a variety of materials and physical phenomena. We have determined the high covalency of the double perovskite iridates, which clearly indicates that the pure ionic t_{2g}-only assumption so often found in studies of this class of compounds must be reconsidered. In this context, it would be interesting to have more theoretical

studies that go into more detail in such highly covalent scenarios. As for the long-sought Kitaev phenomenon, less covalent compounds must be sought, by for instance going to less charged d^5 compounds such as Ru^{3+} or Os^{3+}, or to fluorine compounds instead of oxides. While the scope of our study was the class of double perovskite iridates, HAXPES has proven to be a very good technique to study the covalency and could also be used to verify potential candidates of these other material classes.

In the $LaCoO_3$ study we have determined that the low spin to high spin gradual transition occurs inhomogeneously, and that structural changes occur on the high spin sites, locally reducing the hybridization strength. The presence of such changes in the high spin sites could give an additional hint to search for any possible long range low spin - high spin ordering. A good understanding on the transition and the low spin - high spin ratios is also relevant for choosing temperatures corresponding to specific fractional spin ratios in which such orderings could occur. The diffraction signals from these spin orderings may be very weak and subtle, and thus, limiting the parameter space to explore and knowing of extra hints that can reveal an ordering could prove essential to design an experiment.

In our study of $CaCu_3Ru_4O_{12}$, we have closed a long standing debate by determining that it is indeed a Kondo system with a very high Kondo temperature, reaching a compromise for the many different studies in the literature. Our results also raise new questions for which more theoretical work may be necessary, such as the relation between the correlations on the Ru site and the manifested Kondo physics or the exact nature of the more complex Kondo-like features predicted in the calculations. However, our results also open up many new opportunities to search for the Kondo phenomena in transition metal oxides. Other Cu^{2+} isostructural compounds but with a weaker screening mechanism such as the case of $CaCu_3Ir_4O_{12}$ could be an interesting starting point to search for other transition metal oxide Kondo materials but with a lower temperature scale.

Finally, in our orientation dependence study on ReO_3 and other materials, we proved that with HAXPES, it is possible to reproduce the orbital shapes from the initial state experimentally. We have seen a normalization procedure using shallow core levels of the same element allows the removal of effects from photoelectron diffraction as well as from the differences in the measuring spot. We have also observed about the presence of isotropic background contributions due to elastic scattering. Finally, we have shown increasing the photon energy can have a slight effect on the isotropic background but a change from 80 K to 300 K did not result in any significant change. This new technique complementary to the s-NIXS orbital imaging method, provides an exciting new method to determine the ground state occupation of compounds without the need to rely on calculations. Possibilities to even further enhance the capabilities of the technique could include combining it with the use of a spin detector to obtain a spin-resolved image of the occupation.

While our first attempts proved to be time consuming due to the wide energy windows and many data points, once the technique is fully understood and optimized, it may become possible to obtain the relevant information by either measuring at only a few orientations (corresponding to, for instance, the directions of the expected local maxima and minima) or at narrower energy ranges, making the technique much more time efficient. The fact that we have been able to get information from non-isolated contributions is also remarkable as in the valence band contributions are often mixed, and ensures that relevant information can be subtracted even when ideal conditions such as in the ReO_3 t_{2g} peak are not met. However, more theoretical work would be required to fully understand the nature of the isotropic contributions. So far we have observed that such contributions are also present in the one-step model calculations, and thus, its cause is already present within this theoretical model. If the specific nature of such processes is better understood, it may be possible do choose experimental conditions that minimize the presence of such background, making the process more direct and its interpretation clearer.

References

[1] M. Imada, A. Fujimori, Y. Tokura, *Rev. Mod. Phys.* **1998**, *70*, 1039–1263.

[2] N. Tsuda, K. Nasu, A. Fujimori, K. Siratori, *Electronic Conduction in Oxides*, Springer-Verlag Berlin Heidelberg, **2000**.

[3] E. Economou, *Greens Functions in Quantum Physics*, Springer, Berlin, Heidelberg, **1979**.

[4] S. Hüfner, *Photoelectron Spectroscopy*, Advanced Texts in Physics, Springer, Berlin, Heidelberg, **2003**.

[5] L. H. Tjeng, PhD thesis, Rijksuniversiteit Groningen, **1990**.

[6] E. Merzbacher, *Quantum Mechanics*, Wiley, John & Sons, Inc., **1998**.

[7] L. Ahlfors, *Complex Analysis*, McGraw-Hill Education, **1979**.

[8] S. Suga, A. Sekiyama, *Photoelectron Spectroscopy*, Springer Series in Optical Sciences, vol 176. Springer, Berlin, Heidelberg, **2014**.

[9] A. Damascelli, Z. Hussain, Z.-X. Shen, *Rev. Mod. Phys.* **2003**, *75*, 473–541.

[10] C. Laubschat, E. Weschke, C. Holtz, M. Domke, O. Strebel, G. Kaindl, *Phys. Rev. Lett.* **1990**, *65*, 1639–1642.

[11] A. Sekiyama, H. Fujiwara, S. Imada, S. Suga, H. Eisaki, S. I. Uchida, K. Takegahara, H. Harima, Y. Saitoh, I. A. Nekrasov, G. Keller, D. E. Kondakov, A. V. Kozhevnikov, T. Pruschke, K. Held, D. Vollhardt, V. I. Anisimov, *Phys. Rev. Lett.* **2004**, *93*, 156402.

[12] S. Tanuma, C. J. Powell, D. R. Penn, *Surface and Interface Analysis* **2011**, *43*, 689–713.

[13] M. P. Seah, W. A. Dench, *Surface and Interface Analysis* **1979**, *1*, 2–11.

[14] L. Tjeng, R. Hesper, A. Heessels, A. Heeres, H. Jonkman, G. Sawatzky, *Solid State Communications* **1997**, *103*, 31–35.

[15] F. Offi, S. Iacobucci, P. Vilmercati, A. Rizzo, A. Goldoni, M. Sacchi, G. Panaccione, *Phys. Rev. B* **2008**, *77*, 201101.

[16] D. Geelen, J. Jobst, E. E. Krasovskii, S. J. van der Molen, R. M. Tromp, *Phys. Rev. Lett.* **2019**, *123*, 086802.

[17] *Hard X-ray Photoelectron Spectroscopy (HAXPES)*, (Ed.: J. C. Woicik), Springer Series in Surface Sciences, Springer International Publishing, **2016**.

[18] J. Braun, J. Minár, S. Mankovsky, V. N. Strocov, N. B. Brookes, L. Plucinski, C. M. Schneider, C. S. Fadley, H. Ebert, *Phys. Rev. B* **2013**, *88*, 205409.

[19] A. X. Gray, C. Papp, S. Ueda, B. Balke, Y. Yamashita, L. Plucinski, J. Minár, J. Braun, E. R. Ylvisaker, C. M. Schneider, W. E. Pickett, H. Ebert, K. Kobayashi, C. S. Fadley, *Nature Materials* **2011**, *10*, 759–764.

[20] M. B. Trzhaskovskaya, V. I. Nefedov, V. G. Yarzhemsky, *Atomic Data and Nuclear Data Tables* **2001**, *77*, 97–159.

[21] J. J. Yeh, I. Lindau, *Atomic Data and Nuclear Data Tables* **1985**, *32*, 1–155.

[22] M. B. Trzhaskovskaya, V. I. Nefedov, V. G. Yarzhemsky, *Atomic Data and Nuclear Data Tables* **2002**, *82*, 257–311.

[23] M. B. Trzhaskovskaya, V. K. Nikulin, V. I. Nefedov, V. G. Yarzhemsky, *Atomic Data and Nuclear Data Tables* **2006**, *92*, 245–304.

[24] S. L. Molodtsov, S. V. Halilov, V. D. P. Servedio, W. Schneider, S. Danzenbächer, J. J. Hinarejos, M. Richter, C. Laubschat, *Phys. Rev. Lett.* **2000**, *85*, 4184–4187.

[25] M. Angst, T. Brückel, D. Richter, R. Zorn, *Scattering methods for condensed matter research towards novel applications at future sources*, Jülich Forschungszentrum, **2012**.

[26] S. Mobilio, F. Boscherini, C. Meneghini, *Synchrotron Radiation*, Springer-Verlag Berlin Heidelberg, **2015**.

[27] J. Weinen, T. Koethe, C. Chang, S. Agrestini, D. Kasinathan, Y. Liao, H. Fujiwara, C. Schüßler-Langeheine, F. Strigari, T. Haupricht, G. Panaccione, F. Offi, G. Monaco, S. Huotari, K.-D. Tsuei, L. Tjeng, *J. Electron. Spectrosc. Relat. Phenom.* **2015**, *198*, 6–11.

[28] D. Takegami, L. Nicolaï, T. C. Koethe, D. Kasinathan, C. Y. Kuo, Y. F. Liao, K. D. Tsuei, G. Panaccione, F. Offi, G. Monaco, N. B. Brookes, J. Minár, L. H. Tjeng, *Phys. Rev. B* **2019**, *99*, 165101.

[29] A. Amon, E. Svanidze, A. Ormeci, M. König, D. Kasinathan, D. Takegami, Y. Prots, Y.-F. Liao, K.-D. Tsuei, L. H. Tjeng, A. Leithe-Jasper, Y. Grin, *Angewandte Chemie* **2019**, *131*, 16075–16080.

[30] A. K. Efimenko, N. Hollmann, K. Hoefer, J. Weinen, D. Takegami, K. K. Wolff, S. G. Altendorf, Z. Hu, A. D. Rata, A. C. Komarek, A. A. Nugroho, Y. F. Liao, K.-D. Tsuei, H. H. Hsieh, H.-J. Lin, C. T. Chen, L. H. Tjeng, D. Kasinathan, *Physical Review B* **2017**, *96*, 195112.

[31] A. Sekiyama, J. Yamaguchi, A. Higashiya, M. Obara, H. Sugiyama, M. Y. Kimura, S. Suga, S. Imada, I. Nekrasov, M. Yabashi, K. Tamasaku, T. Ishikawa, *New Journal of Physics* **2010**, *12*, 043045.

[32] S. Ouardi, G. H. Fecher, X. Kozina, G. Stryganyuk, B. Balke, C. Felser, E. Ikenaga, T. Sugiyama, N. Kawamura, M. Suzuki, K. Kobayashi, *Phys. Rev. Lett.* **2011**, *107*, 036402.

[33] Y. Nakatsu, A. Sekiyama, S. Imada, Y. Okamoto, S. Niitaka, H. Takagi, A. Higashiya, M. Yabashi, K. Tamasaku, T. Ishikawa, S. Suga, *Phys. Rev. B* **2011**, *83*, 115120.

[34] S. Ouardi, G. H. Fecher, C. Felser, *Journal of Electron Spectroscopy and Related Phenomena* **2013**, *190*, 249–267.

[35] T. Saitoh, T. Mizokawa, A. Fujimori, M. Abbate, Y. Takeda, M. Takano, *Phys. Rev. B* **1997**, *55*, 4257–4266.

[36] R. R. Heikes, R. C. Miller, R. Mazelsky, *Physica* **1964**, *30*, 1600–1608.

[37] G. Blasse, *Journal of Applied Physics* **1965**, *36*, 879–883.

[38] G. H. Jonker, *Journal of Applied Physics* **1966**, *37*, 1424–1430.

[39] J. B. Goodenough, P. M. Raccah, *Journal of Applied Physics* **1965**, *36*, 1031–1032.

[40] P. M. Raccah, J. B. Goodenough, *Phys. Rev.* **1967**, *155*, 932–943.

[41] J. Goodenough, *Progress in Solid State Chemistry* **1971**, *5*, 145–399.

[42] M. W. Haverkort, Z. Hu, J. C. Cezar, T. Burnus, H. Hartmann, M. Reuther, C. Zobel, T. Lorenz, A. Tanaka, N. B. Brookes, H. H. Hsieh, H.-J. Lin, C. T. Chen, L. H. Tjeng, *Phys. Rev. Lett.* **2006**, *97*, 176405.

[43] J. Braun, *Reports on Progress in Physics* **1996**, *59*, 1267.

[44] J. Braun, J. Minár, H. Ebert, *Physics Reports* **2018**, *740*, 1–34.

[45] H. Ebert, D. Ködderitzsch, J. Minár, *Reports on Progress in Physics* **2011**, *9*, 096501.

[46] A. C. Thompson, D. Vaughan, et al., *X-ray data booklet*, *Vol. 8*, Lawrence Berkeley National Laboratory, University of California Berkeley, CA, **2001**.

[47] K. K. Wolff, S. Agrestini, A. Tanaka, M. Jansen, L. H. Tjeng, *Zeitschrift für anorganische und allgemeine Chemie* **2017**, *643*, 2095–2101.

[48] B. E. Prasad, T. Doert, C. Felser, M. Jansen, *Chemistry – A European Journal* **2018**, *24*, 16762–16765.

[49] K. K. Wolff, L. H. Tjeng, M. Jansen, *Solid State Communications* **2019**, *289*, 43–46.

[50] G. Khaliullin, *Phys. Rev. Lett.* **2013**, *111*, 197201.

[51] G. Cao, T. F. Qi, L. Li, J. Terzic, S. J. Yuan, L. E. DeLong, G. Murthy, R. K. Kaul, *Phys. Rev. Lett.* **2014**, *112*, 056402.

[52] J. Terzic, H. Zheng, F. Ye, H. D. Zhao, P. Schlottmann, L. E. De Long, S. J. Yuan, G. Cao, *Phys. Rev. B* **2017**, *96*, 064436.

[53] S. Bhowal, S. Baidya, I. Dasgupta, T. Saha-Dasgupta, *Phys. Rev. B* **2015**, *92*, 121113.

[54] K. Pajskr, P. Novák, V. Pokorný, J. Kolorenč, R. Arita, J. Kuneš, *Phys. Rev. B* **2016**, *93*, 035129.

[55] T. Dey, A. Maljuk, D. V. Efremov, O. Kataeva, S. Gass, C. G. F. Blum, F. Steckel, D. Gruner, T. Ritschel, A. U. B. Wolter, J. Geck, C. Hess, K. Koepernik, J. van den Brink, S. Wurmehl, B. Büchner, *Phys. Rev. B* **2016**, *93*, 014434.

[56] L. T. Corredor, G. Aslan-Cansever, M. Sturza, K. Manna, A. Maljuk, S. Gass, T. Dey, A. U. B. Wolter, O. Kataeva, A. Zimmermann, M. Geyer, C. G. F. Blum, S. Wurmehl, B. Büchner, *Phys. Rev. B* **2017**, *95*, 064418.

[57] M. Kusch, V. M. Katukuri, N. A. Bogdanov, B. Büchner, T. Dey, D. V. Efremov, J. E. Hamann-Borrero, B. H. Kim, M. Krisch, A. Maljuk, M. M. Sala, S. Wurmehl, G. Aslan-Cansever, M. Sturza, L. Hozoi, J. van den Brink, J. Geck, *Phys. Rev. B* **2018**, *97*, 064421.

[58] B. J. Kim, H. Jin, S. J. Moon, J.-Y. Kim, B.-G. Park, C. S. Leem, J. Yu, T. W. Noh, C. Kim, S.-J. Oh, J.-H. Park, V. Durairaj, G. Cao, E. Rotenberg, *Phys. Rev. Lett.* **2008**, *101*, 076402.

[59] A. Kitaev, *Annals of Physics* **2006**, *321*, 2–111.

[60] G. Jackeli, G. Khaliullin, *Phys. Rev. Lett.* **2009**, *102*, 017205.

[61] J. Chaloupka, G. Jackeli, G. Khaliullin, *Phys. Rev. Lett.* **2010**, *105*, 027204.

[62] S. M. Winter, A. A. Tsirlin, M. Daghofer, J. van den Brink, Y. Singh, P. Gegenwart, R. Valentí, *Journal of Physics: Condensed Matter* **2017**, *29*, 493002.

[63] H. Takagi, T. Takayama, G. Jackeli, G. Khaliullin, S. E. Nagler, *Nature Reviews Physics* **2019**, *1*, 264–280.

[64] S. M. Winter, Y. Li, H. O. Jeschke, R. Valentí, *Phys. Rev. B* **2016**, *93*, 214431.

[65] S. Vasala, M. Karppinen, *Progress in Solid State Chemistry* **2015**, *43*, 1–36.

[66] A. Kolchinskaya, P. Komissinskiy, M. B. Yazdi, M. Vafaee, D. Mikhailova, N. Narayanan, H. Ehrenberg, F. Wilhelm, A. Rogalev, L. Alff, *Phys. Rev. B* **2012**, *85*, 224422.

[67] G. Cao, A. Subedi, S. Calder, J.-Q. Yan, J. Yi, Z. Gai, L. Poudel, D. J. Singh, M. D. Lumsden, A. D. Christianson, B. C. Sales, D. Mandrus, *Phys. Rev. B* **2013**, *87*, 155136.

[68] M. A. Laguna-Marco, P. Kayser, J. A. Alonso, M. J. Martínez-Lope, M. van Veenendaal, Y. Choi, D. Haskel, *Phys. Rev. B* **2015**, *91*, 214433.

[69] A. M. Cook, S. Matern, C. Hickey, A. A. Aczel, A. Paramekanti, *Phys. Rev. B* **2015**, *92*, 020417.

[70] A. A. Aczel, A. M. Cook, T. J. Williams, S. Calder, A. D. Christianson, G.-X. Cao, D. Mandrus, Y.-B. Kim, A. Paramekanti, *Phys. Rev. B* **2016**, *93*, 214426.

[71] S. Fuchs, T. Dey, G. Aslan-Cansever, A. Maljuk, S. Wurmehl, B. Büchner, V. Kataev, *Phys. Rev. Lett.* **2018**, *120*, 237204.

[72] A. A. Aczel, J. P. Clancy, Q. Chen, H. D. Zhou, D. Reig-i-Plessis, G. J. MacDougall, J. P. C. Ruff, M. H. Upton, Z. Islam, T. J. Williams, S. Calder, J.-Q. Yan, *Phys. Rev. B* **2019**, *99*, 134417.

[73] S. Agrestini, K. Chen, C.-Y. Kuo, L. Zhao, H.-J. Lin, C.-T. Chen, A. Rogalev, P. Ohresser, T.-S. Chan, S.-C. Weng, G. Auffermann, A. Völzke, A. C. Komarek, K. Yamaura, M. W. Haverkort, Z. Hu, L. H. Tjeng, *Phys. Rev. B* **2019**, *100*, 014443.

[74] S. Agrestini, C.-Y. Kuo, M. Moretti Sala, Z. Hu, D. Kasinathan, K.-T. Ko, P. Glatzel, M. Rossi, J.-D. Cafun, K. O. Kvashnina, A. Matsumoto, T. Takayama, H. Takagi, L. H. Tjeng, M. W. Haverkort, *Phys. Rev. B* **2017**, *95*, 205123.

[75] J. M. Kahk, C. G. Poll, F. E. Oropeza, J. M. Ablett, D. Céolin, J.-P. Rueff, S. Agrestini, Y. Utsumi, K. D. Tsuei, Y. F. Liao, F. Borgatti, G. Panaccione, A. Regoutz, R. G. Egdell, B. J. Morgan, D. O. Scanlon, D. J. Payne, *Phys. Rev. Lett.* **2014**, *112*, 117601.

[76] A. Yamasaki, S. Tachibana, H. Fujiwara, A. Higashiya, A. Irizawa, O. Kirilmaz, F. Pfaff, P. Scheiderer, J. Gabel, M. Sing, T. Muro, M. Yabashi, K. Tamasaku, H. Sato, H. Namatame, M. Taniguchi, A. Hloskovskyy, H. Yoshida, H. Okabe, M. Isobe, J. Akimitsu, W. Drube, R. Claessen, T. Ishikawa, S. Imada, A. Sekiyama, S. Suga, *Phys. Rev. B* **2014**, *89*, 121111.

[77] F. M. F. de Groot, *Journal of Electron Spectroscopy and Related Phenomena* **1994**, *67*, 529–622.

[78] K. Koepernik, H. Eschrig, *Phys. Rev. B* **1999**, *59*, 1743–1757.

[79] J. C. Slater, G. F. Koster, *Phys. Rev.* **1954**, *94*, 1498–1524.

[80] L. Y. Lim, S. Lany, Y. J. Chang, E. Rotenberg, A. Zunger, M. F. Toney, *Phys. Rev. B* **2012**, *86*, 235113.

[81] R. Morrow, R. Mishra, O. D. Restrepo, M. R. Ball, W. Windl, S. Wurmehl, U. Stockert, B. Büchner, P. M. Woodward, *Journal of the American Chemical Society* **2013**, *135*, 18824–18830.

[82] K. Kitagawa, T. Takayama, Y. Matsumoto, A. Kato, R. Takano, Y. Kishimoto, S. Bette, R. Dinnebier, G. Jackeli, H. Takagi, *Nature* **2018**, *554*, 341–345.

[83] S. Yamaguchi, Y. Okimoto, H. Taniguchi, Y. Tokura, *Phys. Rev. B* **1996**, *53*, R2926–R2929.

[84] M. A. Korotin, S. Y. Ezhov, I. V. Solovyev, V. I. Anisimov, D. I. Khomskii, G. A. Sawatzky, *Phys. Rev. B* **1996**, *54*, 5309–5316.

[85] A. Tanaka, T. Jo, *J. Phys. Soc. Jpn.* **1994**, *63*, 2788–2807.

[86] S. Doniach, M. Sunjic, *Journal of Physics C: Solid State Physics* **1970**, *3*, 285–291.

[87] M. Abbate, J. C. Fuggle, A. Fujimori, L. H. Tjeng, C. T. Chen, R. Potze, G. A. Sawatzky, H. Eisaki, S. Uchida, *Phys. Rev. B* **1993**, *47*, 16124–16130.

[88] L. Richter, S. D. Bader, M. B. Brodsky, *Phys. Rev. B* **1980**, *22*, 3059–3064.

[89] S. R. Barman, D. D. Sarma, *Phys. Rev. B* **1994**, *49*, 13979–13982.

[90] A. G. Thomas, W. R. Flavell, P. M. Dunwoody, C. E. J. Mitchell, S. Warren, S. C. Grice, P. G. D. Marr, D. E. Jewitt, N. Khan, V. R. Dhanak, D. Teehan, E. A. Seddon, K. Asai, Y. Koboyashi, N. Yamada, *Journal of Physics: Condensed Matter* **2000**, *12*, 9259–9279.

[91] A. Chainani, M. Mathew, D. D. Sarma, *Phys. Rev. B* **1992**, *46*, 9976–9983.

[92] P. G. Radaelli, S.-W. Cheong, *Phys. Rev. B* **2002**, *66*, 094408.

[93] G. R. Stewart, *Rev. Mod. Phys.* **1984**, *56*, 755–787.

[94] P. Coleman, *arXiv:cond-mat/0612006* **2006**.

[95] C. Pfleiderer, *Rev. Mod. Phys.* **2009**, *81*, 1551–1624.

[96] S. Wirth, F. Steglich, *Nat. Rev. Mater.* **2016**, *1*, 16051.

[97] S. Kondo, D. C. Johnston, C. A. Swenson, F. Borsa, A. V. Mahajan, L. L. Miller, T. Gu, A. I. Goldman, M. B. Maple, D. A. Gajewski, E. J. Freeman, N. R. Dilley, R. P. Dickey, J. Merrin, K. Kojima, G. M. Luke, Y. J. Uemura, O. Chmaissem, J. D. Jorgensen, *Phys. Rev. Lett.* **1997**, *78*, 3729–3732.

[98] C. Urano, M. Nohara, S. Kondo, F. Sakai, H. Takagi, T. Shiraki, T. Okubo, *Phys. Rev. Lett.* **2000**, *85*, 1052–1055.

[99] A. Shimoyamada, S. Tsuda, K. Ishizaka, T. Kiss, T. Shimojima, T. Togashi, S. Watanabe, C. Q. Zhang, C. T. Chen, Y. Matsushita, H. Ueda, Y. Ueda, S. Shin, *Phys. Rev. Lett.* **2006**, *96*, 026403.

[100] K. Momma, F. Izumi, *J. Appl. Crystallogr.* **2011**, *44*, 1272–1276.

[101] W. Kobayashi, I. Terasaki, J.-i. Takeya, I. Tsukada, Y. Ando, *J. Phys. Soc. Jpn.* **2004**, *73*, 2373–2376.

[102] A. Krimmel, A. Günther, W. Kraetschmer, H. Dekinger, N. Büttgen, A. Loidl, S. G. Ebbinghaus, E.-W. Scheidt, W. Scherer, *Phys. Rev. B* **2008**, *78*, 165126.

[103] A. Krimmel, A. Günther, W. Kraetschmer, H. Dekinger, N. Büttgen, V. Eyert, A. Loidl, D. V. Sheptyakov, E.-W. Scheidt, W. Scherer, *Phys. Rev. B* **2009**, *80*, 121101.

[104] H. Xiang, X. Liu, E. Zhao, J. Meng, Z. Wu, *Phys. Rev. B* **2007**, *76*, 155103.

[105] S. Tanaka, N. Shimazui, H. Takatsu, S. Yonezawa, Y. Maeno, *J. Phys. Soc. Jpn.* **2009**, *78*, 024706.

[106] S. Tanaka, H. Takatsu, S. Yonezawa, Y. Maeno, *Phys. Rev. B* **2009**, *80*, 035113.

[107] H. Kato, T. Tsuruta, M. Matsumura, T. Nishioka, H. Sakai, Y. Tokunaga, S. Kambe, R. E. Walstedt, *J. Phys. Soc. Jpn.* **2009**, *78*, 054707.

[108] J.-G. Cheng, J.-S. Zhou, Y.-F. Yang, H. D. Zhou, K. Matsubayashi, Y. Uwatoko, A. MacDonald, J. B. Goodenough, *Phys. Rev. Lett.* **2013**, *111*, 176403.

[109] Y. Shimakawa, T. Saito, *physica status solidi (b)* **2012**, *249*, 423–434.

[110] T. Sudayama, Y. Wakisaka, K. Takubo, T. Mizokawa, W. Kobayashi, I. Terasaki, S. Tanaka, Y. Maeno, M. Arita, H. Namatame, M. Taniguchi, *Phys. Rev. B* **2009**, *80*, 075113.

[111] N. Hollmann, Z. Hu, A. Maignan, A. Günther, L.-Y. Jang, A. Tanaka, H.-J. Lin, C. T. Chen, P. Thalmeier, L. H. Tjeng, *Phys. Rev. B* **2013**, *87*, 155122.

[112] H. Liu, Y. Cao, Y. Xu, D. J. Gawryluk, E. Pomjakushina, S.-Y. Gao, P. Dudin, M. Shi, L. Yan, Y.-f. Yang, H. Ding, *Phys. Rev. B* **2020**, *102*, 035111.

[113] T. Böske, K. Maiti, O. Knauff, K. Ruck, M. S. Golden, G. Krabbes, J. Fink, T. Osafune, N. Motoyama, H. Eisaki, S. Uchida, *Phys. Rev. B* **1998**, *57*, 138–141.

[114] T. T. Tran, K. Takubo, T. Mizokawa, W. Kobayashi, I. Terasaki, *Phys. Rev. B* **2006**, *73*, 193105.

[115] J. Ghijsen, L. H. Tjeng, J. van Elp, H. Eskes, J. Westerink, G. A. Sawatzky, M. T. Czyzyk, *Phys. Rev. B* **1988**, *38*, 11322–11330.

[116] The parameters for the CuO_4 calculations have been tuned based on the values taken from ref. [122]: $U_{dd} = 7.8$, $U_{pd} = 9.0$, $\Delta = 4.0$, pd$\sigma = -1.44$, pd$\pi = 0.625$, Tpp= 1.3. Additionally, we have set the ionic crystal field paramaters to $10Dq = 1.0$, $Ds = 0.025$, $Dt = 0.05$. All values are in eV.

[117] M. Taguchi, A. Chainani, K. Horiba, Y. Takata, M. Yabashi, K. Tamasaku, Y. Nishino, D. Miwa, T. Ishikawa, T. Takeuchi, K. Yamamoto, M. Matsunami, S. Shin, T. Yokoya, E. Ikenaga, K. Kobayashi, T. Mochiku, K. Hirata, J. Hori, K. Ishii, F. Nakamura, T. Suzuki, *Phys. Rev. Lett.* **2005**, *95*, 177002.

[118] G. Panaccione, F. Offi, P. Torelli, G. Vanko, O. Tjernberg, P. Lacovig, A. Guarino, A. Fondacaro, A. Nigro, M. Sacchi, N. B. Brookes, G. Monaco, *Phys. Rev. B* **2008**, *77*, 125133.

[119] L. H. Tjeng, C. T. Chen, J. Ghijsen, P. Rudolf, F. Sette, *Phys. Rev. Lett.* **1991**, *67*, 501–504.

[120] L. H. Tjeng, C. T. Chen, S.-W. Cheong, *Phys. Rev. B* **1992**, *45*, 8205–8208.

[121] H. Eskes, G. A. Sawatzky, *Phys. Rev. Lett.* **1988**, *61*, 1415–1418.

[122] H. Eskes, L. H. Tjeng, G. A. Sawatzky, *Phys. Rev. B* **1990**, *41*, 288–299.

[123] J. Kuneš, *Phys. Rev. B* **2011**, *83*, 085102.

[124] H. Yavaş, M. Sundermann, K. Chen, A. Amorese, A. Severing, H. Gretarsson, M. W. Haverkort, L. H. Tjeng, *Nature Physics* **2019**, *15*, 559–562.

[125] B. Leedahl, M. Sundermann, A. Amorese, A. Severing, H. Gretarsson, L. Zhang, A. C. Komarek, A. Maignan, M. W. Haverkort, L. H. Tjeng, *Nature communications* **2019**, *10*, 5447–5447.

[126] A. Amorese, B. Leedahl, M. Sundermann, H. Gretarsson, Z. Hu, H.-J. Lin, C. T. Chen, M. Schmidt, H. Borrmann, Y. Grin, A. Severing, M. W. Haverkort, L. H. Tjeng, *Phys. Rev. X* **2021**, *11*, 011002.

[127] S. Goldberg, C. Fadley, S. Kono, *Solid State Communications* **1978**, *28*, 459–463.

[128] S. Goldberg, C. Fadley, S. Kono, *Journal of Electron Spectroscopy and Related Phenomena* **1981**, *21*, 285–363.

[129] P. Puschnig, S. Berkebile, A. J. Fleming, G. Koller, K. Emtsev, T. Seyller, J. D. Riley, C. Ambrosch-Draxl, F. P. Netzer, M. G. Ramsey, *Science* **2009**, *326*, 702–706.

[130] C. Fadley, M. Van Hove, Z. Hussain, A. Kaduwela, *Journal of Electron Spectroscopy and Related Phenomena* **1995**, *75*, Future Perspectives for Electron Spectroscopy with Synchrotron Radiation, 273–297.

[131] G. Schönhense, K. Medjanik, S. Babenkov, D. Vasilyev, M. Ellguth, O. Fedchenko, S. Chernov, B. Schönhense, H.-J. Elmers, *Communications Physics* **2020**, *3*, 45.

[132] J. Falke, C. F. Chang, C. E. Liu, D. Takegami, A. Melendez-Sans, C.-S. Chen, L. Zhao, A. C. Komarek, C.-Y. Kuo, C. T. Chen, L. H. Tjeng, *Phys. Rev. B* **2021**, *103*, 115125.

[133] M. A. V. Alvarez, H. Ascolani, G. Zampieri, *Phys. Rev. B* **1996**, *54*, 14703–14712.

[134] S. Babenkov, K. Medjanik, D. Vasilyev, S. Chernov, C. Schlueter, A. Gloskovskii, Y. Matveyev, W. Drube, B. Schönhense, K. Rossnagel, H.-J. Elmers, G. Schönhense, *Communications Physics* **2019**, *2*, 107.

[135] C. F. Chang, T. C. Koethe, Z. Hu, J. Weinen, S. Agrestini, L. Zhao, J. Gegner, H. Ott, G. Panaccione, H. Wu, M. W. Haverkort, H. Roth, A. C. Komarek, F. Offi, G. Monaco, Y.-F. Liao, K.-D. Tsuei, H.-J. Lin, C. T. Chen, A. Tanaka, L. H. Tjeng, *Phys. Rev. X* **2018**, *8*, 021004.

Acknowledgements

First of all, I would like to thank my supervisor, Hao Tjeng, for all the guidance and support. I am very grateful that I had the chance to do work in your group, to learn directly from you about physics, correlations, experimental techniques, etc. and also I greatly appreciate that I have had the chance to have additional experiences such as helping with the lectures and managing the beamtimes in SPring-8 which have given me a lot of experience in many aspects beyond performing experiments and calculations.

I would also like to thank Stefano Agrestini for all the daily support during the first years of my PhD, teaching me many things from sample preparation to calculations, an office mate who was always there whenever I needed some assistance.

I am also very grateful to many of the colleagues of the department, in particular Deepa Kasinathan, Chun-Fu Chang (Roger), Simone Altendorf, Sahana Roßler, Vanda Pereira and Chi-Nan Wu not only for the helping me with different experiments or calculations but also for the continued support during all these years in Dresden, and of course, the coffee breaks, hikes and other activities that made the stay much more enjoyable.

I would also like to thank Alexander Komarek as well as many of the other colleagues from his group, Hanjie Guo, Gihun Ryu, Li Zhao, Lunyong Zhang, Zhiwei Li, Junwon Seo, Donghoon Lee and Anna Meléndez for providing always high quality samples that make our spectroscopy experiments possible.

Special thanks to Katharina Höfer and Christoph Becker for all the swift assistance for repairs and maintenance of the experimental equipment, as well as for all the new designs for experimental setups and sample holders that allowed performing experiments that otherwise would not have been possible.

I am also grateful to Philipp Hansmann for teaching me more about calculations and helping me understand their interpretation and to Zhiwei Hu for his advice and expertise in many different aspects.

As for the collaborators from external institutions, I would like to begin by expressing my gratitude to Yen-Fa Liao, Ku-Ding Tsuei, and more recently also Yoshimura Masato for the continued technical assistance and guidance during the HAXPES experiments in the Taiwan beamline in SPring-8, as well as to Hiraoka Nozomu for coordinating the logistics and beamtimes, always listening to our scheduling requests.

I would like to thank Tanaka Arata from Hiroshima University, not only for making a very great program that I extensively used during these years, but also for hosting me in Hiroshima and helping us understand many of the results of the calculations.

I would also like to thank Ján Minár and Laurent Nicolaï from the University of West Bohemia for the one-step calculations and all the theoretical discussions about cross-sections and all the processes that are going on during the photoemission process, making it possible to understand a significant part of the work presented in this thesis.

I would like to express my gratitude to Hariki Atsushi from the Osaka Prefecture University and Jan Kuneš from the Technische Universität Wien for providing us with very finely tuned DMFT calculations and for all the discussions about the Kondo physics in CCRO.

Also, I would like to mention and thank Mizokawa Takashi from Waseda University for the brief but interesting discussions about this same compound as well as other experimental aspects.

I am grateful to Kyung-Tae Ko and Jeong-Gyu Kim for providing us beamtime in Pohang and the assistance during the experiments in Korea.

I would also like to thank Ryan Morrow and Sabine Wurmehl from IFW Dresden for providing us with many iridate and ruthenate single crystals, as well as to Sugano Satoshi and Shimakawa Yuichi from Kyoto University, Axel Günther from University of Augsburg, and Stefan Ebbinghaus from Martin-

Luther-Universität Halle-Wittenberg for providing us with the CCRO samples.

Back to the colleagues from our institute, I would like to acknowledge and thank all the people with whom I had the chance to share the many long beamtimes: Cheng-En Liu (Phoebe), Chang-Yang Kuo, Roger, Johannes Falke, and Anna Meléndez for the beamtimes NSRRC, in Taiwan. Special thanks to Phoebe for bringing always very interesting Taiwanese food during the beamtimes and guiding me through Hsinchu.

I would like to thank Andrea Amorese, Martin Sundermann, Andrea Marino, as well as Andrea Severing for the beamtimes in DESY, where I was able to learn a lot about Uranium compounds and other systems that I would not have touched otherwise in the scope of my thesis.

I am also grateful to Stefano Agrestini and Andrea Severing for making my first two beamtime experiences in ESRF very interesting and having had the chance to learn about many diverse techniques and compounds during my first months after starting my PhD. Also, once again, I am grateful to Stefano Agrestini also for inviting me to the all-nighter XMCD beamtime in ALBA.

Next, I would like to thank the people with whom I shared the many SPring-8 beamtimes, starting with Klaus Wolff and Simone Altendorf who showed how the experimental setup worked during my first beamtimes in Japan, and also to all people who assisted me in my many experiments afterwards and made the long beamtime hours much more interesting and enjoyable: Deepa Kasinathan, Katharina Höfer, Federico Meneghin, Alfred Amon, Chang-Yang Kuo, Anna Meléndez, Vanda Pereira, Johannes Falke, Ana Barrios, Cariad Knight, Daria Balatsky, Shao-Lun Huang, Connor Dalton.

I would also like to mention and thank to all cat-sitters that took care of the cats during the beamtimes and many other trips and allowed me to travel and do all the experiments without having to worry about them: Vanda Pereira, Johannes Falke, Andrea Amorese, Po-Ya Yang, Belén Zúñiga, and Deepa Kasinathan

Finally, I want to thank the non scientific staff of our institute, and in particular Ellen Winkler for helping me with all the necessary arrangements for any beamtime or business trip, allowing me to focus on my scientific work.

I also want to express my gratitude to Jochen Geck from the Technische Universität Dresden for his guidance and advice in the TAC meetings.

Special thanks to Eric Pellegrin who encouraged me to pursue this path and put me in contact with Hao Tjeng and his group in Dresden.

This work has been carried out with support of the Deutsche Forschungsgemeinschaft (DFG) through Grant No. 320571839 and SFB 1143 (project-id 247310070). The experiments in Taiwan and Korea were facilitated by the Max Planck-POSTECH-Hsinchu Center for Complex Phase Materials.

Finalment, m'agradaria fer una menció especial a J.P.C., F.P.P. i A.M.S. i agrair-los el continuat suport durant tots aquests anys, que m'ha permès superar els moments difícils i finalitzar exitosament la tesi.